SZÉCHENYI ISTVÁN EGYETEM
MULTIDISZCIPLINÁRIS MŰSZAKI TUDOMÁNYI DOKTORI ISKOLA

Sipos Dávid

SIMULATION OF FULL VEHICLE ACOUSTICS IN MID-FREQUENCY RANGE

Doktori értekezés

Témavezető:
Dr. Feszty Dániel
Tanszékvezető
Járműfejlesztési Tanszék, Széchenyi István Egyetem

2023

TABLE OF CONTENTS

DECLARATION OF ORIGINALITY

I hereby declare that the intellectual content of this thesis is the product of my own work and that all the assistance received in preparing this thesis and sources have been acknowledged. Parts excepted are corrections of form and content by my supervisor.

ACKNOWLEDGEMENT

I would like to express my deepest appreciation to the following people for their support and contribution over the years. I'm extremely grateful to Dr. Daniel Feszty, my supervisor, for all the guidance and support he provided to me throughout my doctoral studies. Thanks should also go to Antoine Guellec for mentoring he gave to our research group.

Completing this research would not have been possible without the funding of the Hungarian Academy of Sciences and Audi Hungaria Zrt through the MTA-SZE Lendület Vehicle Acoustics Research Group.

I am also grateful to Jonathan Jacqmot for giving me an opportunity to work at Free Field Technologies. Special thanks to Tamás Turcsik for his time, effort, and expert advice throughout the years. In addition, I had the pleasure of working with Markus Brandstetter, his assistance and expert advice is deeply appreciated.

Furthermore, I would like to extend my sincere thanks to the colleagues at the Department of Whole Vehicle Engineering, Audi Hungaria Zrt., Audi AG and Free Field Technologies. Finally, I would like to express my gratitude to my family, my friends and girlfriend for all the support, motivation, and encouragement that helped me through the difficulties.

KIVONAT

A személyautók NVH tulajdonságai kiemelt jelentőséggel bírnak a potenciális vásárlók megítélése szempontjából. Emiatt az autóipari szereplők egyre nagyobb hangsúlyt fektetnek az ezen területen történő fejlesztésekre. A számítógépes szimulációs módszerek, mint a Végeselem Módszer (VEM) és a Statisztikai Energiaanalízis (SEA) nagyban hozzájárulnak a fejlesztési folyamat hatékonyságához, de a középfrekvencia-tartományban (400 – 1 000 Hz) ezen módszerek csak korlátozottan használhatók. Jelen kutatási munka célja a Virtual SEA szimulációs módszer fejlesztése és alkalmazása járművek középfrekvenciás akusztikai szimulációjára.

A módszer alkalmazhatóságának vizsgálata többszintű validációs kampány keretein belül történt, melynek első lépésében hajlított, vonal- és ponthegesztett, valamint ragasztott lemezszerkezetek álltak. A végeselemes modellezés révén a Virtual SEA módszerrel számolt kapcsolati veszteségi tényezők és a kísérleti úton kapott, adott kötéstechnológiára jellemző értékek korrelációja figyelhető meg. További Kísérlettervezés (DOE) tanulmány kimutatta, hogy ponthegesztés esetében a lemezvastagságok aránya jelentős mertékben, a kapcsolódási „pontok” merevsége és átmérője pedig kisebb mértékben befolyásolja a kapcsolati veszteségeket.

Az SEA alrendszerfelosztásnak meghatározó szerepe van a modell érvényességére és pontosságára nézve. Ennek vizsgálata egy egyszerűsített autómodellen történt, amely intuíció alapú, K-Means, X-Means klaszteralgoritmussal, valamint megoldó által automatikusan generált alrendszerfelosztások SEA feltételek szerinti összehasonlítását foglalja magába. Az eredmények tanúsága szerint az automatikus partícionálás biztosítja a legjobb minőségű modellt, ami egyben a legjobb korrelációt is eredményezi a referencia VEM szimulációval.

A validációs kampány legkomplexebb eleme egy teljes járműmodellt tartalmaz, melyben az utastér elemei, valamint a belső légüreg is megtalálható. Előzetes szimulációk kimutatták, hogy a járműkarosszéria szerkezeti csillapítása a frekvencia függvényében változik. A teljesjármű szimulációs modellben az utastér elemi közül a szőnyeg, a tűzfal csillapítás, a tetőkárpit és a hátsó ülések szerepeltek, melyek porózus anyagokat is tartalmaztak. A dinamikai és akusztikai eredmények méréssel történő összevetése alapján a Virtual SEA módszer képes járművek középfrekvenciás akusztikai viselkedését megfelelő pontossággal előre jelezni.

A járművekben keletkező szerkezeti zajok hatékonyan csökkenthetők csillapító fóliák alkalmazásával. Ez a munka egy olyan újszerű módszertant mutat be, amely segítségével a csillapító fóliák optimális helyzete meghatározható azon energetikai mennyiségek alapján,

amelyek egy Virtual SEA számítás során rendelkezésre állnak. A módszertan hatékonyságát mutatja, hogy segítségével egy valós járműkarosszérián 33%-kal kevesebb csillapító fólia alkalmazásával változatlan NVH tulajdonságok érhetők el.

ABSTRACT

The Noise, Vibration and Harshness (NVH) characteristics of passenger cars are of particular importance for potential buyers. Hence, car manufacturers have been investing huge efforts in product development in this field. Simulation methods such as Finite Element Method (FEM) and Statistical Energy Analysis (SEA) have been proven to make the development process quicker and more cost-effective, but they both face various challenges in predicting the mid-frequency (400 – 1 000 Hz) acoustics of full vehicle models. Thus, the goal of this research is to assess and enable the recently proposed Virtual SEA method to provide a solution to the mid-frequency acoustic simulation of full vehicles.

A multi-level validation campaign was carried out to investigate the applicability of the Virtual SEA method for vehicle structures, starting with flat plates coupled with the most common joining methods, such as bending, line welding, gluing and spotwelding. Results showed that Virtual SEA allows to consider the effect of various junction types via Finite Element (FE) modeling and the so-obtained Coupling Loss Factors (CLF) correlate with experimental results. A Design of Experiment (DOE) study highlighted that the thickness ratio of the connecting plates has major, and the connection area and stiffness have minor influence on the coupling strength of the spotwelded junction.

A simplified car model was used to investigate the effect of sub-structuring on the SEA model validity and accuracy. Intuition-based sub-structuring was compared to K-Means, X-Means clustering algorithms and to the automatic partitioning of MSC Actran, in terms of the fulfilment of the weak coupling assumption and the reciprocity relation. The results showed that the automatic partitioning provides the best quality model, which also leads to the best correlation with the reference FE simulation.

The most complex level of the Virtual SEA validation campaign features a full-scale passenger car model with poro-elastic trim parts and an internal cavity. First, it was shown that the constant structural damping cannot hold in the entire frequency range, thus frequency-dependent damping must be used for the car structure. In the trimmed body configuration, the carpet, the firewall insulation, the headliner, and the rear seats were considered as multilayered trim parts that contain poro-elastic materials. Comparison of dynamic and acoustic results with measurements showed that the Virtual SEA method is able to predict the NVH characteristics of vehicles in the mid-frequency range.

In passenger cars, structure-borne noise can be effectively reduced by placing damping layers on large panels. This work presents a novel methodology for finding the optimal distribution of

damping layers based on the energetic quantities that are calculated during a Virtual SEA simulation. The effectiveness of the method is presented on a full-scale car model, on which 33% of the damping layers could be removed while keeping the NVH performance on the same level.

NOMENCLATURE

$\mathbf{A}$	Acoustic fluid boundary matrix	v_n, v_t	Normal and tangent velocities
$\mathbf{B}$	Damping matrix	$\mathcal{W}$	Modal work
c_f	Speed of sound	$\widetilde{W}_i$	Injected power
E	Young's modulus	$\widetilde{W}_d$	Dissipated power
E_i	Subsystem energy	y_i	Experiment output
$\boldsymbol{E}$	Energy matrix	$\mathbf{Z}$	Dynamic stiffness matrix
f_i	Trim layer thickness scaling factor	Z	Trim impedance
$\boldsymbol{f}(\omega)$	Time integrated load	α_j	Adjustable parameter
$\mathbf{H}$	Frequency Response Function	α_∞	Tortuosity
h	Scaled trim layer thickness	$\alpha(x)$	Subsystem energy scaling factor
i	Imaginary unit	$\alpha(\Theta)$	Absorption coefficient
$\mathbf{K}$	Stiffness matrix	Δ	Modal damping bandwidth
k	Wave number	ζ	Normal acoustic impedance
$\mathbf{M}$	Mass matrix	$\boldsymbol{\eta}$	Loss matrix
M	Modal mass	η_i	Damping Loss Factor
n	Number of experiments	η_{ij}	Coupling Loss Factor
n_i	Modal density	η_s	Structural damping coefficient
$\boldsymbol{P}$	Injected power matrix	Λ	Viscous characteristic length
P	Load vector	Λ'	Thermal characteristic length
P_{in}^i	Injected power	ν	Poisson ratio
p	Pressure	ξ	Modal coordinate
S	Coupling surface	ρ_s	Solid phase density
T	Total thickness of trim	σ	Resistivity
$\tilde{T}_k$	Kinetic energy	σ_p	Stress mode shape
t_i	Trim layer thickness	σ_n, σ_t	Normal and tangent stresses
$u(t)$	Displacement	$\mathbf{\Phi}$	Modal matrix
x_k^i	Independent variable	Φ	Eigenvector
$X_m(x)$	Arbitrary fixed function	ϕ	Porosity
$\tilde{V}_k$	Potential energy	ω	Angular frequency

.

1. INTRODUCTION

The subjective comfort of vehicle passengers can be traced back to a series of factors, among which disturbing noises, vibrations and harsh, intrusive effects play a prominent role. The aforementioned effects are the same physical phenomena, they differ from each other only in the frequency range and in the way of human perception. The Noise, Vibration and Harshness (NVH) comfort features are not only one of the most important evaluation criteria of potential buyers but are closely related to travel safety as well since they can cause a feeling of discomfort and reduce the ability to concentrate. Buyers today prefer efficient, comfortable vehicles. Thus, car manufacturers have been investing huge efforts in product development to meet the often-conflicting conditions of customer demands. As an example, the interior noise can be reduced by adding noise insulators and damping materials, but the increased weight will affect the dynamics and the emissions or the energy consumption of the vehicle. As a result of these, the role of Virtual Prototyping (VP) and Computer Aided Engineering (CAE) methods is continuously increasing in the development process, enabling to achieve the desired vehicle characteristics and to evaluate various design options as quickly and cost-effectively as possible.

1.1. Characteristics of vehicle structures and noise sources

Thanks to advanced development methods, a modern vehicle features an integrated body and frame (unibody chassis) that provides lightweight design with adequate rigidity/stiffness. In such a structure, the entire car is a load-carrying unit, thus its specifics determine the dynamics, performance, comfort, safety, and many other characteristics of the vehicle. A wide range of materials is used, (see Figure 1) to maximize these characteristics while keeping the overall weight as low as possible. Due to the material diversity, several types of joining methods are used, as shown in Figure 2. These joining methods are extremely challenging to model in virtual prototypes, but they are decisive factors regarding the behavior of the complete model. In order to reduce the complexity of full-scale vehicle models, different model stages are distinguished. The least complex stage is called Body-in-White (BIW) that consists only of the chassis and the front and rear windshields. A Body-in-Blue (BIB) structure includes the front and rear doors, thus forming an enclosed internal cavity. The most complex stage is the Trimmed Body (TB) that includes all of the lining and trim elements in the passenger compartment, usually containing poro-elastic materials (PEM) such as foams, felts, etc. These materials contribute to noise reduction inside the cabin.

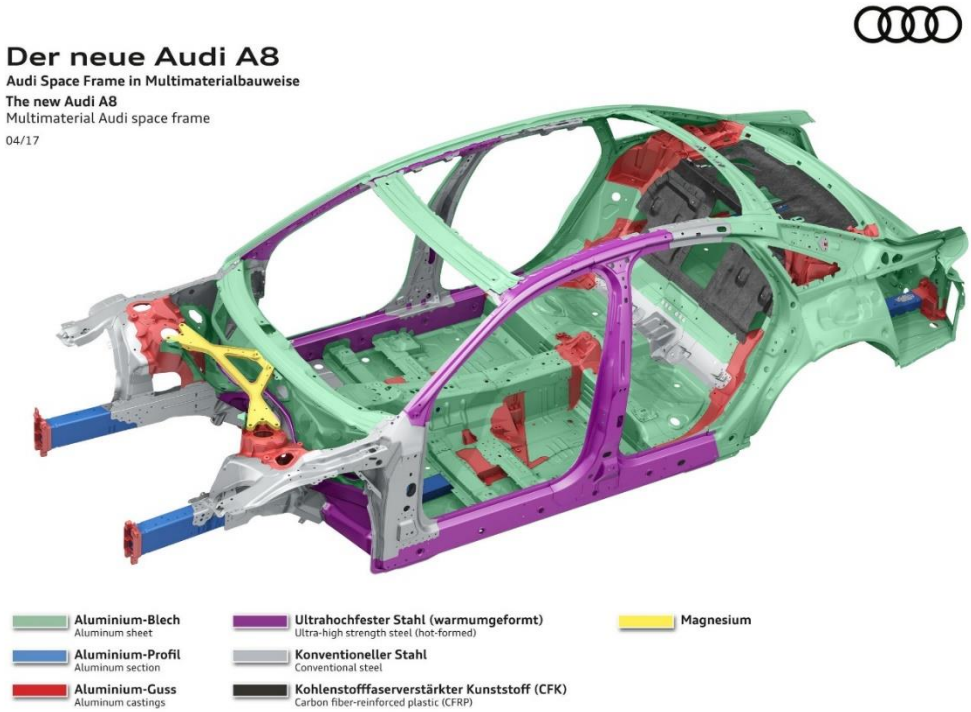

Figure 1. Multi-material vehicle chassis [1].

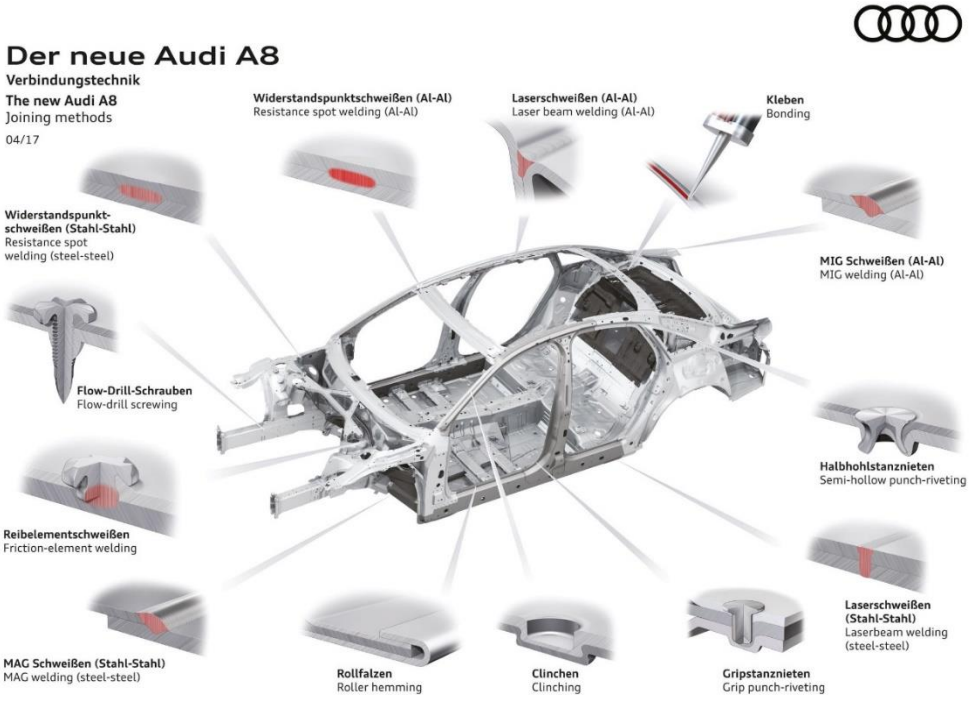

Figure 2. Joining methods in multi-material vehicle chassis [2].

There are two main sources from which noise could originate in a vehicle. Structure-borne noise is induced by the time-varying loads entering the chassis from the suspension and engine/motor mounts. The structure transfers these vibratory loads to the large, noise-radiating panels that in

turn either excite the air in the cabin and generate noise or are perceived as vibrations by the passengers. Structure-borne noise generally falls within the low- and mid-frequency range (0-400 Hz and 400 – 1 000 Hz, respectively). Airborne noise, on the other hand, is typically induced by the pressure fluctuations in the surrounding air of the structure and is dominant in the high frequency range (above 1 000 Hz). These two distinct phenomena require different simulation tools for their prediction.

1.2. Methods and motivation

Several well-established CAE methods are available to assess the NVH characteristics of a vehicle in the early development phase depending on the frequency range to consider. Multibody Simulations (MBS) are typically used in the inaudible frequency range (below 20 Hz) for conducting motion analysis, to evaluate the comfort, safety, and dynamics of the vehicle. It is widely used for suspension design as well, which is a decisive factor in terms of rolling noise. Finite Element Analysis (FEA) is one of the most popular tools to solve complex engineering problems in various fields, including structural dynamics and acoustics. It uses Finite Element Method (FEM) to create a discretized mathematical model (mesh) of the model, in which connection points (nodes) the approximated solution of the displacement field is given by a set of algebraic equations. In dynamic analyses, at least 6-8 nodes per wavelength of the propagating waves are required to capture the vibrations of the model. In other words, the frequency range dictates the mesh density. Consequently, higher frequency simulations require finer mesh, which increases the computational requirements of the solution. However, there are other difficulties too in high frequency simulations that are challenging to solve by deterministic methods. These are the statistical nature of the frequency response, associated with the model uncertainty. With the increase of the frequency, the sensitivity to the model details, as well as the modal density of the structure increases. Thus, system level responses provided by energetic indicators would give more meaningful results. Statistical Energy Analysis (SEA) is the most widely used energetic approach in the high frequency range. In such analysis, the structure is subdivided into rather large panels and the spatially and frequency-averaged power balance of these is investigated. As Figure 3 shows, three distinct regions can be identified in the typical dynamic response of a model.

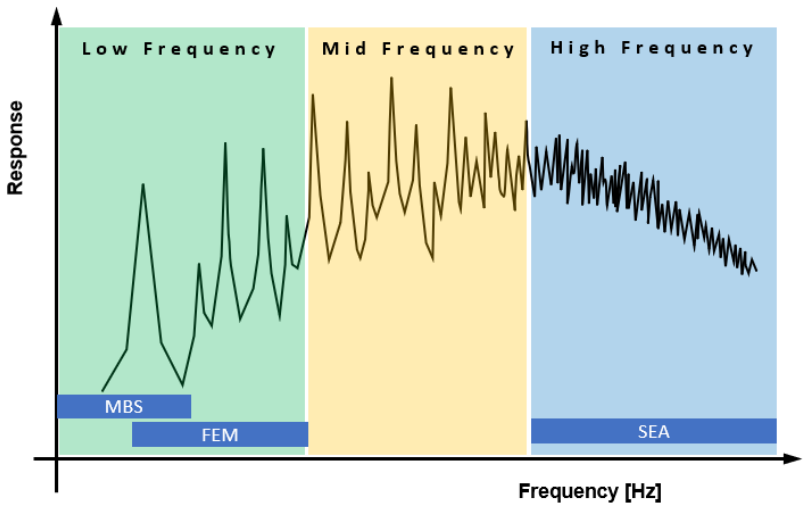

Figure 3. Typical dynamic response of a model and applicable methods.

Simulation methods, such as MBS and FEM cover the low frequency range where the response is deterministic and is driven by the global behavior of the model, typically below 400 Hz in the automotive industry. SEA is suitable at the other, high-frequency end of the spectrum (typically above 1 000 Hz), where the local behavior is dominant. However, in the transition zone, often called the "mid-frequency gap", both methods reach their limitations, and their applicability is compromised. With the spread of electric vehicles, the need to develop a simulation tool able to provide comprehensive, broadband solution in the full frequency range is growing. This is because instead of an internal combustion engine, more disturbing noise sources (electric motor, inverter, etc.), emitting higher frequency excitations are installed in the vehicle. Therefore, the present work aims to explore the limitations of state-of-the-art full vehicle acoustic simulation methods, as well as to enable the recently proposed Virtual SEA method to solve the "mid-frequency gap" problem. Various aspects of its capabilities, applicability and validity have been investigated and developed in this Dissertation.

This Dissertation is structured in the following way. First, a comprehensive literature review is provided in the field of full vehicle acoustic simulations with FEM and SEA, extraction of the SEA parameters, SEA sub-structuring and interior noise reduction. Based on this, the research gaps are identified, and the precise objectives of the Dissertation are formulated. After reviewing the theoretical background of the relevant numerical methods in detail, the solutions to the individual goals are discussed.

2. LITERATURE REVIEW

2.1. Full vehicle acoustic simulations

2.1.1. Finite Element Method in vehicle acoustics

Finite Element Method is a well-established CAE tool to solve complex computational problems in most of the fields of virtual development. It has been used to evaluate the NVH characteristics of vehicles since the early 1980s. Since then, the ever-increasing computational capacities allowed more detailed models to be created. In this Section, the main stages of the development of full vehicle acoustic FEM simulations are reviewed through the most important studies in literature.

Sung and Nefske [3], [4] presented the first 3D forced coupled analysis of a vehicle structure with an interior cavity and described the details of the coupled modal solution procedure. The analysis was limited to frequencies below 100 Hz due to the decreasing accuracy of the structural model. In this range, the predicted and the measured interior sound pressure showed generally good agreement. Sung et al. [5] later presented the development of a coupled finite element trimmed body model and its experimental evaluation up to 200 Hz. In their half-vehicle model, the trim parts were modeled as non-structural mass (NSM) elements. This means that only the mass effect of the trim parts is considered. The level and the trend of the spatially averaged vibrations and front seat sound pressure were predicted with acceptable accuracy. To resolve the deficiencies of the model, improvements were proposed regarding the structural modeling and the damping determination. Sol and Van Herpe [6] demonstrated the step-by-step process of building a structural FE model from validated component models. Trim effects were considered by updating the numerical properties of the model, such as damping, mass, and so on, based on comparisons against measurements. To assess the constructed model, sound pressure and displacement response functions were shown, and fairly good agreement was achieved below 150 Hz in terms of the functions' level and shape. Yuksel et al. [7] used the FEM-BEM approach to predict the sound pressure level inside a commercial vehicle interior and determined the contribution of the radiating panels. A Design of Experiment (DOE) was performed along with a Response Surface Modeling (RSM) for three performance metrics to optimize panel thicknesses. The efficiency of the method was proven by achieving improved vibro-acoustic responses in their model. The same method was used in Ref. [VIII] to investigate the effects of the poro-elastic material properties on the dynamic and acoustic response of a

simplified car model. This allows to find the most significant parameters, the fine-tuning of which may yield optimized NVH characteristics.

As the available computational capacities have grown, more advanced modeling techniques evolved regarding the fluid-structure coupling [8] [9], the model details and the consideration of the trim parts. Theoretical developments contributed to provide efficient FEM formulations for trim modeling based on Biot's theory of wave propagation in porous media [10], [11], [12], [13], [14]. Blanchet et al. [15] summarized the theoretical foundations of FE trim modeling and provided references to a wide range of industrial studies, which highlight its advantages over previous methods. One of the most recent analyses of a fully trimmed vehicle was made by Caillet et al. [16], representing the state-of-the-art of FEM-PEM modeling in the automotive industry. Almost all acoustic trim parts were considered in the model as finite elements equipped with poro-elastic material properties. The model building and the validation process was described in detail, including mesh creation, the procedure of obtaining material parameters, coupling conditions and model investigations. Even if the process needs much more computational resources than NSM models, it provides great accuracy according to the SPL results up to 400 Hz. The same conclusion was made by Yoo et al. [17] in 2019. The exponential increase in computational costs and the uncertainty of the model makes higher frequency FEM-PEM simulations highly impractical.

2.1.2. Statistical Energy Analysis in vehicle acoustics

Statistical Energy Analysis was first introduced by Lyon and Maidanik [18] and Smith [19] in the 1960s. SEA is more suitable for high-frequency analyses since it uses spatial and frequency averaging. The unknown in the equations is the vibrational energy level of subsystems, of which propagation is driven by the Damping Loss Factors (DLF) and Coupling Loss Factors (CLFs). Several examples of SEA applications for vehicle structures can be found in the literature.

Steel [20] studied the structural vibration transmission of a car body. In this early work, the vehicle body is modeled by a set of flat plates and only the flexural waves are considered. Sound transmission through the door hinges and through the rubber strips around the windows is also investigated. The results were compared to measurements and an acceptable correlation was found above 500 Hz. Galasso et al. [21] have built up the SEA model of a passenger car with multiple levels of detail. They found that for such complex model, unfortunately it is inevitable to have subsystems that do not satisfy the SEA assumptions, such as they are not weakly coupled, do not have sufficient modal density and homogenous energy distribution, and they do not fulfil the reciprocity relation. It was also highlighted that obtaining the coupling loss

factors through experiments is extremely expensive in terms of the effort needed. With the proposed point junction modeling of connections, their results showed good agreement with measurements. Musser et al. [22] addressed the modeling assumptions used to generate the interior of vehicle and the surrounding structure. The internal cavity of the vehicle was divided into several acoustic spaces, contrary to the SEA assumptions. This enabled the comparison of different measured and predicted transfer functions. The careful calibration of the model led to accurate predictions. Xin et al. [23] presented the validation of an SEA car body model. Measured accelerations of different powertrain points and aerodynamics pressures obtained through CFD simulations were used as excitations at different operating conditions. They claimed a maximum of 3 dB difference deviation between the predicted and the measured sound pressure level at the driver's ear in the frequency range from 200 Hz to 5 kHz. However, no information was provided on the SEA model building methodology. Bötke et al. [24] used SEA to investigate the acoustic package of an electric vehicle that was subjected to random noise sources such as road noise and wind noise. The analysis of these sources exceeds the limitations of the finite element method. The materials in the simulation model were characterized by properties typical of porous materials. They conducted measurements in semi-anechoic chamber and in a closed test track as well at constant speeds to validate their model. However, it is not clear exactly how the model was built up. The authors state that the process is largely user-dependent, and they refer to external help in minimizing user errors. Jang et al. [25] presented the SEA modeling and simulation of a mid-size truck in commercial SEA software, VA One. The subsystems were created bearing in mind the SEA assumptions. Most of the panels were slightly curved plates with stiffeners that were tuned according to the component level FE model. The internal cavity was divided into multiple subsystems. Noise control treatment was applied on the panels, the effect of which was considered by the Transfer Matrix Method. Measurements were performed at multiple conditions, which validated the SEA model. Regarding the model parameters, the authors only relied on the analytical values provided by the software.

2.1.3. Hybrid FE-SEA in vehicle acoustics

The mid-frequency gap between the applicability of FEM and SEA has been known for a long time. In the hybrid Finite Element (FE) - SEA method [26] [27], the system was represented by deterministic FE components as a master system that couples SEA subsystems with statistical properties. The results were given in the form of the ensemble average of the system [28] [29].

A number of works that used the hybrid approach for full vehicle acoustic simulations can be found in the literature.

Charpentier et al. [30] [31] presented the hybrid FE-SEA approach on a full vehicle model and predicted the interior noise levels due to broadband structure-borne excitation from 200 Hz to 1 000 Hz. In the former study, they found that standard algorithms can accurately model simple structural junctions. Their goal was to investigate and improve the coupling of FE and SEA components by detailed local FE models and a simple methodology was proposed to guide the FE/SEA partitioning. It was shown that significant computational costs could be saved with the hybrid approach. The predicted noise levels were within the 3-5 dB range compared to experiments. The same hybrid model was used for a contribution analysis and a sound package optimization in later studies [32] [33]. Chen et al. [34] built up a simplified FE-SEA model to predict the interior noise in vehicle at the development and design stage. The division of the FE/SEA parts is discussed in detail. The parameters of the hybrid model, such as modal densities, damping and coupling loss factors were obtained using mostly analytical methods. The sound absorption and the insulation of trim bodies were also considered. Excitations included road noise, wind noise, engine mount and engine sound radiation. The overall relative error between prediction and experiment was less than 1%. Musser and Rodrigues [35] presented the improvements of mid-frequency model correlation by using a hybrid FE-SEA approach. It was shown that the accurate characterization of structural input power yielded the largest improvement and that the measured, or FE simulated conductance data could be used to fine-tune an SEA model.

2.2. SEA parameters, conditions of model validity

In an SEA system, the dissipated and the exchanged power is represented by the damping and coupling loss factors that can be obtained analytically, experimentally or based on a finite element analysis. Several previous works have contributed to the establishment of these three approaches.

Langley and Heron [36] derived a method that enables the calculation of transmission coefficients of any plate/beam assembly. In their analysis, the dynamic stiffness matrix is adopted to minimize the algebraic manipulation required. Langley [37] later introduced the definition of weak coupling and defined the conditions under which a complex dynamic system may be reduced to SEA equations. The estimation of the coupling loss factors based on the wave approach was derived. Fahy and James [38] proposed a technique for the assessment of the strength of coupling between SEA subsystems based on theoretical analysis. Le Bot and

Cotoni [39] investigated the validity of coupled plates SEA model by introducing the diagrams of validity. The domain of validity is defined by constraining the appropriate dimensionless quantities, corresponding to the SEA assumptions such as weak coupling, sufficient number of modes, large modal overlap, equipartition of energy, diffuse field, rain-on-the-roof excitation. Bosmans et al. [40] presented two models for predicting wave transmission between thin orthotropic plates. The first one is based on the wave propagation in semi-infinite plates, the second one is based on the modal summation for finite plates. The results were compared to the L-junction of equivalent isotropic plates and good agreement was found. Wester and Mace [41] used the wave approach on two coupled plates and highlighted its advantages over the modal approach. They quantified the coupling strength and defined four distinct regimes of energy flow and storage to improve the estimates of input and coupling powers and coupling loss factors. Wöhle et al. [42] presented a method for calculating the coupling loss factors for a structure-borne sound transmission at a rectangular slab junction for incident bending, longitudinal and transverse waves. In a subsequent paper [43], they showed how the structure-borne sound transmission induced by forced bending waves should be considered in an SEA model. Díaz-Cereceda et al. [44] presented a procedure for obtaining SEA parameters numerically for two subsystems. Three separate ways of isolating the CLFs were explored and compared to an analytical solution. They found that the best option is to isolate the CLFs from the power balance of the second (unexcited) subsystem.

Patil and Manik [45] performed an optimization procedure using the theoretical equations for CLFs and a sensitivity analysis of differently coupled plates using direct differentiation and finite difference methods. It was found that the values of CLF depend on the coupling stiffness and the optimal values of CLF can contribute to reducing the response of a system. Simmons [46] used Finite Element Method to calculate the vibrational energies of L- and H-shaped structures. The energies are used to characterize the junction and find the corresponding SEA parameters.

2.2.1. Experimental SEA

The experimental determination of the SEA parameters based on the Power Injection Method (PIM) is introduced by De Langhe [47]. In PIM, measurement data is substituted into the power balance equation to find the damping and coupling loss factors.

Bies and Hamid [48] used the Power Injection Method to determine the loss factors of coupled plates and concluded that the steady state and the reverberant decay method lead to different results. The SEA parameters can be determined by the inversion of the power balance equation,

if the equations are well conditioned, meaning that the SEA model adequately represents the structure, and the injected power is measured with reasonable precision. James and Fahy [49] applied their previously proposed technique of coupling strength assessment to the experimental results of two plates coupled by a variable number of straps and two rooms coupled by an aperture. Bouhaj et al. [50] introduced the procedures of statistical description of measured power input, vibration energies and SEA parameters when using experimental SEA. Gu and Sheng [51] used an improved energy ratio method to estimate the coupling loss factors of a coupled structure. Hela Ladin et al. [52] presented concreate guidelines for performing the PIM and verified the influence of the number of measurement points. Bhagwan and Popuri [53] used the energy-level difference method to estimate the coupling loss factors and of various junctions and the effect of the tightening torque applied at the junction. They found that the coupling loss factors tend to increase with the tightening torque. Panuszka et al. [54] investigated L-shaped structures with different joint types and thickness ratios. They estimated the DLFs from reverberation time, the CLFs from the Power Injection Method and compared the results to analytical formulas. Kurosawa [55] used hybrid analytical-experimental SEA to obtain the damping and coupling loss factors for a full vehicle model. The damping was determined from the reverberation curve, the coupling loss factors were calculated from the energy ratio of two subsystem when one of them was excited and the influence of the others were considered. Trim parts, damping materials, seals, and leakages were also included in the model. Differences up to 2 dB could be observed between the experiment and predictions. Treszkai et al. [56] investigated nineteen different joining methods and compared experimental Power Injection Method to analytical SEA results.

2.2.2. Virtual SEA

The use of a prior finite element analysis for building up reduced energetic model and find the SEA parameters was introduced by Gagliardini et al. [57], [58]. Their proposed method, called Virtual SEA eliminates the need for expertise to build an SEA model. They obtained convincing results for a minivan floor, when comparing Virtual SEA to experimental methods.

Borello and Gagliardini presented the developments of the Virtual SEA method in Ref. [59]. The most time-consuming tasks were improved, making the method able to manage an as large as150 000-node vehicle body. It was also stated that the prediction quality largely depended on the FE model. Brandstetter et al. [60] applied a commercial implementation of the Virtual SEA approach in MSC Actran for a B-segment SUV. It was shown that frequency extrapolation extends the FE mesh validity by a factor of four. The Virtual SEA results were compared to

finite element modal frequency response simulations and validated. The vibration transfer paths were also investigated by visualizing the CLFs between the subsystems. The effectiveness of the Virtual SEA method to consider manufacturing uncertainties on a ladder-like structure, equipped by plates, was proven in Ref. [IV]. Although the low frequency discrepancies could only be improved by adding an approximate curvature to the plates, the mid- and high frequency correlation with measurement was satisfactory, even with the nominal geometry.

Duval et at. [61] presented a novel methodology that introduces curved poro-elastic trim parts in Virtual SEA using finite elements. The results of an air-borne Transmission Loss simulation of a firewall as well as the structure-borne vibro-acoustic responses were compared to measurements and showed promising agreement, although the integration of the trim FE simulation into the Virtual SEA process was challenging and needs to be improved.

2.3. SEA sub-structuring

In order to create an SEA model that fully respects the validity criteria imposed by the SEA theory, more advanced methods have been proposed to create SEA subsystems. Several papers in the literature employed clustering techniques to find the optimal partitioning of vibro-acoustic systems.

Magrans et al. [62] proposed a methodology for the automatic identification of subsystems based on the cluster analysis of the powers of the transfer matrix. They showed that the subsystems are clearly identified when high powers of the transfer matrix are considered. Their approach also provides a quantification of the coupling strength. The results were illustrated on plates coupled by springs and rooms connected by means of cavity. Gagliardini et al. [58] proposed a strategy based on the energetic transfer functions to identify SEA subsystems in a minivan floor. The analysis relies on two different finite element meshes, from which the course one was used to excite every node of the structure to obtain the transfer functions. For different frequency bands, different sub-structuring schemes were achieved. Totaro and Guyader [63] proposed a tool to aid valid SEA sub-structuring based on cluster analysis of energy transfer functions and Principal Component Analysis (PCA). They used their approach on an L-shaped plate, on an assembly of three plates and on a more complex shell structure. They also established the MIR (Mutual Inertia Ratio) index that indicates the best number of subsystems and correlates with the coupling strengths of the subsystems. Kovalevsky and Langley [64] developed an automated algorithm with two different strategies to recognize the deterministic FE and the highly random SEA components in a hybrid model based on a coarse FE model. They presented their results on a plate-stiffener structure and on a section of an aircraft. For the

former one, the results were consistent with the expectations, the panels were identified as distinct subsystems and the stiffeners as the master subsystem. The result of the aircraft section was not so clear, however with the application of the right post-processing method, the resulting decomposition seemed reasonable. Díaz-Cereceda et al. [65] proposed a methodology based on dividing the domain into cells and performing hierarchical clustering based on the system eigenmodes. The energy distribution for the cluster analysis was computed based on the averaged and normalized total energy at each cell. They used the correlation distance as the measure of energetic differences between the system cells. Using a set of eigenmodes eliminated the need for PCA, thus less calculations were required. The robustness of the method was presented on coupled plates and coupled acoustic rooms. Kassem et al. [66] presented a structural partitioning devoted to the medium frequency range and its application to a complex vehicle model. The methodology is based on the energy density field approach, presented in Ref. [67]. They proved that the effective partitioning of the system can be constructed for frequencies larger than the one given by the degree of separation. The methodology they presented could extend the validity of SEA models to the medium frequency range.

2.4. Damping layer optimization

The ultimate goal of vehicle NVH simulation is usually to reduce the noise inside the passenger compartment. Numerous works can be found in literature concerning the reduction of radiated sound power and panel vibration through finding the optimal location of damping layers.

Wodtke and Lamancusa [68] showed that the redistribution of unconstrained damping layers can reduce the radiated sound power of circular plates. Arenas and Hornig [69] proposed a method to numerically estimate the radiated sound power and showed that the thickness and stiffness of the unconstrained damping layers have significant effect on it. Their method is suitable for fast optimization purposes too. Subramanian, et. al., [70] developed a methodology to enhance the effectiveness of damping treatments in a vehicle structure. They used modal strain energy of the bare structure panel to identify the location and the size of the damping treatments. The numerical results were compared with laser vibrometer measurements. The road noise comparison showed that 2.5 dB(A) noise reduction could be achieved in the 200-400 Hz frequency range with the optimized configuration. The main advantages of this methodology according to the authors are its simplicity, reasonable accuracy, and that the computation takes less time than the experimental approaches. In addition, it can be used in the early stages of the design. Balmes and Germes [71] introduced a design strategy for the placement of viscoelastic treatments, with tools of the simulation for a full vehicle. They used

the frequency weighted average strain energy for the first 50 modes to determine the place of the damping treatments. This methodology can be used to optimize large models in the early design phase. Furukava, et. al. [72] compared three different passenger vehicle cases: Body-in-White, with asphalt pad and with liquid applied sprayable damper. They used experimental tools to determine the position of the damping materials and to reduce the application area of them. The investigated frequency range was 0-1 kHz, and they divided the vehicle components to different subsystems, and investigated the vibroacoustic behavior in third-octave bands. They used acceleration values to determine the position of the damping materials. As a result of their work, the application area reduced 26.3% and the added material was 53.7% of the original setup. The main drawback of this method is that it needs to have access to a prototype. Comesana and Tatlow [73] investigated the particle velocity maps of the different car components. This way they defined the critical areas where the damping materials were applied, then the measurement was repeated, and the results were compared. Different material types, position and thicknesses were used to achieve the highest Particle Velocity Level difference in dB(A) compared to the undamped structure. The authors proposed a quick and efficient way to characterize the vibro-acoustic behavior of the car structure, however, the main problem of this method is that the measurement process requires a real car structure. Hara and Özgen [74] investigated the performance of the foam cored sandwich structures instead of damping treatments on the panels of the vehicle structures e.g., on the floor, on the firewall. As the results showed the foam cored sandwich material had the same bending stiffness performance as the sheet metal panels with at least 50% less weight. The authors recommended a sandwich structure with a viscoelastic core instead of a sheet metal with added damping treatments, because it could reduce weight by 60-70%, while keeping the same damping performance. Guellec et at. [75] performed a complete trim package optimization for a passenger car floor panel in a two-phase design process. In the first step, they used a topology optimization algorithm to modify the beads and embossments of the panel. Then in the second stage, they optimized the bitumen and porous material properties to achieve the best possible configurations with optimal overall damping and with optimized mass. With these two configurations, they managed to achieve 2.8 dB and 2.5 dB RMS reduction of the averaged PSD pressure at the microphones in the cavity, respectively.

2.5. Summary of literature review and research gaps

The purpose of the literature review was to provide a broad overview of the state-of-the-art simulation methods available in the field of vehicle acoustics. It can be concluded that Finite

Element Method is the most widely used approach, because of its accuracy and capability in detailed modeling. However, as the frequency range of interest shifts higher, above 400 Hz, its limitations, resulting from the increased number of degrees of freedom due to the need for increased mesh density, became obvious. Today's current full vehicle models can only be used at enormous computational costs, especially when trim parts are also considered. Statistical Energy Analysis (SEA), on the other hand, has been proven to effectively manage high-frequency computations, but its limitations of the frequency range lie in the restrictions of the model building. This means that in order to determine the CLF and DLF values for each subsystem, one has to rely either on simplified analytical formulas, which might not be suitable for more complex structures, or has to perform a Power Injection Method (PIM) via an expensive set of experiments, requiring the access to a prototype a-priori of the simulations. This prevents the usage of the method in the early stages of design. More recently proposed methods aimed to combine the advantages of FEM and SEA. In the hybrid FE-SEA approach, the definition, and the coupling of all the statistical subsystems to the master deterministic subsystem remains unresolved and requires further complex analyses. A relatively new method, the Virtual SEA, promises to utilize the advantages of all above methods: in this approach, the CLF and DLF values of the SEA simulation are deduced from FEM simulations, by performing the PIM virtually. This shows promising results and extends the SEA model validity towards the lower frequency bands. The advantages of this method lie in that the so-obtained SEA parameters do not require conducting time-consuming measurements on a prototype, nor using analytical formulas for different junctions. However, even regarding Virtual SEA, there are research gaps, especially in the mid-frequency range (400 – 1 000 Hz) of full vehicle acoustic simulations. Based on the review of literature above, the following points appear to be unaddressed in the literature:

- Virtual SEA is assumed to be able to consider the coupling and damping effects of various junction types through the proper finite element representation of the connection. However, the CLFs obtained through the Virtual SEA approach for various connection types have not been validated, and effects of the finite element connection modeling parameters have not been explored.
- The subsystems of a Virtual SEA model are required to have certain attributes in order to satisfy the general assumptions of SEA theory, such as they are weakly coupled, have sufficient modal density and homogenous energy distribution, and they fulfil the reciprocity relation. Various sub-structuring techniques have already been proposed, but

no prior investigation has been made for comparing different clustering algorithms and for exploring their effect on the accuracy of the model.

- There is no study in the literature that presents a full-scale trimmed body vehicle model inclusive an internal cavity coupled to the structure through trim parts, modelled as poro-elastic materials. The fluid-structure coupling, and the consideration of the trim parts are yet to be validated.
- Several studies have proved that the redistribution of damping layers on a car chassis can effectively reduce panel vibrations, but none of the proposed methods is able to find the optimal locations for a given frequency range without performing additional complex computations and analyses.

3. GOALS OF THE DISSERTATION

Based on the literate review and the identified research gaps, the main goal of present work is in general to assess and enable the Virtual SEA simulation method for the mid- and high frequency full vehicle acoustic simulations. The specific goals are:

1) To prove that the Virtual SEA approach is capable of considering the damping and coupling effects of different junction types through the proper finite element representation of the connection. In relation to this, the present work aims to explore the influence of the finite element modeling parameters on the coupling and damping loss factors obtained via the virtual power injection method.
2) To demonstrate that the accuracy of the model depends on its sub-structuring and its compliance with the assumptions of SEA theory. Consequently, the goal is to propose a method that allows to create subsystems in a conscious and consistent way (instead of an ad-hoc, or experience-based approach) and provides the best possible subdivision of the model in terms of accuracy and SEA model validity point of view. To achieve this, a new method also needs to be proposed that allows the comparison of different subdivisions.
3) To perform a full vehicle trimmed body acoustic simulation in Virtual SEA, including an internal cavity as well as trim parts consisting of poro-elastic materials (PEM), and to validate these with experiments. This would provide validation of the specific approaches that enable the calculation of fluid-structure coupling and the consideration of the trim effects.
4) Last, the present work aims to investigate how the energetic quantities computed during a Virtual SEA solution can be used for the NVH optimization of a vehicle chassis.

Before proceeding to working out solutions to these goals, a comprehensive review of the theoretical background of the simulation methods applied in the present work will be discussed in detail.

4. THEORETICAL OVERVIEW OF THE SIMULATION METHODS

Recall, that Virtual SEA simulations are essentially SEA simulations, in which the Coupling Loss Factor (CLF) and Damping Loss Factor (DLF) values are obtained not via an experimental Power Injection Method (PIM) method or from analytical formulae, but from a virtually performed PIM on a finite element simulation model. The Virtual SEA simulation results that will be presented in this Dissertation have uniformly been generated in the commercial acoustic simulation software MSC Actran by Hexagon. The required finite element input data was provided by the commercial general purpose finite element solver MSC Nastran by Hexagon in all cases. Thus, the theoretical review conducted in this chapter is based on the respective solver's theory guides.

4.1. Dynamic Finite Element Analysis

This chapter introduces the basics of dynamic finite element analysis and characterizes the analysis types based on Ref. [76]. Dynamic analyses differ from static analyses because the applied loads and the system response are functions of time or frequency. Figure 4 shows the simplest dynamic Single Degree of Freedom (SDOF) system.

m	=	mass (inertia)
b	=	damping (energy dissipation
k	=	stiffness (restoring force)
p	=	applied force
u	=	displacement of mass
$\dot{u}$	=	velocity of mass
$\ddot{u}$	=	acceleration of mass

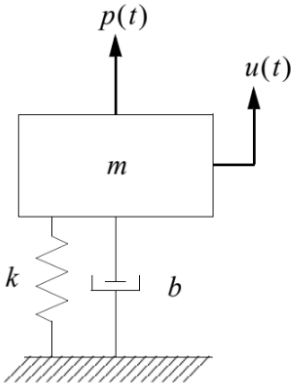

Figure 4. Dynamic SDOF system [76].

In an SDOF system, the time varying system displacement is described by one component of motion $u(t)$. Mass and damping are associated with the motion of the system, thus the degrees of freedom associated with mass or damping are called dynamic degrees of freedom. On the other hand, the degrees of freedom associated with stiffness are called static degrees of freedom. The four basic components are the mass, energy dissipation (damper), spring (resistance) and applied force. The equation of motion for a SDOF system is then given by:

$$m\ddot{u}(t) + b\dot{u}(t) + ku(t) = p(t) \tag{1}$$

The equation of motion describes the forces acting on the system. On the left-hand side, internal forces account for inertial force, viscous damping force and elastic force, respectively. The right-hand side accounts for the external force (applied load). In frequency response analyses, the excitation is applied in the frequency domain, to compute steady-state oscillatory response of the system. There are two possible ways of performing a frequency response analysis, depending on the system degrees of freedom: direct frequency response and modal frequency response.

4.1.1. Direct Frequency Response

In direct frequency response analysis, the system response is computed for discrete frequencies and the system response $\{u(\omega)\}$ is described by physical coordinates. For an MDOF system with the harmonic excitation load and system responses introduced as complex vectors, the damped forced vibration equation of motion can be written as:

$$[\mathbf{M}]\{\ddot{x}(t)\} + [\mathbf{B}]\{\dot{x}(t)\} + [\mathbf{K}]\{x(t)\} = \{P(\omega)\}e^{i\omega t} \tag{2}$$

Assuming a harmonic solution in the form of:

$$\{x\} = \{u(\omega)\}e^{i\omega t} \tag{3}$$

And by back substituting into Equation (2) one gets:

$$-\omega^2[\mathbf{M}]\{u(\omega)\}e^{i\omega t} + i\omega[\mathbf{B}]\{u(\omega)\}e^{i\omega t} + [\mathbf{K}]\{u(\omega)\}e^{i\omega t} = \{P(\omega)\}e^{i\omega t} \tag{4}$$

After simplifying by $e^{i\omega t}$, yields:

$$[-\omega^2\mathbf{M} + i\omega\mathbf{B} + \mathbf{K}]\{u(\omega)\} = \{P(\omega)\} \tag{5}$$

Then, the equation of motion is solved by inserting the forcing frequency and by using complex arithmetic. From the above equation, by introducing $[\mathbf{Z}]$, the dynamic system matrix of the system, can be obtained as:

$$\{u\} = [\mathbf{Z}]^{-1}\{P\} = [\mathbf{H}]\{P\} \tag{6}$$

where $[\mathbf{H}]$ is referred as the Frequency Response Function (FRF) of the system.

4.1.2. Modal Frequency Response

Modal frequency response analysis is an alternative approach for computing the frequency response of a system. It uses the mode shapes to uncouple the equations and to reduce the size of the problem to solve. A modal approach starts with the extraction of the system modes, which requires a special reduced form of the equation of motion with no damping and applied loads:

$$[\mathbf{M}]\{\ddot{u}\} + [\mathbf{K}]\{u\} = 0 \tag{7}$$

Assuming a harmonic solution if the form of:

$$\{u\} = \{\Phi\}sin\omega t \tag{8}$$

where $\{\Phi\}$ is the eigenvector or mode shape. After substituting and simplifying, Equation (9) is obtained as:

$$([\mathbf{K}] - \omega^2[\mathbf{M}])\{\Phi\} = 0 \tag{9}$$

If $det([\mathbf{K}] - \omega^2[\mathbf{M}]) \neq 0$, a non-trivial solution exists for a set of discrete ω_i^2 and for each of them, there is a $\{\Phi_i\}$ that satisfies the equation. These are called eigenvalues and eigenvectors, and the possible number of them equals to the number of dynamic degrees of freedom in the system. The eigenvectors are orthogonal, meaning that one shape cannot be obtained through the linear combination of the others. At any given time, the deflected shape of a linear elastic structure in free or forced vibration can be described by the linear combination of all of its normal modes:

$$\{u\} = \sum_i \{\Phi_i\}\xi_i \tag{10}$$

Several different approaches exist for real eigenvalue extraction. The Lanczos method is usually recommended to use since it combines the best of the other methods and provides great accuracy in finding the roots of the eigenvalue problem. For vehicle acoustic simulations, other methods, such as the Automated Multilevel Substructuring (AMLS) and Automated Component Mode Substructuring (ACMS) are preferred due to their performance advantages [77]. After the modal calculation, the variables of the system are transformed from physical coordinates $\{u(\omega)\}$ to modal coordinates $\{\xi(\omega)\}$ by assuming:

$$\{x\} = [\mathbf{\Phi}]\{\xi(\omega)\}e^{i\omega t} \tag{11}$$

After substituting and simplifying, the undamped forced equation of motion is given by:

$$-\omega^2[\mathbf{M}][\mathbf{\Phi}]\{\xi(\omega)\} + [\mathbf{K}][\mathbf{\Phi}]\{\xi(\omega)\} = \{P(\omega)\} \tag{12}$$

To uncouple the equations, pre-multiply by $[\boldsymbol{\phi}]^T$ to obtain:

$$-\omega^2[\mathbf{\Phi}]^T[\mathbf{M}][\mathbf{\Phi}]\{\xi(\omega)\} + [\mathbf{\Phi}]^T[\mathbf{K}][\mathbf{\Phi}]\{\xi(\omega)\} = [\mathbf{\Phi}]^T\{P(\omega)\} \tag{13}$$

Using the orthogonality property of the system mode shapes, which diagonalize the system matrices (generalized mass, stiffness), the uncoupled equation of motion can be obtained:

$$-\omega^2 m_i\xi_i(\omega) + k_i\xi_i(\omega) = p_i(\omega) \tag{14}$$

where m_i, k_i, p_i are the i^{th} modal mass, stiffness, and force, respectively, corresponding to the elements in the diagonal of the diagonalized system matrices. The uncoupled equation is much faster to solve than direct methods since it is a series of SDOF systems. The physical responses of the system are retrieved in complex form using Equation (11) once the individual modal responses are found. If damping is present, so when $[\mathbf{B}]$ exists, or structural damping is used in the form of complex stiffness matrix, the mode shapes generally do not diagonalize the generalized damping and stiffness matrices. The equation of motion remains coupled, and the

coupled equation is solved by the direct frequency approach in terms of modal coordinates. The uncoupled equation of motion can be maintained by using modal damping, so that each mode has a damping of $b_i = 2m_i\omega_i\zeta_i$, written as:

$$-\omega^2 m_i\xi_i(\omega) + +i\omega b_i\xi_i(\omega) + k_i\xi_i(\omega) = p_i(\omega) \tag{15}$$

where ζ_i is damping ratio. If the coupled form is used, the number of modes extracted for the solution is typically much less than the number of physical degrees of freedom, so the costs of solving the coupled equation in modal coordinates is typically much less than having physical coordinates.

4.1.3. Coupled structure-fluid analysis

In a coupled structure-fluid analyses, an arbitrary-shaped fluid is coupled to the structure modeled by conventional 3D solid elements with acoustic properties and material data. Each grid point has one pressure degree of freedom in the acoustic domain. The equations used for solving an acoustic media are based on small motion theory, with negligible convective momentum terms and locally linear pressure-density relationship. The detailed derivation of the equations can be found in Ref. [76]. The final form of the coupled fluid structure equation is given by:

$$\begin{bmatrix} \mathbf{M_s} & \mathbf{0} \\ -\mathbf{A^T} & \mathbf{M_f} \end{bmatrix} \begin{Bmatrix} \ddot{u}_s \\ \ddot{p} \end{Bmatrix} + \begin{bmatrix} \mathbf{B_s} & \mathbf{0} \\ \mathbf{0} & \mathbf{B_f} \end{bmatrix} \begin{Bmatrix} \dot{u}_s \\ \dot{p} \end{Bmatrix} + \begin{bmatrix} \mathbf{K_s} & \mathbf{A} \\ \mathbf{0} & \mathbf{K_f} \end{bmatrix} \begin{Bmatrix} u_s \\ p \end{Bmatrix} = \begin{Bmatrix} P_s \\ P_f \end{Bmatrix} \tag{16}$$

where the submatrices denoted by s are generated for the structural elements, submatrices denoted by f subscript are generated for the fluid elements. These are the acoustic fluid mass matrix $\mathbf{M_f}$, the acoustic fluid damping matrix $\mathbf{B_f}$, the acoustic fluid stiffness matrix $\mathbf{K_f}$ and the acoustic fluid load vector P_f. Additionally, A submatrix denotes the acoustic fluid boundary matrix, responsible for the structure-fluid coupling.

4.2. Poro-Elastic Materials

Acoustic trim bodies containing poro-elastic materials (porous elastic solid skeleton saturated by compressible fluid) have major influence on the vibro-acoustic behavior of coupled systems [16] [75]. The theory of deformation and the propagation of elastic waves in the poro-elastic materials has been established by M. A. Biot in 1941 [78] and 1956 [79], [80]. To consider the effect of these materials in finite element simulations, they can be characterized by the Biot parameters. According to Biot's theory, poro-elastic materials consist of two phases, described by the material properties listed in Table 1.

Table 1. Biot parameters of porous material characterization.

Fluid phase parameters	Fluid phase density, ρ_f
	Celerity (speed of sound), c_f
Solid phase parameters	Solid phase density, ρ_s
	Young's modulus, E
	Poisson ratio, ν
	Structural damping coefficient, η_s
Coupling parameters	Porosity, ϕ
	Resistivity, σ
	Tortuosity, α_∞
	Viscous characteristic length, Λ
	Thermal characteristic length, Λ'

Biot's Lagrangian model for propagation of elastic waves in a porous solid is based on the potential energy of deformation. It is assumed that the fluid is compressible and relative motion between the fluid and the solid can occur above a certain frequency, depending on the kinematic viscosity of the fluid and the size of the pores. In vehicle acoustic applications, the maximal frequency is typically below that specific frequency, so Biot's theory for the low frequencies is adequate to discuss. The model assumes that the walls of the pores are impervious, their size is around an average value and the thermo-elastic effects are disregarded. Two types of dilatational (compressional) waves and one rotational (shear) wave are considered in the theory [79]. In the original work of Biot, the displacements of the two phases are coupled, while in later theories [10], [11], mixed pressure-displacement formulations are used for describing the equations of wave propagation. This approach has several advantages over the displacement-coupled formulations, such as reduced number of degrees of freedom and easier transmission at the fluid-porous interface, thus it has been implemented in most NVH finite element solvers via the Reduced Impedance Method (RIM). As described in Ref. [81], the trim component is considered as an impedance matrix and condensed on the interface nodes of the structure and the fluid domain. The frequency-dependent reduced impedance matrix is projected on the structure and fluid modal bases.

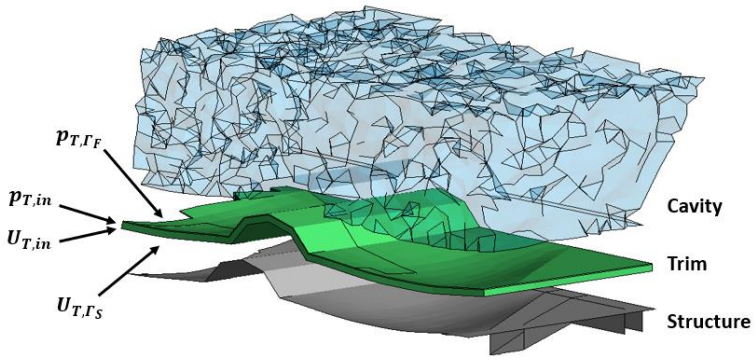

Figure 5. Degrees of freedom of a trim component in Reduced Impedance Method.

First, consider a trim part coupled to the structure along Γ_S and coupled to the cavity along Γ_F as Figure 5 shows. The trim displacement and pressure degrees of freedom are given by:

$$(U_T, p_T)^T = (U_{T,in}, p_{T,in}, U_{T,\Gamma_S}, p_{T,\Gamma_F})^T \tag{17}$$

The assembled impedance matrix of the trim can then be expressed as:

$$Z_T = \begin{pmatrix} [Z_{in}] & [Z_{in,\Gamma}] \\ [Z_{\Gamma,in}] & [Z_\Gamma] \end{pmatrix} \tag{18}$$

To eliminate the internal degrees of freedom, the impedance matrix is reduced to the coupling degrees of freedom in the following form:

$$Z_{T,red} = Z_T - Z_{\Gamma,in} * {Z_{in}}^{-1} * Z_{in,\Gamma} \tag{19}$$

After the modal projection, one gets:

$$\tilde{Z}_{T,red}(\omega) = \begin{pmatrix} [\boldsymbol{\Phi}_{\boldsymbol{\Gamma_S}}]^T & 0 \\ 0 & [\boldsymbol{\Phi}_{\boldsymbol{\Gamma_F}}]^T \end{pmatrix} \cdot Z_{T,red} \cdot \begin{pmatrix} [\boldsymbol{\Phi}_{\boldsymbol{\Gamma_S}}] & 0 \\ 0 & [\boldsymbol{\Phi}_{\boldsymbol{\Gamma_S}}] \end{pmatrix} \tag{20}$$

The obtained modal impedance matrix provides the contribution of the trim part in modal coordinates and can be used in the coupled modal equation of the three-domain system. The drawback of this approach is that the physical mesh of the trim parts has to be created, and for each frequency, a matrix inversion has to be performed to eliminate the trim internal degrees of freedom, according to Equation (19). This raises the computational costs drastically and limits the maximal frequency that can be reached with the simulations [16], [17].

4.3. Statistical Energy Analysis

Statistical Energy Analysis is a widely used energy-based method for vibro-acoustic analyses of complex structures, introduced by Lyon and Maidanik [18] and Smith [19]. It is suitable for high-frequency analyses, where the response of the structure can only be described effectively by energetic methods. In SEA, the system is first divided into subsystems and a power balance equation is solved to retrieve their energy levels. According to Langley [37] and Le Bot and

Cotoni [39], the subsystems must satisfy certain assumptions, such as the subsystems are weakly coupled, meaning the dissipated power is higher than the exchanged power between others; the energy distribution in the subsystems is homogenous; the modal density and modal overlap is sufficient, and the reciprocity relation is fulfilled. If these conditions are met, the power balance equation for subsystem i can be written as derived in Ref. [81]:

$$P_{in}^{i} = P_{diss}^{i} + \sum_{i \neq j} P_{c}^{i,j} \tag{21}$$

where P_{in}^{i} equals the total injected power, $P_{c}^{i,j}$ is the exchanged power between subsystem i and j. P_{diss}^{i} is the dissipated power from subsystem i given by:

$$P_{diss}^{i} = \eta_i \omega E_i \tag{22}$$

where η_i is the damping loss factor, ω is the center frequency of the considered frequency band, E_i is the subsystem energy. As Lyon and Maidanik [18] showed, the energy flow between subsystems is proportional to their vibration energy difference. By assuming that the vibrational energy is equally distributed in each subsystem among its modes, and introducing the reciprocity relation,

$$n_1 \eta_{12} = n_2 \eta_{21} \tag{23}$$

the exchanged power between the subsystems can be written as:

$$P_{c}^{i,j} = \omega(\eta_{ij} E_i - \eta_{ji} E_j) \tag{24}$$

where n_1 and n_2 are the modal densities, η_{ij} and η_{ji} are the coupling loss factors. The general form of the power balance equation for any number of subsystems can be written as:

$$P_{in}^{i} = \eta_i \omega E_i + \sum_{i \neq j} \omega(\eta_{ij} E_i - \eta_{ji} E_j) \tag{25}$$

or in compact form:

$$\boldsymbol{P} = \omega[\boldsymbol{\eta}]\boldsymbol{E} \tag{26}$$

Figure 6 shows a schematic SEA power balance model for 2 subsystems.

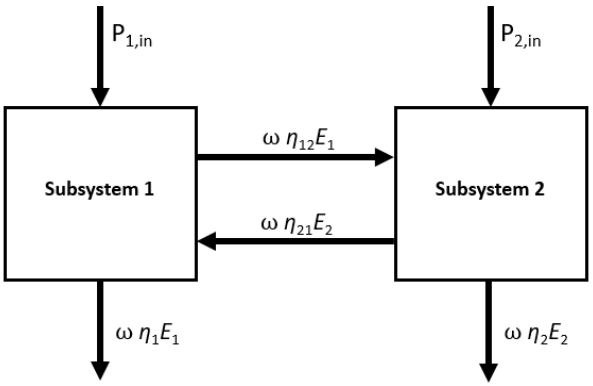

Figure 6. Schematic representation of the SEA power balance model [56].

4.3.1. Analytical SEA

Determining the correct values of the coupling and damping loss factors in the loss matrix, $[\boldsymbol{\eta}]$ that drive the power balance equations one of the most challenging parts of an SEA simulation. There are several different approaches to consider, such as analytical SEA, experimental SEA, and Virtual SEA. Analytical SEA, as its name suggests, uses analytical formulations based on the wave propagation or on the modal summation approach [41] to estimate the coupling conditions between any two neighboring subsystems inferred by the transmission coefficient of the junction. This means that the analytical formulation for the Coupling Loss Factors (CLF) can only be derived for physically connected subsystems for which these formulas are available e.g., simple connections for regular geometrical objects [30]. The transmission of elastic waves through plate/beam junctions is derived in Ref. [36]. In analytical SEA, energy exchanges associated with all wave types can be considered. However, indirect coupling loss factors, often associated with global modes, cannot be calculated [81].

4.3.2. Power Injection Method

The SEA loss matrix can also be obtained by experimental measurements. In the Power Injection Method, first introduced by De Langhe [47], the loss matrix is calculated by substituting the $\boldsymbol{P}$ and $\boldsymbol{E}$ values in the SEA power balance equation. The most convenient way to do so is to excite all subsystems one by one while measuring the injected power and the response of all subsystems. According to Ref. [81], the injected power to a subsystem can be calculated according to the following equation:

$$P_{in} = F^2 \,\mathrm{Re}\{Y\,(\omega)\} \tag{27}$$

where F is the excitation force and Y is the driving point mobility. The kinetic energy of the subsystem is given by:

$$E = m < v^2 > \tag{28}$$

where m is the mass, and $< v^2 >$ denotes the spatially averaged squared vibrational velocity of the subsystem. In each iteration for n subsystems, frequency dependent power P_n is injected into subsystem n (each subsystem individually), and the frequency dependent energy response of all subsystems $E_{n1} \ldots E_{nn}$ are monitored. After iterating on all subsystems, the SEA power balance equation can be assembled: on the left-hand side, a diagonal matrix $\boldsymbol{P}$ corresponding the measured injected powers and on the right-hand side, a full matrix of $\boldsymbol{E}$ corresponding to the column vectors of the measured subsystem energies, obtained for each excitation, as shown by Equation (29):

$$\begin{bmatrix} P_1 & \cdots & 0 \\ \vdots & \ddots & \vdots \\ 0 & \cdots & P_n \end{bmatrix} = \omega[\boldsymbol{\eta}] \begin{bmatrix} E_{11} & \cdots & E_{n1} \\ \vdots & \ddots & \vdots \\ E_{1n} & \cdots & E_{nn} \end{bmatrix} \tag{29}$$

From the above equation, the loss matrix $[\boldsymbol{\eta}]$ can be obtained by a simple matrix inversion for each frequency band. It should be noted that this method considers energy exchanges associated with only bending waves and not with longitudinal or shear waves. It is also a drawback of this method that it needs access to a prototype to perform the measurements on and it can require extreme amounts of measurements and man hours depending on the size of the structure [81].

4.4. Virtual SEA

The most recent approach to obtain the SEA loss matrix is the Virtual SEA method, first introduced by Gagliardini et al. [57], [58]. They used finite element calculations to build up an energy distribution model for the virtual power injection method. Based on the modal representation of the vibro-acoustic model, the distribution matrices enable the computation of energetic quantities on element patch levels i.e., k set of elements. According to the description provided in Ref. [81], considering an element patch P_k, the associated mass and stiffness distribution matrices $(\mathbf{M}_k, \mathbf{K}_k)$ are obtained by projecting the set of element level mass and stiffness matrices $(\boldsymbol{M}^{(e)}, \boldsymbol{K}^{(e)})$ on the modal basis $\boldsymbol{\Phi}$:

$$\mathbf{M}_k = \boldsymbol{\Phi}^{\mathrm{T}} \sum_{e \in P_k} \boldsymbol{M}^{(e)} \boldsymbol{\Phi} \tag{30}$$

$$\mathbf{K}_k = \boldsymbol{\Phi}^{\mathbf{T}} \sum_{e \in P_k} \boldsymbol{K}^{(e)} \boldsymbol{\Phi} \tag{31}$$

A generic kinematic quantity expressed in modal coordinates as: $\boldsymbol{X}(\omega) = \boldsymbol{\Phi}\vec{\alpha}(\omega)$. Since energetic quantities generally takes the expression $\boldsymbol{X}(\omega)^H \boldsymbol{D}_k \boldsymbol{X}(\omega)$, it can be rewritten as $\vec{\alpha}(\omega)^H \boldsymbol{D}_k \vec{\alpha}(\omega)$ where $\boldsymbol{D}_k$ is either the mass or stiffness distribution matrix of element patch P_k. Thus, the distribution matrices can be directly used to calculate energetic quantities, as derived in Ref. [81]. The injected power is expressed as:

$$\widetilde{W}_i = \frac{\omega}{2} Im(\vec{\alpha}(\omega)^H \boldsymbol{\Phi}^{\mathrm{T}} \boldsymbol{f}(\omega)) \tag{32}$$

The potential and kinetic energies are expressed as [81]:

$$\tilde{V}_k = \frac{1}{4} \vec{\alpha}(\omega)^H \, \mathbf{K}_k \vec{\alpha}(\omega) \tag{33}$$

$$\tilde{T}_k = \frac{\omega^2}{2} \vec{\alpha}(\omega)^H \mathbf{M}_k \vec{\alpha}(\omega) \tag{34}$$

And the dissipated power is given by [81]:

$$\widetilde{W}_d = \frac{\eta\omega}{2} \vec{\alpha}(\omega)^H \, \mathbf{K}_k \vec{\alpha}(\omega) \tag{35}$$

Once the energy distribution model is built up, it can be used for the power injection method, meaning exciting each subsystem one by one, while monitoring the response in all the other

subsystems, exactly as in experimental SEA. However, this method combines the advantages of the previously mentioned approaches, but without their limitations and challenges: all of the wave types can be considered, no difficulties caused by measurements and any complex geometry can be assessed. Furthermore, indirect CLFs are considered to ensure the global model power balance. The so obtained coupling matrix should approximate the SEA assumptions as close as possible even in the mid-frequency range and it only requires a finite element modal analysis to be available [81]. Fluid-structure coupling

The virtually performed PIM in Virtual SEA only provides coupling loss factors between subsystems, that belong to the same physical component, either structure or fluid. In MSC Actran's Virtual SEA module, the coupling between different physical objects is calculated by the Statistical Modal Energy Distribution Analysis (SmEdA) approach, introduced by Maxit et al [82], [83]. In SmEdA, the energy exchange between neighboring subsystems is described without the limitation of the modal energy equipartition assumption. The coupling loss factors based on their model depend on the interaction of modal work of mode pairs given by [81]:

$$\mathcal{W}_{pq} = \int_S W_q \sigma_p n \mathrm{d}S \tag{36}$$

Where shape W_q is the q^{th} displacement mode shape of the uncoupled-free structure subsystem and σ_p is the p^{th} stress mode shape of the uncoupled-blocked fluid subsystem. S denotes the surface between the two subsystems and n is its unit normal vector. It should be noted that the integral over the surface indicates that only direct CLFs can be expressed with the SmEdA approach. For expressing the CLF between the two subsystems, all the interaction modal work terms of all the resonant mode pairs are considered in the frequency range of interest, according to [81]:

$$\eta_{ij} = \frac{1}{N_i \omega_c} \sum_{p=1}^{N_i} \sum_{q=1}^{N_j} \left[\frac{\left(\mathcal{W}_{pq}\right)^2}{\omega_p^2 M_p M_q} \left(\frac{\Delta_p \omega_q^2 + \Delta_q \omega_p^2}{\left(\omega_p^2 - \omega_q^2\right)^2 + \left(\Delta_p + \Delta_q\right)\left(\Delta_p \omega_q^2 + \Delta_q \omega_p^2\right)} \right) \right] \tag{37}$$

where $\mathcal{W}_{pq}$ is the modal work of the p^{th} and q^{th} resonant mode pairs, N_i and N_j are the number of resonant modes in the frequency band with the center frequency ω_c, ω_p and ω_q are the natural frequencies, Δ_p and Δ_q are the modal damping bandwidths, M_p and M_q represent the modal mass of mode p and q [81].

4.4.1. Trim modelling in Virtual SEA

In MSC Actran's Virtual SEA module, the effect of the trim bodies is considered by updating the SEA parameters that have already been calculated via the virtual PIM and the SmEdA. According to Ref. [81], the method relies on the analytical formulation of equivalent transfer admittance of a layer-structured trim model.

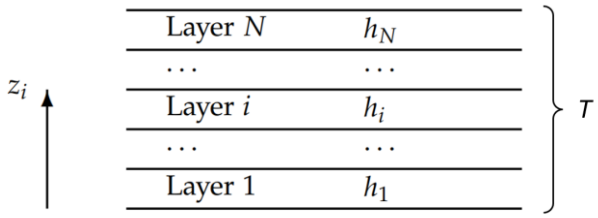

Figure 7. Layered trim structure [81].

Figure 7 shows a trim model that has a sequence of N layers, each with a scaled thickness h_i and certain material properties, describing a fluid, a solid or a porous domain. The scaled thickness of layer i $(1 \leq i \leq N)$ is defined by [81]:

$$h_i = t_i + (f_i t_i) + \frac{T - \sum_1^N t_i}{\sum_1^N f_i t_i} \tag{38}$$

where t_i and f_i are the thickness and scaling factor of layer i and T is the total thickness of the trim part. This formula mimics the behavior of combining springs with certain length and stiffness, stretched to a total thickness T. Figure 8 shows an example of a solid and an acoustic layer stacked. The analytical transfer admittance matrix of each layer associated with the degrees of freedom at the top and the bottom in the normal direction is calculated [81].

...	...
Layer $i+1$	$\sigma_n^{\mathrm{t}}, \sigma_t^{\mathrm{t}}, u_n^{\mathrm{t}}, u_t^{\mathrm{t}}$ $\sigma_n^{\mathrm{b}}, \sigma_t^{\mathrm{b}}, u_n^{\mathrm{b}}, u_t^{\mathrm{b}}$
Layer i	$v_n^{\mathrm{t}}, p^{\mathrm{t}}$ $v_n^{\mathrm{b}}, p^{\mathrm{b}}$
...	...

Figure 8. Degrees of freedom of a solid and an acoustic layer [81].

The solid layer has normal and tangent stress $(\sigma_n^t, \sigma_t^t, \sigma_n^b, \sigma_t^b)$ and displacement $(u_n^t, u_t^t, u_n^b, u_t^b)$ degrees of freedom at the top and at the bottom, the acoustic layer has normal velocity (v_n^t, v_n^b) and pressure (p^t, p^b). The transfer admittance matrix describes the relation of the top and bottom degrees of freedom in the normal direction. For example, the relation for the acoustic layer written as [81]:

$$\begin{bmatrix} v_n^t \\ v_n^b \end{bmatrix} = T \begin{bmatrix} p^t \\ p^b \end{bmatrix} \tag{39}$$

that has a transfer admittance matrix of [81]:

$$T = \frac{1}{i\rho\omega}\begin{bmatrix} \frac{\cos(hk)}{\sin(hk)} & \frac{-1}{\sin(hk)} \\ \frac{-1}{\sin(hk)} & \frac{\cos(hk)}{\sin(hk)} \end{bmatrix} \tag{40}$$

where $k = \omega/c$ is the wave number with the angular frequency ω, and the speed of sound c; and h is the scaled thickness of the layer. In this procedure, transverse coupling between degrees of freedom is neglected, but in vehicle acoustic applications, bending waves having displacement component in normal direction to the surface are mainly responsible for the structure-borne noise radiation. The total transfer admittance of the trim part is assembled from the analytically constructed transfer admittance matrices of each layer. The presence of a trim modifies the neighboring structure and fluid DLFs to account for the damping and absorption effects as well as the fluid-structure CLFs to account for the insulation effect. The structural DLFs are modified by a factor proportional to the damping part of the transfer admittance projected on the subsystem modes. The increase in the DLFs of acoustic subsystems is directly proportional to the random incident absorption coefficient α_{st} of the trim, written as [81]:

$$\eta_i(\omega) = \frac{\alpha_{st}(\omega) c_i S_i}{4 V_i \omega} \tag{41}$$

with α_{st} defined by the integral of the oblique incidence sound absorption coefficient $\alpha(\Theta)$ from $\Theta = 0\ to\ \pi/2$ [81]:

$$\alpha(\Theta) = \frac{4Re(\zeta)\cos(\Theta)}{|\zeta|^2 cos^2(\Theta) + 2Re(\zeta)\cos(\Theta) + 1} \tag{42}$$

In the above expression, c_i is the speed of sound, S_i is the trimmed surface, V_i is the volume of the acoustic subsystem, ζ is the normal acoustic impedance corresponding to the analytical transfer admittance. The absorption effect of the trim on the fluid-structure CLFs are accounted as a multiplier of the interaction modal work $\mathcal{W}_{pq}$ in Equation (36) [81]. Figure 9 shows the general workflow of a Virtual SEA simulation.

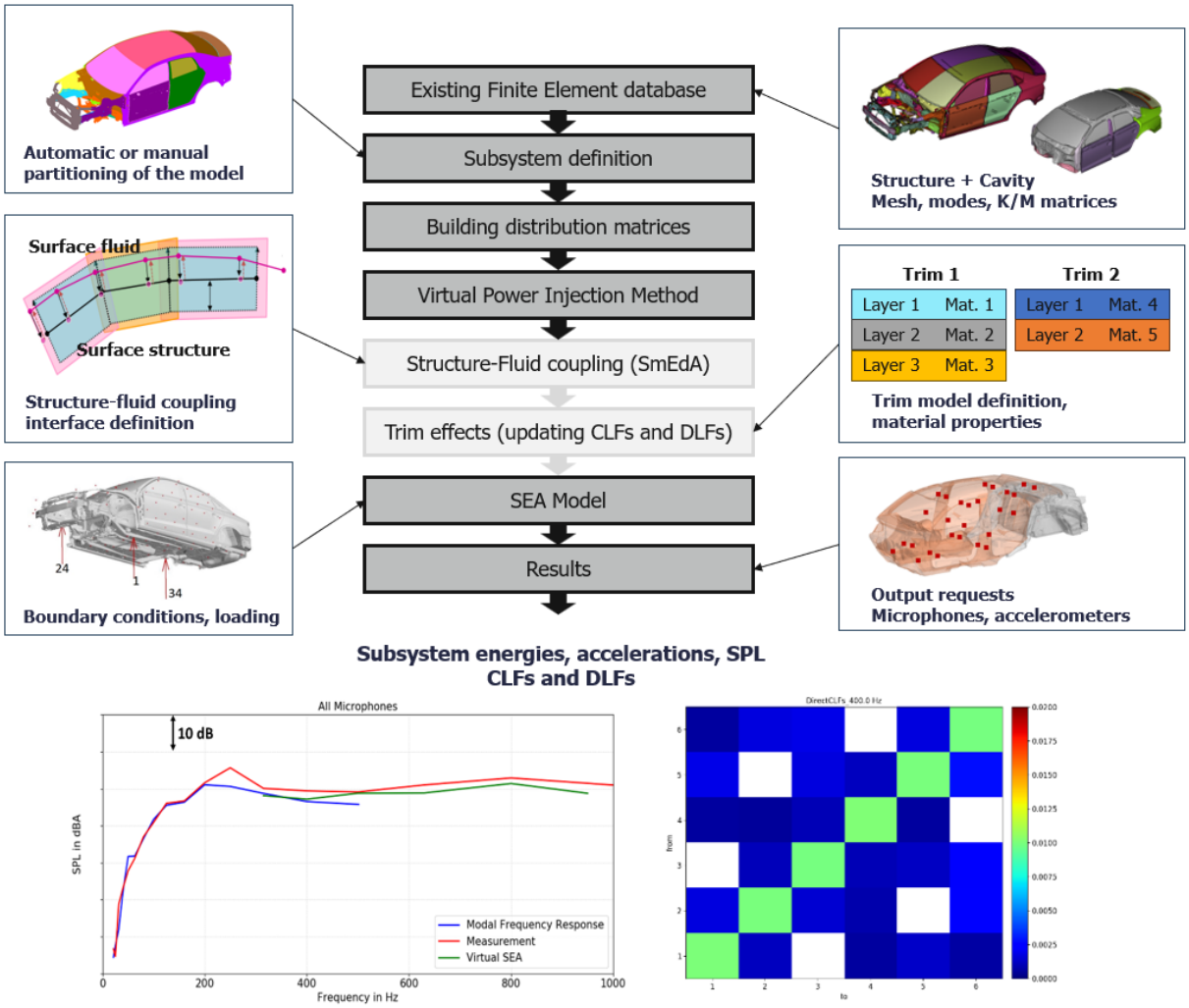

Figure 9. General workflow of a Virtual SEA simulation [81].

4.5. Clustering algorithms

The other most challenging part of the SEA simulation besides obtaining the loss matrix, [$\boldsymbol{\eta}$], is the creation of subsystems, which requires a lot of expertise in order to be in line with the assumptions. As seen, numerous previous works [62], [57], [58], [63], [65] employed clustering methods for SEA simulations. Since SEA subsystems are required to have homogenous vibrational energy distribution, it seems obvious that such techniques offer an effective solution for the subdivision of a mechanical system. Cluster analysis is a technique that allows grouping a large population of data so that the data in the same groups have similar properties. These groups of similar properties are called clusters. Several different classification models exist, considering different properties of the data points for clustering.

4.5.1. Agglomerative hierarchical clustering

One of the most popular methods is hierarchical clustering, which has two types: agglomerative and divisive [84]. These two methods work exactly in the opposite way, but the former one is

the most commonly used [65], [84]. Agglomerative hierarchical clustering builds a binary tree from the data points. Initially, all the data points are individual clusters. Then, in each iteration, the closest two clusters are merged, until only one cluster (or N) remains. The linkage function defines the calculation of the distance of any two subsets and groups objects into clusters based on their similarity. The linkage method can be chosen according to the characteristics of the exact dataset. The graphical representation of the so-obtained binary tree is called a dendrogram. A dendrogram shows the (dis)similarity of two clusters on the vertical axis. The cluster centroids can be extracted from the dendrogram by cutting it at a chosen height to obtain a flat clustering. For example, one can define the exact height by considering the largest difference (dissimilarity) between two iterations. [84].

4.5.2. K-means clustering

K-means [63], [85] is also a popular clustering technique because it is easy to understand and implement. It starts by initializing a randomly chosen K centroids and in the first iteration, every data point is assigned to the closest one, based on their squared Euclidian distances. Next, each of the so-obtained cluster's means are recalculated, thus defining the new centroids. The iteration continues until the centroids have stabilized or the maximum number of iterations is reached. In other words, the algorithm finds the lowest sum of squared Euclidian distances between every data point and their centroids. The most significant drawback of this method is that one has to know the exact number of clusters that will be formed [85].

4.5.3. X-means clustering

In order to overcome this issue of the K-means algorithm, Pelleg and More [86] proposed the X-means algorithm. This technique provides not only the centroids, but the value of K that scores the best by a model selection criterion. The lower and upper bounds of K still have to be provided by the user. X-means starts by running conventional K-means with K equal to the number of lower bound for the clusters. Then, new centroids are created by splitting some of the existing ones into two by certain strategies and continue with performing K-means until the upper bound of the possible number of clusters is reached. The best scoring model by the defined criteria during the iteration will be considered as the final result [86].

4.6. Design of Experiments

In scientific research and industrial applications, extracting the maximum amount of unbiased information about a system from the fewest number of (costly) observations and showing the statistical significance of a factor that exerts on a dependent variable is usually desirable. Design

of Experiments (DOE), first introduced by Fischer [87] is a systematic approach to explore the effects of varying input parameters on the output response of a system. A DOE utilizes statistical methods to get the maximum amount of information about a system while minimizing the number of experiments to perform. According to Ref. [88], design methods can be classified in two categories, random designs, and orthogonal designs. The first category includes designs where the input values of the parameters are determined by a random process. The most common random design method is the Latin Hypercube Design (LHD). LHD generates random design points while considering the previously generated ones. Its theory can be further extended by defining the spread of the design points in the design space, to avoid the undesired clustering of the design points.

The category of orthogonal designs includes designs like full factorial and central composite design. In a full factorial design, every level of every factor appears with every level of every factor, the effect of each factor is investigated simultaneously. This means, the total number of experiments to perform is given by Equation (43) where k is the number of the factors, n_i is the number of levels for the i^{th}factor [88]:

$$N = \prod_1^k n_i \tag{43}$$

Figure 10 shows an example of a three-factor, two-level full-factorial design. The main disadvantage of a two-level design is that only linear effects can be predicted. However, according to Equation (43), the total number of experiments increases exponentially with the number of factors. The base of the exponent corresponds to the number of levels. This means that the total number of experiments can take a substantial number, when it is desired to consider nonlinear effects.

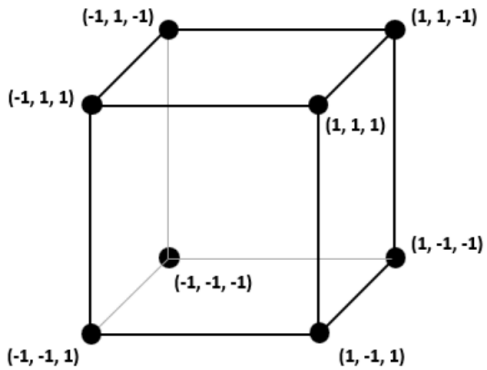

Figure 10. Two-level full factorial design for three factors.

To overcome this issue, central composite designs offer a possible solution that can predict nonlinear effects, while keeping the total number of experiments moderated. This can be achieved by taking a two-level full factorial design and adding the minimum number of points

to the design that provides at least levels for each factor, which allows the estimation of the curvatures. In a design with k factors, $2k + 1$ points will be added, called star points or axial points and a center point. Central composite design can be classified by the distance of the star point from the center, shown in Figure 11 [88].

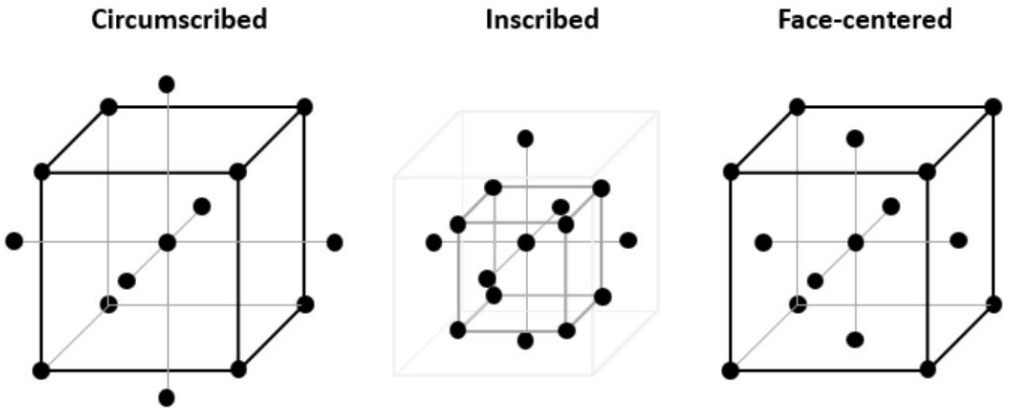

Figure 11. Circumscribed, inscribed and face-centered central composite designs.

In the circumscribed design, the star points are on the axes outside of the prescribed intervals and the center point is at the origin. The geometry of the design region is determined by a scale factor, designated as α. It describes the ratio of the distance of the star points and the factorial points from the center. To achieve a spherical (or hyper spherical) design, where the star points and the factorial points are located on the same sphere, α must be set to the square root of the number of the factors. This design provides 5 levels of each factor and provides high quality estimations over the whole design space but has points outside of the original ranges. In the inscribed design, the star points take the values of the strict limits, and the factorial points are in the interior of the design space. In this case, the position of the factorial point can be changed by dividing the radius of the star points with the scale factor, α. This design also provides 5 levels of each factor, but the quality of its predictions near the corners of the design space falls short of the circumscribed design. The face-centered design sets the star points and the factorial points to the value of the factor limits, in other words, $\alpha = 1$, which results only three levels for each factor and weaker prediction capabilities for quadratic responses than the former design types. On the other hand, the whole design space is more equally explored while respecting the limits of the factors [88].

4.6.1. Response Surface Modeling

Response Surface Modeling (RSM) is used to describe the relation between the input factors and the results and visualize the model predictions in the design space, without performing more experiments. Response surfaces are typically generated by the least squares fitting method

that minimizes the sum of the squares of the residuals of the result points from an analytical surface. Mathematically, a least squares fitting problem with n experiments, k independent variables $(x_1^i, \dots, x_k^i, y^i; i = 1, \dots, n)$ and m adjustable parameters $(\alpha_j; j = 1, \dots, m)$ with the functional relationship between the measured dependent and independent variables $y(x) = y(x; \alpha_1, \dots, \alpha_m), x = (x_1, \dots, x_k)^T \epsilon \Re^k)$ can be described as [88]:

$$min_{\alpha_1,\dots,\alpha_m} \sum_{i=1}^{n} \left[y^i - y(x^i; \alpha_1, \dots, \alpha_m)\right]^2 \tag{44}$$

where $x^i = (x_1^i, \dots, x_k^i)^T$. The described relation of dependent and independent variables is a general form of the model equation, containing linear and nonlinear relation between the parameters. In Taylor method for least squares model, any combination of the Taylor polynomial terms can be selected as a basis function to find an optimal fitting. For example, a quadratic Taylor polynomial basis function with two factors [88]:

$$y = \alpha_1 + \alpha_2 x_1 + \alpha_3 x_2 + \alpha_4 x_1 x_2 + \alpha_5 x_1^2 + \alpha_6 x_2^2 \tag{45}$$

For linear least squares model, Equation (46) has to be solved as [88]:

$$min_{\alpha_1,\dots,\alpha_m} \sum_{i=1}^{n} \left[y^i - \sum_{j=1}^{m} \alpha_j X_j(x^i)\right]^2 \tag{46}$$

where $X_1(x), \dots, X_m(x)$ are the arbitrary fixed functions of $x = (x_1, \dots, x_m)^T \epsilon \Re^k$. Let **A** an $n \times m$ component matrix and $\boldsymbol{b}$ vector with the length of n defined by Equations (47) and (48) [88].

$$\mathbf{A} \equiv \left[\alpha_{ij}\right] = X_j(x^i) \tag{47}$$

$$b_i = y^i, b = (y^1, \dots, y^n)^T \tag{48}$$

Here, **A** is called the matrix of the fitting problem. The vector of the parameters to be fitted is defined by [88]:

$$\alpha_j = (\alpha_1, \dots, \alpha_m)^T \tag{49}$$

If $\alpha^* = (\alpha_1^*, \dots, \alpha_m^*)^T$ is the minimizer of the equation of the least squares fitting problem, derived from Equation (46), the final equation will be [88]:

$$\sum_{j=1}^{m} q_{kj} \alpha_j^* = \beta_k \tag{50}$$

where:

$$q_{kj} = \sum_{j=1}^{m} X_j(x^i) X_k(x^i) \text{ and } \beta_k = \sum_{j=1}^{m} y^i X_k(x^i) \tag{51}$$

Equivalently,

$$\mathbf{Q} \cdot \boldsymbol{\alpha}^* = \boldsymbol{\beta} \tag{52}$$

where:

$$\mathbf{Q} = \left[q_{kj}\right]_{i,j=1,\dots,m} = \mathbf{A^T} \cdot \mathbf{A} \, \epsilon \, \Re^{m \times m} \text{ and } \boldsymbol{\beta} = \mathbf{A^T} \cdot \mathbf{b} \tag{53}$$

This is called the equations of the least squares problem that can be solved by standard methods [88].

4.6.2. Error measures and regression parameters

The quality of the fitted response surface model can be described by several types of error measures and regression parameters that provide information about how the response surface follows the simulation outputs in the design points. Let n the number of experiments, m the number of terms that are used for the response surface calculation, y_i the output of the i^{th} experiment and y_i^{pred} the predicted value if the i^{th} experiment by the response surface model. The mean output value is then given by [88]:

$$\bar{y} = \frac{\sum_{i=1}^{n} y_i}{n} \tag{54}$$

The sum of the squared differences between the experiments and the overall mean is [88]:

$$SSTOT = \sum_{i=1}^{n} (y_i - \bar{y})^2 \tag{55}$$

$SSTOT$ provide information only about the design method, but not the quality of the response surface model. The sum of squared error is [88]:

$$SSE = \sum_{i=1}^{n} (y_i - y_i^{pred})^2 \tag{56}$$

where y_i^{pred} is the predicted value by the response surface model. The average of the squared error is given by [88]:

$$MSE = \frac{SSE}{n-m} \tag{57}$$

SSE and MSE provide information about the quality of the response surface model too. Using these measures, the normal regression parameter is defined as [88]:

$$R^2 = 1 - \frac{SSE}{SSTOT} \tag{58}$$

If the normal regression parameter value is close to 1, it means that the quality of the model is good and the predicted values by the response surface model are close to the actual calculated ones. The adjusted regression parameter, given by Equation (59), considers the total number of experiments and the number of terms. Thus, it gives a smaller number than the normal regression parameter [88]:

$$R_{adj}^2 = 1 - (1 - R^2) \frac{(n-1)}{(n-m-1)} \tag{59}$$

The predicted residual sum of squares indicates the predictive capabilities of the model. It is calculated with the same formula as R^2, given by Equation (58), but only for $n - 1$ experiments, y_n is left out from the model. Next, it is evaluated how well the model predicts the result of the

left-out experiment. As iterating over the experiments, the results are summated in R^2_{press}. The schematic representation of the procedure is shown in Figure 12 [88].

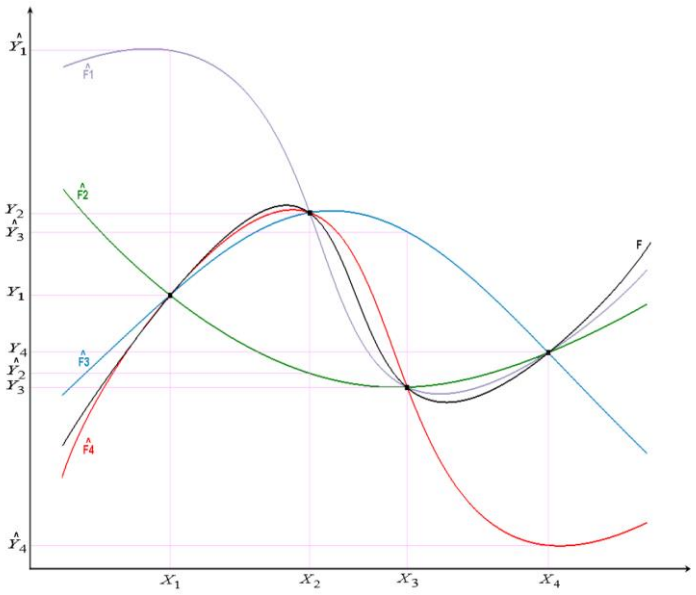

Figure 12. The calculation procedure of R^2_{press} parameter [88].

5. COUPLING LOSS FACTOR ESTIMATION FOR JUNCTION TYPES

As the overview of the SEA method pointed out, it is challenging to obtain the coefficients of the power balance equations, while the detailed modeling of the structure is not possible in SEA. Analytical formulas are only available for a set of connection types and performing a PIM on a prototype is not always feasible. Virtual SEA offers a solution for detailed modeling of different junctions through finite elements, thus considering dissipative and coupling strength effects in the simulation. Several studies in the literature cover the topic of analytical and experimental determination of CLFs and DLFs, but none of them provide validation for various finite element connections in Virtual SEA. The goal of this Chapter is to evaluate experimental and virtual PIM results for the most common junction types that can be found in a vehicle structure. Usually, these junctions consist of variously connected sheet metals and the most common joining methods are the line welding, spotwelding and gluing, as shown in Figure 2. The sensitivity of the finite element modelling parameters of the spotwelded joining method is also explored and investigated through a DOE. The validation is conducted by comparing experimentally measured and calculated coupling loss factors and by comparing the energy responses given to the same injected power. The experimental data was provided by former measurements, described in Treszkai et al. [56]. As mentioned before, the virtual PIM was performed in MSC Actran's Virtual SEA module, for which, the finite element modal calculation and the extraction of matrices was performed in MSC Nastran.

5.1. Test cases and simulation models for loss matrix estimation

Some of the most common connection types were investigated, based on the work of Treszkai et al. [56]. The least complex test cases were assembled and used for the validation, consisting of two coupled plates. The first reference model was a single piece of sheet metal bent 90° with 2 mm nominal thickness. The junction created by the bending splits the structure into 2 subsystems. Plate 1 will be excited along all the load cases and will be referenced as subsystem 1, while Plate 2 will be the receiver subsystem. The dimensions of the plates are approximately 650 × 550 mm, but due to the connections to be realized, there is a 20 mm overlap area between the coupled plates. This overlap for the connection was always formed from Plate 1 and bent in 90°, as described in Ref. [56]. The finite element model of the bent variant is shown in Figure 13.

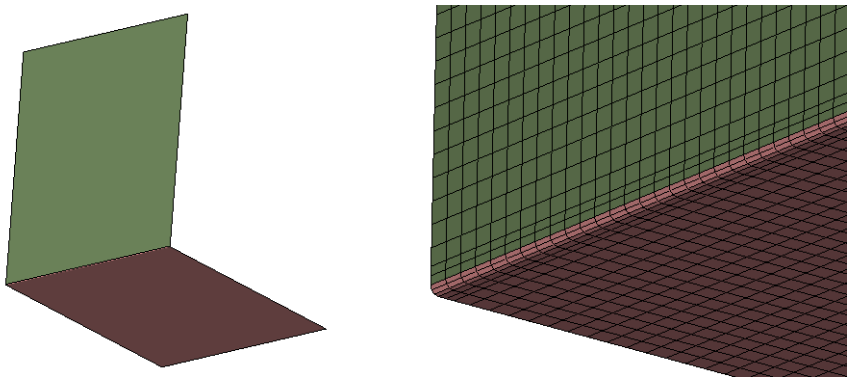

Figure 13. Finite element model of Test Case 1: the baseline bent variant.

In the second variant, the two plates were connected with line welding as shown by the representative finite element model in Figure 14. The elements used for realizing the connections are MSC Nastran-specific, and their specifications can be found in the corresponding documentation [76]. The line welding was modeled as RBE3-HEXA-RBE3 connection with one row and one layer of HEXA elements. The material properties of the solid elements were the same as for the plates. The line welding connection was created around the overlapping area just as on the physical model.

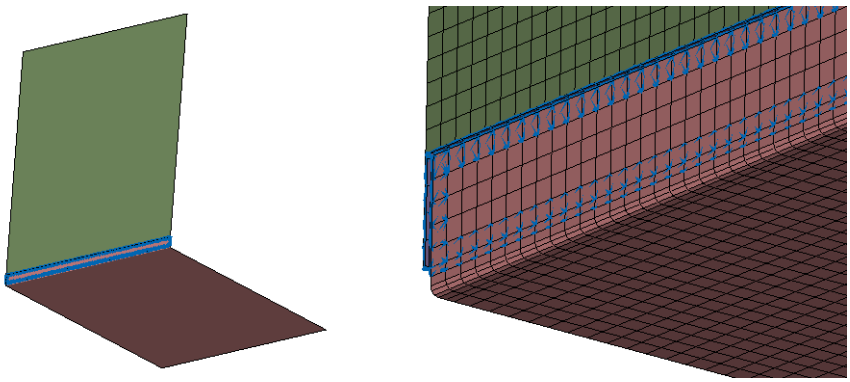

Figure 14. Finite element model of Test Case 2: the line welded variant.

In the third variant, a superglued type of connection was created. The whole overlapping areas on both plates were connected, again with RBE3-HEXA-RBE3 elements shown in Figure 15. The whole overlapping area between the plates was filled with 3 layers of HEXA elements and those material properties were set according to Table 2.

Table 2. Material properties of superglue.

Young's modulus	1 630 MPa
Poisson ratio	0.45
Density	1 200 kg/m^3

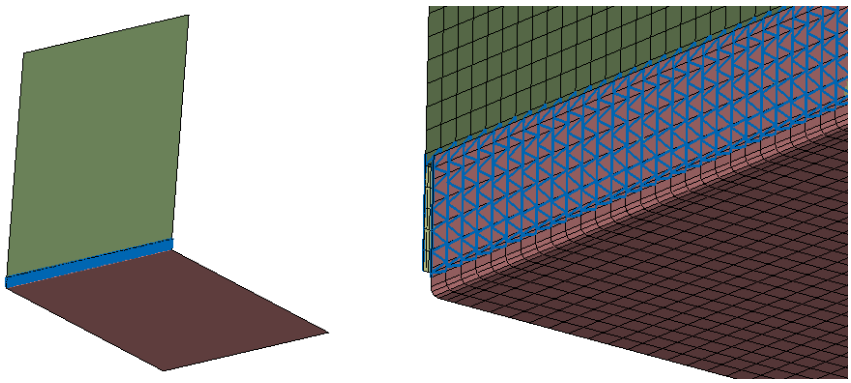

Figure 15. Finite element model of Test Case 3: the superglued variant.

The last connection that was investigated is a spotwelded variant. Five connection points were equally spaced in the overlapping area, as shown in Figure 16. The finite element representation of this type of connection is again RBE3-HEXA-RBE3. This time, a single HEXA element was created in the connection and similarly to the line welded variant, the material properties of the solid elements were set to steel.

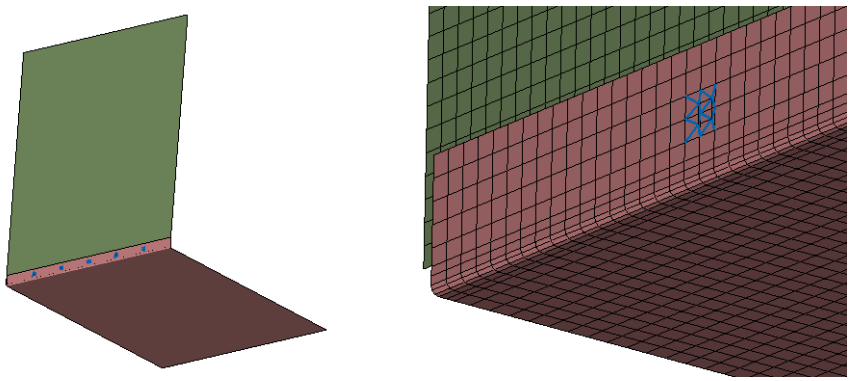

Figure 16. Finite element model of Test Case 4: the spotwelded variant.

The measurement process that provided the data for this comparison is described more in detail in Ref. [56]. In short, impact testing methodology was employed with a total of 12 accelerometers per plate (4 at once to minimize their mass effect), based on the findings of Ref. [VII]. 4 excitations were defined randomly on Plate 1 and the injected power was measured according to Equation (27). The response of Plate 2 was calculated according to Equation (28) and averaged over the 4 excitation load cases. The measurement frequency range was 178 Hz – 1778 Hz with 0.07 Hz resolution. Free-free boundary condition was during the measurements by hanging the structure on bungee cords. Regarding the finite element simulation models, it is required to have 8-10 linear elements per bending wavelength at the highest frequency of the analysis. In this case, for a steel plate with 2 mm thickness, the bending wavelength is approximately 100 mm at 2000 Hz, meaning that the maximum element size should be less

than 10-12 mm. Based on this, the 5 mm mesh that was used in the models can be considered valid at 2000 Hz, which was the upper bound of the modal base calculation. The SEA subsystem division was also kept the same during the analyses. The finite elements created for the connections were always assigned to the receiver plate's subsystem. For each variant, two Virtual SEA simulations were built up. One with constant global damping, assuming that no measurements had been made in prior simulations and one where the damping values of the plates are exactly the same as the measured DLF values. The constant damping value in the second case was set to 0.2%, which is a typical value for such lightly damped steel plates, and it approximates the real measured damping value best over the frequency range of interest. Both Virtual SEA variants were excited with the exact same injected power that comes from the measurements to make the results as comparable as possible.

The results will be analyzed in terms of the energy levels of the receiver subsystem, i.e., Plate 2. Measured curves will be compared to simulation results, one with constant DLFs and one with measured DLFs. The determination of the DLF values is described in detail in Ref. [VI]. The second type of comparison for each variant investigates the CLFs. In this case, since the damping and coupling loss factors are dependent on each other, the measured CLF curves will only be compared to the simulation where the measured DLFs were applied. Thereby, no external factors affect the result, so one can get a more accurate insight to the differences of the measured and the calculated CLFs by the Virtual SEA approach. It should be noted that the measured CLFs are quite challenging to capture accurately. Moreover, if the SEA weak coupling condition is assured, large discrepancies can occur in the CLFs whose effects may not appear in the energetic results of the receiver plate.

5.2. Results and analyses of Test Case 1: bent variant

Figure 17 shows the energy response of the receiver plate in measurement and Virtual SEA simulations. It can be observed that the 0.2% constant damping value employed in the simulation (blue curve) still might be too high, proven by the measured values that were lower in general as well. The simulation employing the exact damping values (green curve) agrees very well with the measurement. The general trend of both the results is still acceptable and both curves reflect the real behavior of the structure.

The comparison of the measured and calculated coupling loss factors is shown in Figure 18. It can be observed that in the measurement and in the simulation too, the reciprocity relation is respected. In the low frequency range, larger discrepancies can occur but as the frequency increases, the results get more accurate. Starting from about 300 Hz, the trends are relatively

well captured, except in the 1 000 Hz third octave band. This effect is slightly visible in the energy response curves as well. Overall, the bent model has few parameters to tune, thus this level of correlation is expected. The discrepancies can be attributable to the high sensitivity of the model.

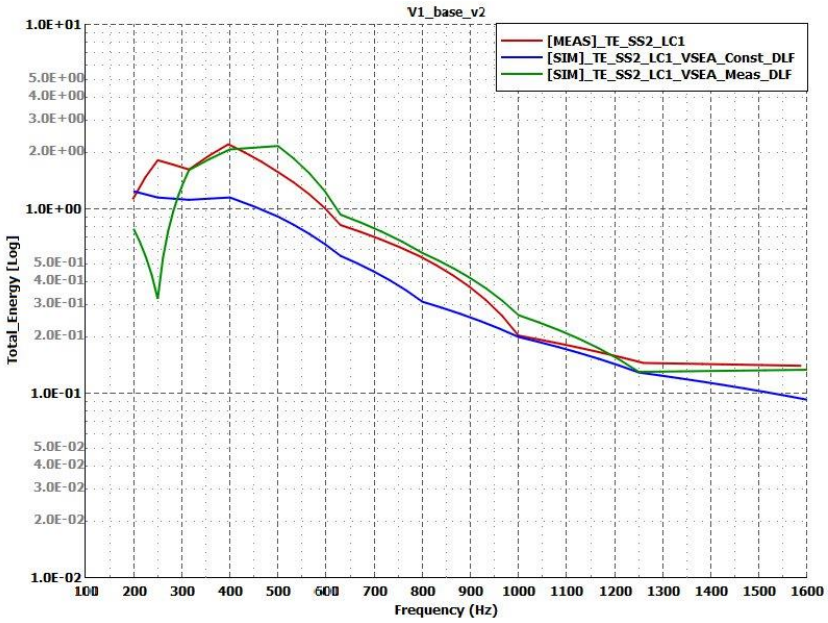

Figure 17. Energy response of the receiver plate for Test Case 1: baseline bent variant. Measurement – red curve; simulation with constant damping – blue curve; simulation with measured damping – green curve.

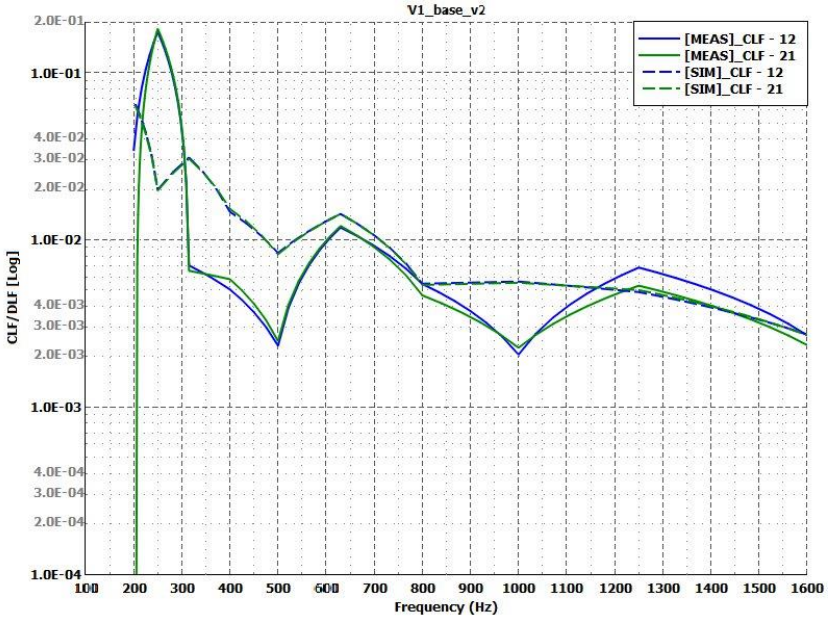

Figure 18. Coupling Loss Factors for Test Case 1: baseline bent variant. Measurement – solid lines; simulation – dashed lines.

5.3. Results and analyses of Test Case 2: line welded variant

The energy response of Plate 2 in the line welded variant is shown in Figure 19. This time both simulation curves are in good agreement with the measurement. The 0.2% constant damping value for this variant seems to be appropriate (blue curve). The simulation with the measured damping value (green curve) has discrepancies in certain third octave bands in the low frequency range and in the 500 Hz band. These bands have the largest difference in terms of coupling loss factors too, as shown in Figure 20. Despite this, the rest of the results in this frequency range agree with the measurement and overall, for such sensitive structure, thus the modelling method for line welding can be approved.

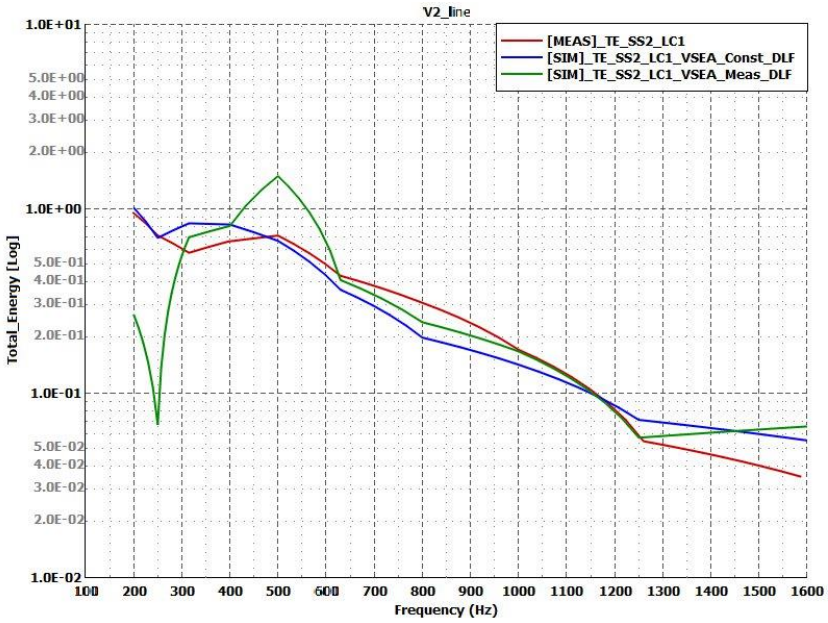

Figure 19. Energy response of the receiver plate for Test Case 2: line welded variant. Measurement – red curve; simulation with constant damping – blue curve; simulation with measured damping – green curve.

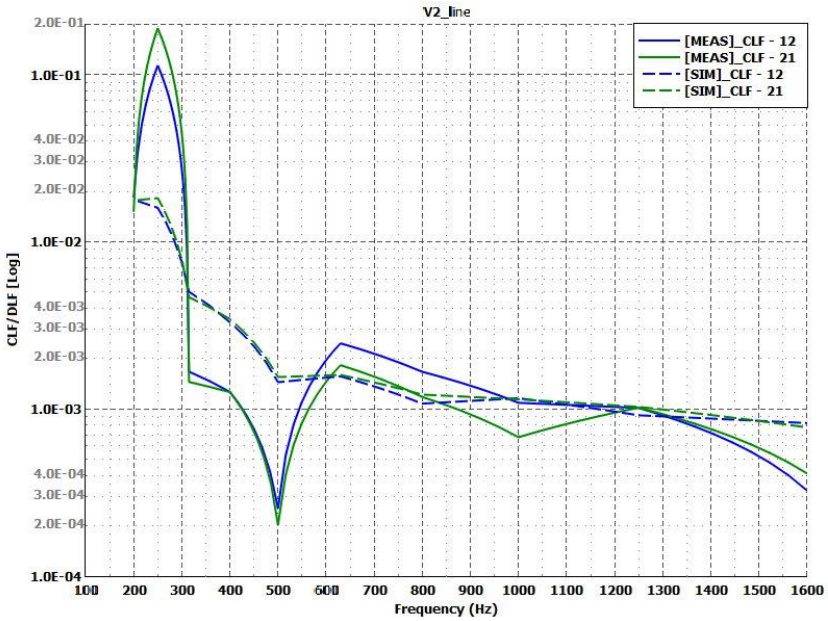

Figure 20. Coupling Loss Factors for Test Case 2: line welded variant. Measurement – solid lines; simulation – dashed lines.

5.4. Results and analyses of Test Case 3: superglued variant

The next variant to compare the results of is the superglued junction type. Figure 21 shows, with the approximated constant damping (blue curve), the simulation model is slightly overdamped below 600 Hz but above this frequency, it gives reliable results. The simulation model with the measured damping (green curve) almost perfectly catches the measurement curve in every third octave frequency band. Figure 22 shows the comparison of the measured and calculated CLFs. It can be observed that the nature of these curves is well represented by the Virtual SEA simulation from 400 Hz, though the amplitudes are not necessarily correct. However, this does not have a significant impact on the energy response curves, as can be seen in Figure 21.

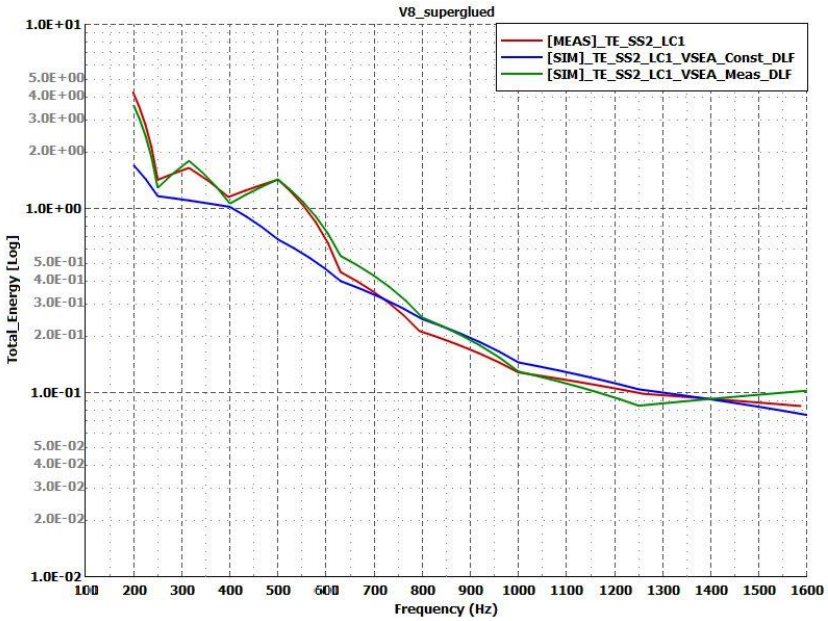

Figure 21. Energy response of the receiver plate for Test Case 3: superglued variant. Measurement – red curve; simulation with constant damping – blue curve; simulation with measured damping – green curve.

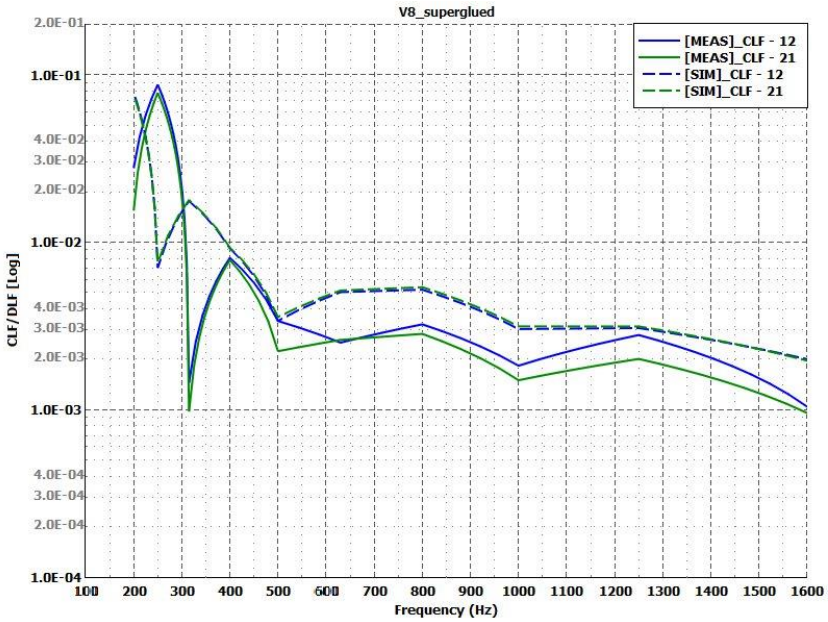

Figure 22. Coupling Loss Factors for Test Case 3: superglued variant. Measurement – solid lines; simulation – dashed lines.

5.5. Results and analyses of Test Case 4: spotwelded variant

Last, the results of the spotwelded variants are compared in Figure 23 and Figure 24. The former shows that the energy response of the receiver plate has the largest difference between simulation and measurement among all of the variants. The simulation with the measured damping values (green curve) shows similarities with the experimental results in terms of

trends, but the correlation of the results is much worse than expected. The constant damping value for this variant does not provide reliable results. Regarding the measured and calculated coupling loss factors shown in Figure 24, it is obvious that something is wrong with either the simulation model or with modelling method of the spotwelded connection. To find out what could cause such differences and what are the main influencing factors of the connection modeling, a DOE was performed, and response surfaces were created to visualize the results.

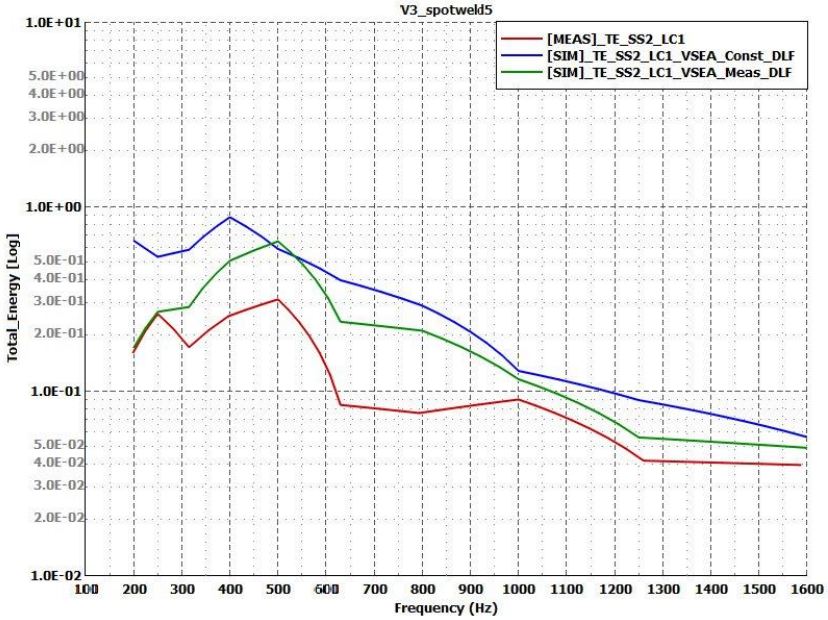

Figure 23. Energy response of the receiver plate for Test Case 4: spotwelded variant. Measurement – red curve; simulation with constant damping – blue curve; simulation with measured damping – green curve.

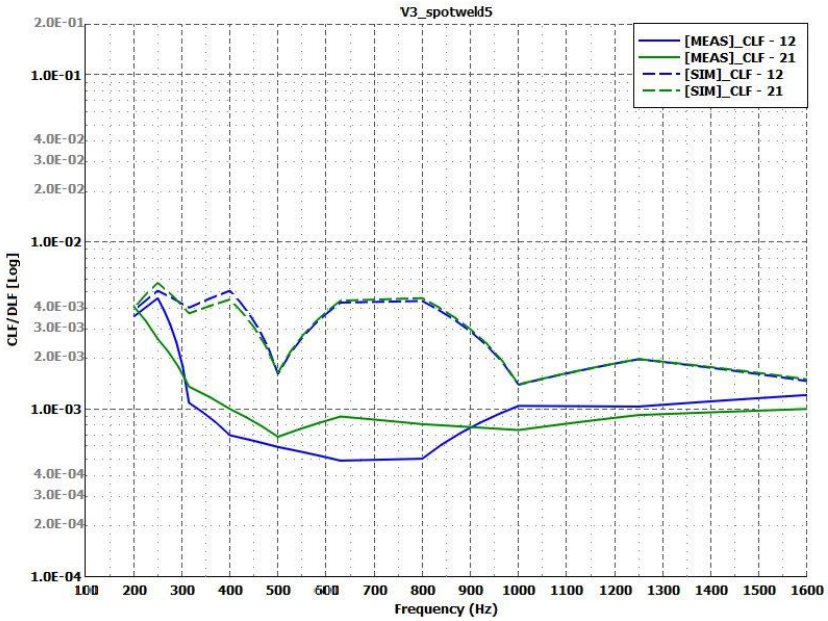

Figure 24. Coupling Loss Factors for Test Case 4: spotwelded variant. Measurement – solid lines; simulation – dashed lines.

5.5.1. Design of Experiments in coupling modeling

The dynamic behavior of the connection can be traced back to its stiffness, to the size of the area involved in the coupling and to the geometrical properties of the connecting region. The stiffness of the connection can be influenced by the material properties of the connecting HEXA elements. Typically, these are defined as the same material as the connecting structure, but different connection stiffnesses can be introduced through the changes of the Young's modulus of the connecting HEXA elements. The size of the involved area corresponds to the arrangement of the finite element grids coupled by the RBE3 elements. The effect of the coupling area can be investigated by gradually increasing the coupling RBE3 diameters. The geometrical properties of the connecting region include parameters that most of the analytical formulas are based on, e.g., the dimensions of the connecting structure, thickness ratio, or the distribution of the coupling points. The plate dimensions and the distribution of the coupling points are given by the geometry, however uncertainties in the plate thicknesses can occur and their relative extent can be significant. Based on the above, the parameters that were selected for the DOE and their investigation ranges are summarized in Table 3. The effect of the damping – whether it is constant or measured – could already be seen previously, so it was left constant not to bias the effect of the other parameters.

Table 3. DOE parameters and ranges.

Parameter name	Min. value	Nominal	Max. value
HEXA Young's modulus	100 000 MPa	210 000 MPa	300 000 MPa
RBE3 diameter	5 mm	10 mm	20 mm
Receiver plate's thickness	1.9 mm	2 mm	2.1 mm

Selecting the appropriate design method is crucial to get the maximum information from the least experiment. In this case, nonlinear responses are expected so at least 3 levels of each factor is necessary to have. In order to save computational time, a central composite design was preferred over a 3-level full factorial design. Of the three possible types of such design, only the face centered type can be considered, since the RBE3 diameter has strict ranges, i.e., the RBE3 elements can only couple predefined nodes at discrete distances. This results in a total of 15 experiments. The area covered by the energy response of the receiver plate for all runs is shown in Figure 25, which suggests that significant deviations can occur in the results, especially in the low and mid-frequency range. In this frequency range, the large deviation is caused by the shifting of the global modes due to the variation of model parameters. Starting from 1 000 Hz, the model better satisfies the SEA assumptions and behaves like a statistical system so that the uncertainties like thickness and connection stiffness variations will have less pronounced effect on the frequency and spatially averaged response, proving the applicability of classical SEA. The same phenomenon is illustrated in Figure 3.

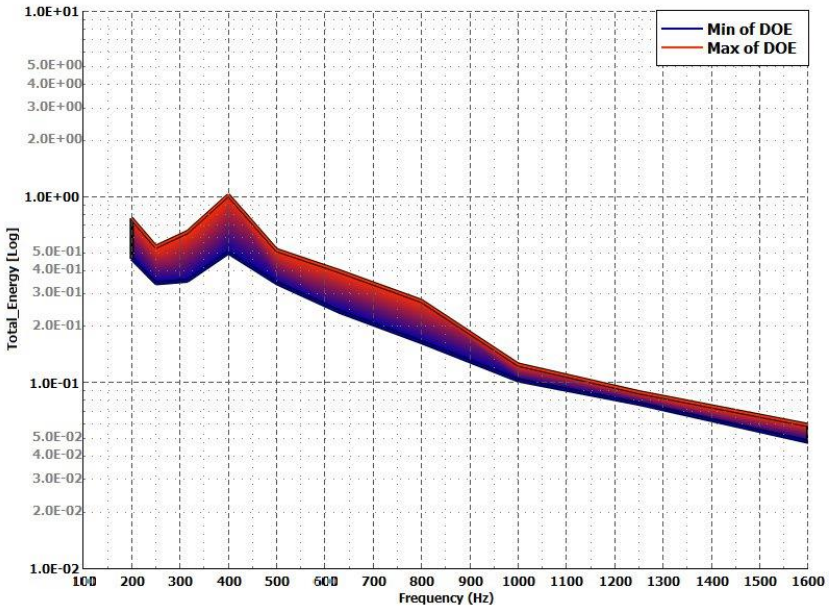

Figure 25. Area covered by the energy response curves of the receiver plate, spotwelded variant in the DOE.

To better visualize the results and to investigate the individual effects and the interaction of the parameters, response surfaces were created for each frequency band with the least squares fitting method. The quality of the obtained response surfaces is evaluated by the error measures and regression parameters, described in Chapter 4.6.2. The averaged quality indicator values over all frequency bands are summarized in Table 4, which supports the reliability of the fitted model. Figure 26 shows the results at 200 Hz, as a function of two of the input parameters at a time, in every combination, while the parameter not shown on the axes is set to its nominal value. The Z axis value corresponds to the energy response of the receiver plate due to the same, measured injected power.

Table 4. Error measures and regression parameters for the fitted model.

Parameter name	Averaged value
SSE	1.28E-02
SSTOT	1.64E-01
R^2	8.87E-01
R^2_{ADJ}	8.28E-01
R^2_{PRESS}	8.40E-01
MSE	2.56E-03

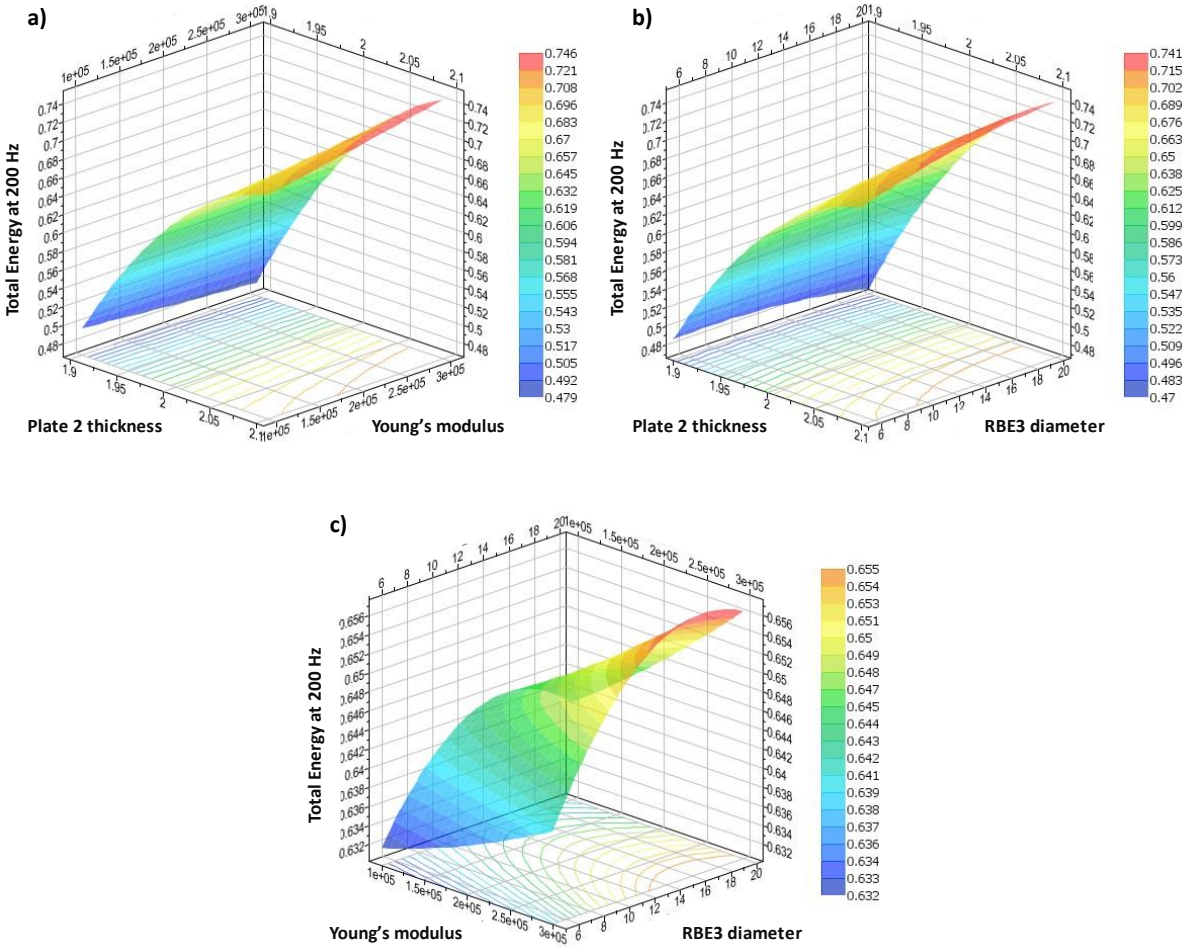

Figure 26. Response surfaces created for the energy response of the receiver plate at 200 Hz, Test Case 4: spotwelded variant.

It can be observed in Figure 26 a) and b) that the variations in the plate thickness ratio have greater impact on the results than the coupling element stiffness and coupling diameter. Along the axes of the latter two, the changes in the results are neglectable, except in one corner of the design space, approaching their minima and the maxima of the receiver plate's thickness value. Figure 26 c) shows that their interaction results in a small-scale, nonlinear behavior. With the increase of the frequency, the response surfaces gradually transition to the form of the 400 Hz band results, shown in Figure 27. The influence of the coupling element stiffness and the coupling diameter is dominated by the effect of the variations in the plate thickness ratio, showing strong nonlinear behavior in this frequency band. At the bounds of the design space, the expected response is significantly lower than at the nominal value, where the plate thicknesses are equal. The other parameters have minor effects in this frequency band where the plate thickness is above the nominal value. Figure 27 c) shows that the interaction of these shows a smaller degree of nonlinearity.

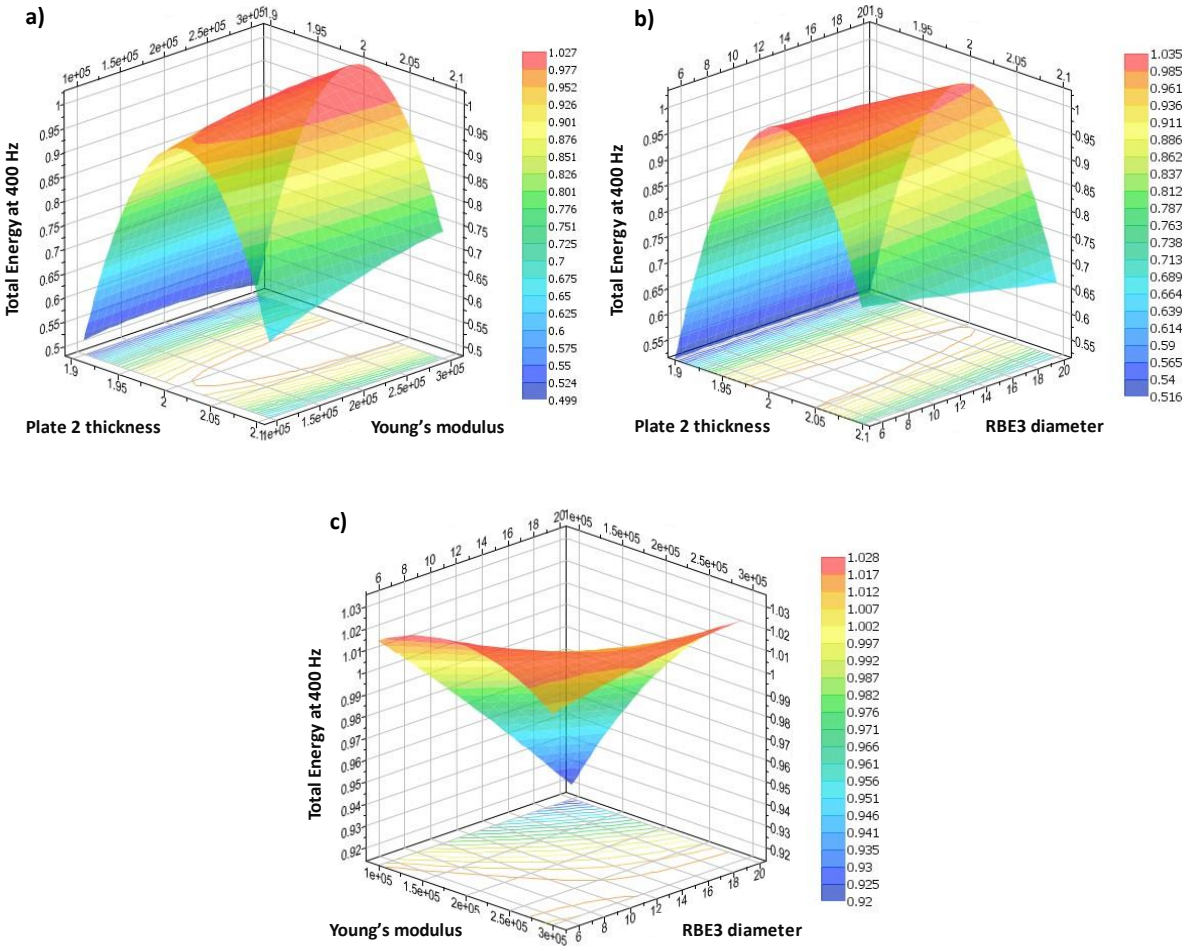

Figure 27. Response surfaces created for the energy response of the receiver plate at 400 Hz, Test Case 4: spotwelded variant.

However, in the 500 Hz frequency band, the influence of the coupling element stiffness and coupling diameter becomes more pronounced, as shown in Figure 28. Strong nonlinear effects appear in their behavior, comparable to the significance of the variations in the plate thickness ratio. The effect of the coupling element stiffness is similar in nature to the thickness ratio variation, both have maxima at their nominal values and minima at the bounds of their ranges. On the other hand, the opposite effect can be observed in the coupling diameter, it minimizes the response surface at its nominal value. This behavior is represented by a paraboloid and a hyperbolic surface respectively.

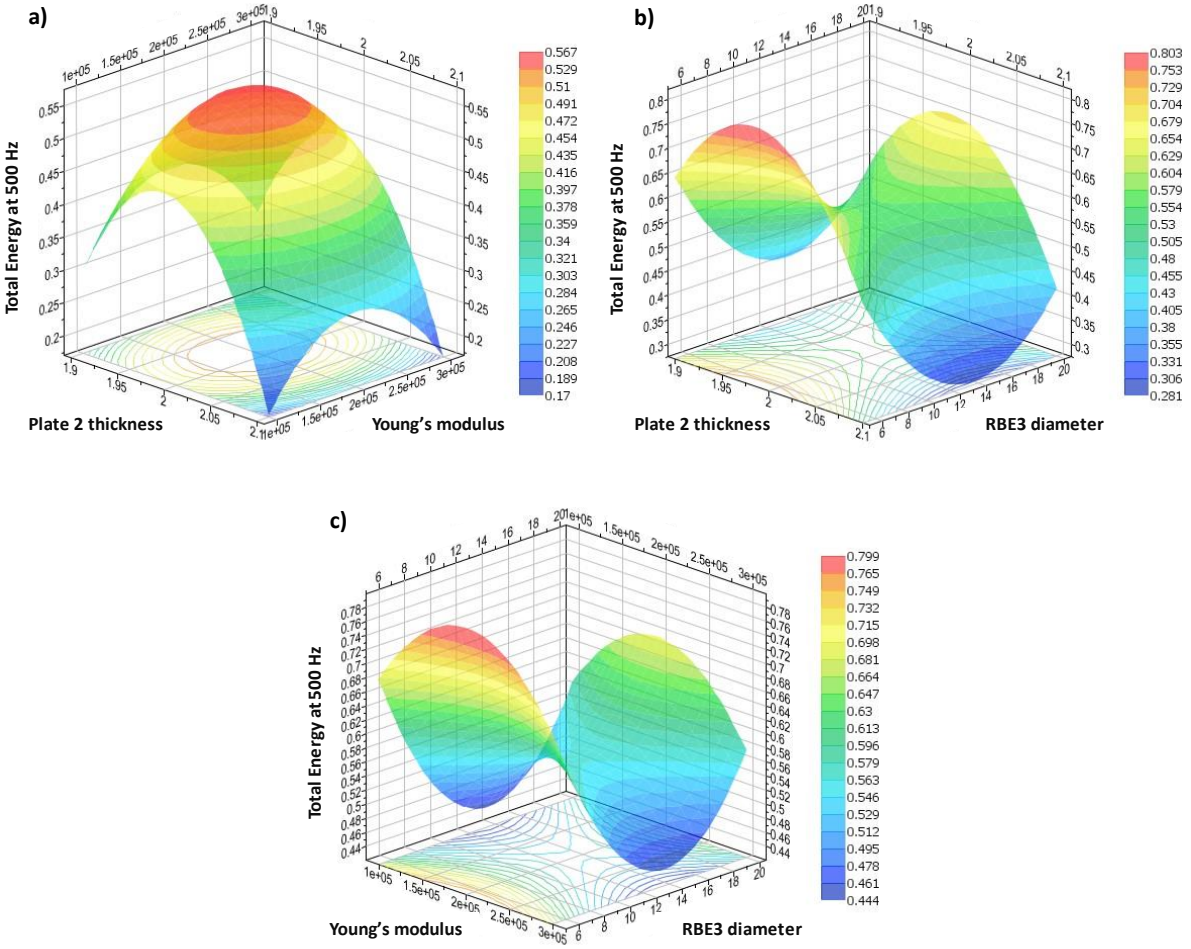

Figure 28. Response surfaces created for the energy response of the receiver plate at 500 Hz, Test Case 4: spotwelded variant.

At higher frequencies, up until 1 000 Hz, the response surfaces show similar shapes as in the 400 Hz band. The most dominant factor is still the thickness ratio of the plates, showing strong nonlinear behavior. From 1 000 Hz onwards, all of the effects prevail to a lesser extent. as could be seen in Figure 25. The 1 600 Hz band results in Figure 29 show that the effect of the thickness ratio variation becomes less and less dominant, while the relative influence of the others increases and shows similar behavior as seen in the 500 Hz frequency band in Figure 28. The overall conclusion of the DOE is that the most influential factor of the connection representation in Virtual SEA is the thickness ratio of the connecting plates. The coupling element stiffness and coupling diameter have only minor effects on the results in the majority of the frequency range.

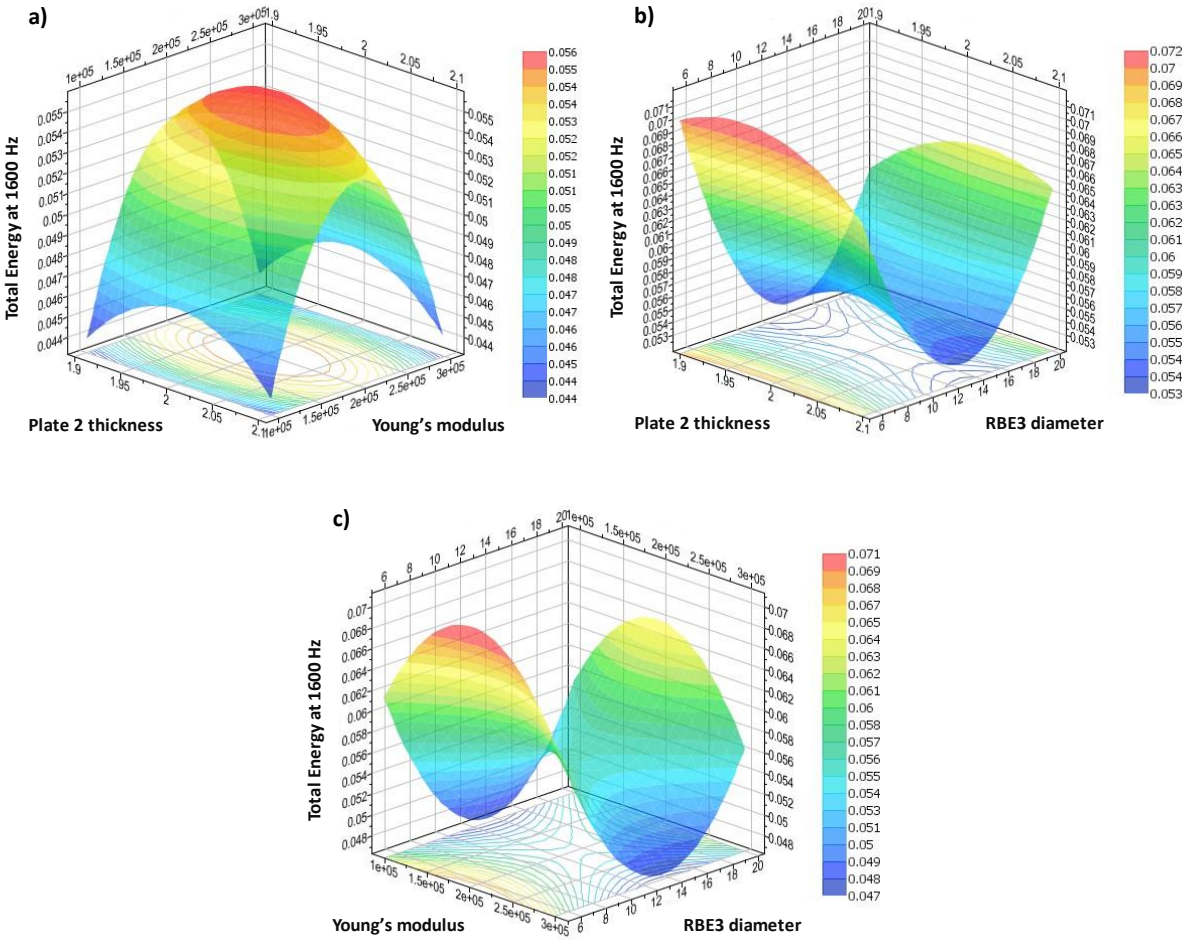

Figure 29. Response surfaces created for the energy response of the receiver plate at 1 600 Hz, Test Case 4: spotwelded variant.

5.5.2. Validation of Test Case 4: spotwelded variant results

To evaluate the predictive quality of the DOE, further points were selected from the design space and their results were compared to measurement. In the first case, the Young's modulus of the HEXA elements in the connection was set to the minimum value, 100 000 MPa, while the other parameters were at nominal values. According to Figure 28 a), the energy response of the receiver plate is expected to decrease in the 500 Hz frequency band in this case. Figure 30 shows the comparison of the two simulations with measured and constant damping compared to measurement. In the 500 Hz band, when compared to Figure 23, the total energy of Plate 2 is decreased by a value of 0.1 in both simulations, as expected. Accordingly, small changes in the calculated CLFs can also be observed in Figure 31, which suggests that the spotwelded model still cannot be regarded valid.

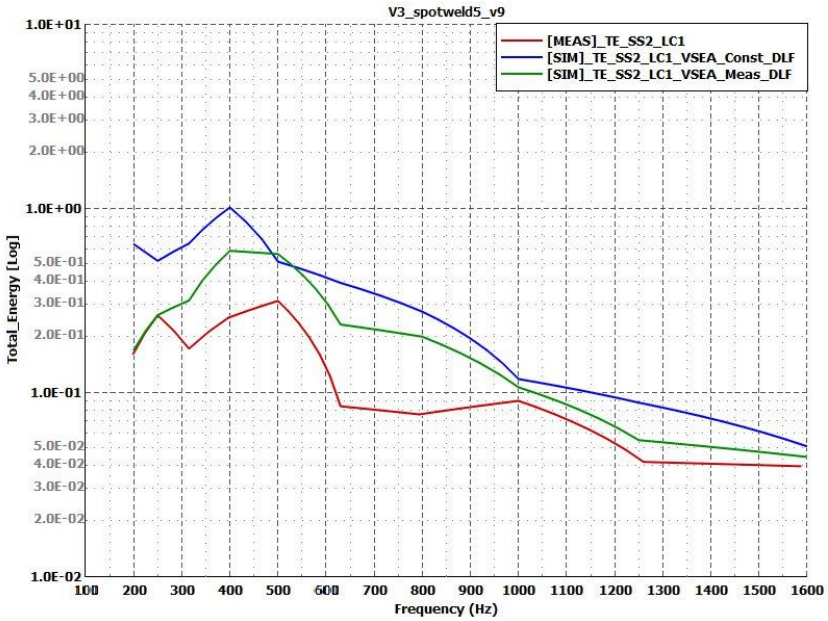

Figure 30. Energy response of the receiver plate for Test Case 4: spotwelded variant with decreased connection element stiffness. Measurement – red curve; simulation with constant damping – blue curve; simulation with measured damping – green curve.

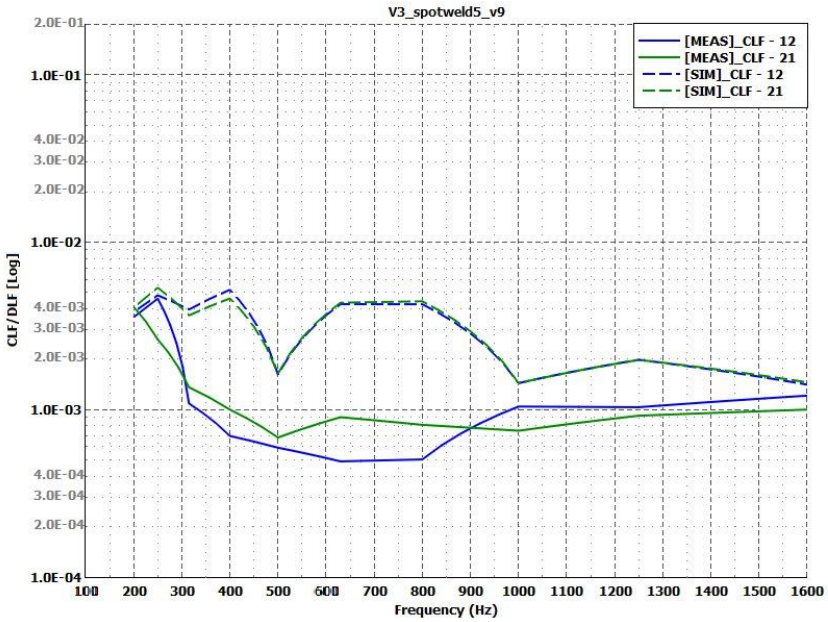

Figure 31. Coupling Loss Factors for Test Case 4: spotwelded variant with decreased connection element stiffness. Measurement – solid lines; simulation – dashed lines.

In the next simulation model, the connection stiffness and the thickness of the receiver plate were left on nominal values, and the RBE3 diameter was set to 15 mm. The design point corresponding to this value was not included in the DOE. According to the response surfaces in Figure 26-Figure 29, this change in the simulation model should not affect the results significantly compared to Figure 23. Not even in the 500 Hz frequency band, since points

corresponding to the nominal 10 mm value and to the 15 mm diameter lie approximately at the same contour line – points with equal values on the response surface. Figure 31-Figure 32 support the expectations, showing the energy response on the receiver plate and the calculated CLFs, respectively.

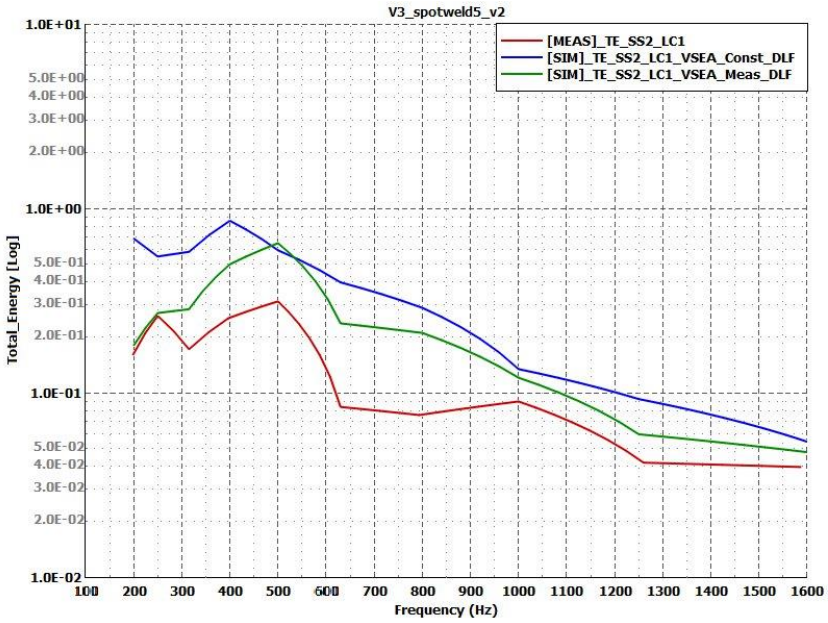

Figure 32. Energy response of the receiver plate for Test Case 4: spotwelded variant with increased connection area. Measurement – red curve; simulation with constant damping – blue curve; simulation with measured damping – green curve.

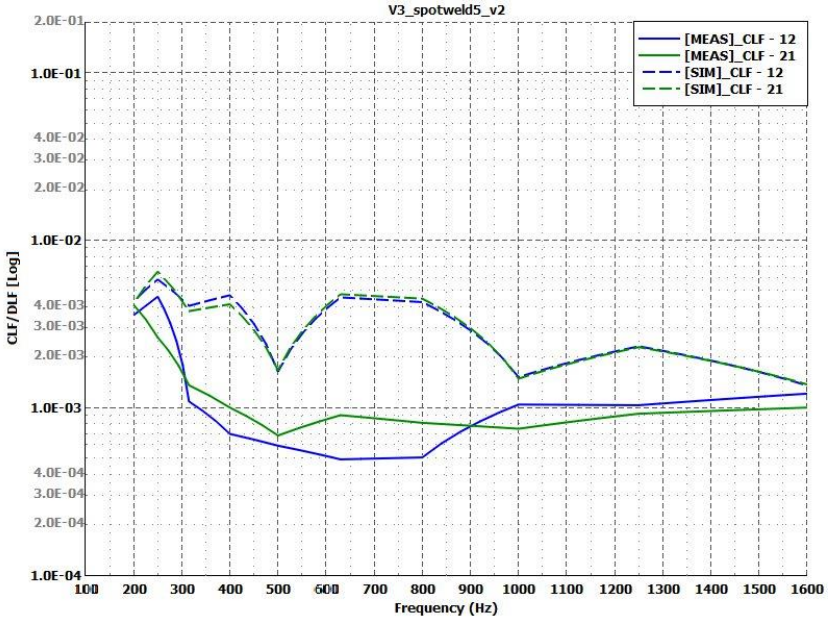

Figure 33. Coupling Loss Factors for Test Case 4: spotwelded variant with increased connection area. Measurement – solid lines; simulation – dashed lines.

In the next step, the thickness ratio of the plates was changed, and the other parameters were set to nominal values. As seen in Figure 23, the calculated responses were much higher than the measured curve. According to the upper images of the response surfaces in Figure 26-Figure 29, the greatest effect can be achieved in the low and mid-frequency range by changing the thickness ratio in such a way, that the receiver plate is thinner than the excited one. Control measurements on the prototype revealed that the actual thickness of Plate 1 is approximately 2.1 mm due to inaccuracies in manufacturing, so the model was modified accordingly. Figure 34 shows that this improved the energy response on the receiver plate significantly, especially when measured damping was applied, compared to the previously seen changes. The constant damping simulation curve is also improved, and its trend seems to be better fitting the experiment and the simulation with the exact damping values. As the green curve suggests, the model itself became much more accurate, but requires the precise determination of the damping curve. Figure 35 shows that significant improvement was achieved in terms of the coupling loss factors too. The trend of these curves is now fairly well captured, which was not the case with the previous models at all. Of the coupling parameters that were investigated, the ratio of the thicknesses had significant effect on the simulation results, and it provided the only way to approach the measured curves. The connection modelling method in this case can now be assumed to be correct.

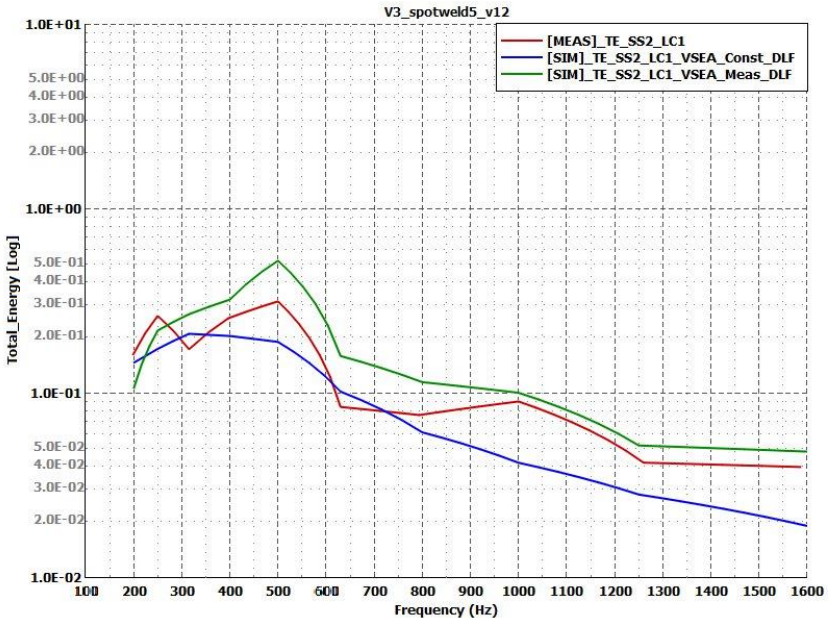

Figure 34. Energy response of the receiver plate for Test Case 4: spotwelded variant with different thickness ratio. Measurement – red curve; simulation with constant damping – blue curve; simulation with measured damping – green curve.

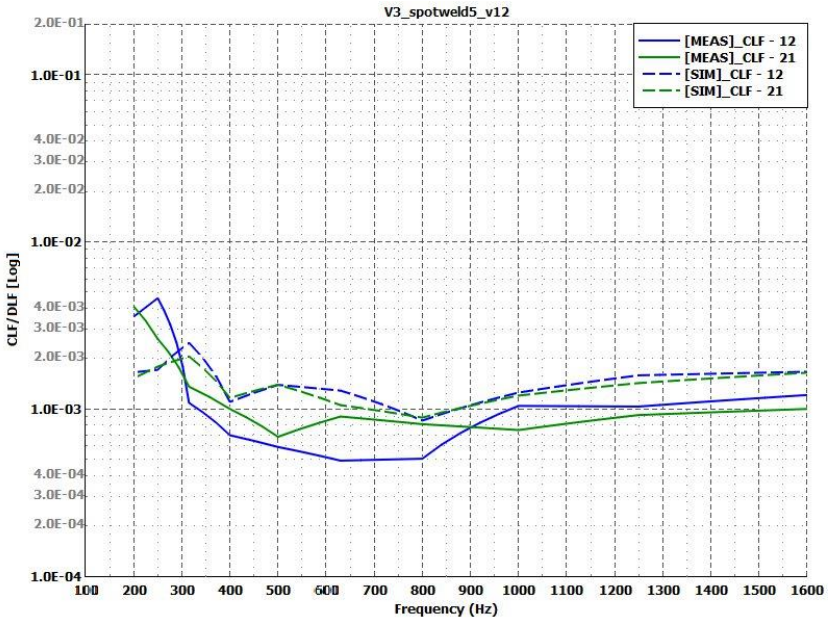

Figure 35. Coupling Loss Factors for Test Case 4: spotwelded variant with different thickness ratio. Measurement – solid lines; simulation – dashed lines.

5.6. Summary and conclusions

The finite element modelling method of the most common connection types was investigated through comparison of experimental and virtual power injection method. These connections included bent, line welded, superglued and spotwelded junctions. Two types of simulation results were tested to measurement data in each case: first, based on no experimental data, where the global damping of the simulation model was a constant value; and second, where the damping of the two plates came from the experimental PIM to get a better understanding of the behavior of the other influencing factors and a better insight to the validity of the models. In the case of the bent, line welded and superglued variants, the simulation models represented the realistic behavior of the physical models, apart from some low frequency discrepancies, where probably the SEA assumptions were not entirely respected. The overall quality of these models was satisfactory, in terms of the response of the receiver plate and the coupling loss factors too. Discrepancies that could be seen in Figure 17 – Figure 22 can be attributed to the high sensitivity of the model to the measurement parameters, such as boundary conditions, excitation and response point locations. The model uncertainties due to manufacturing tolerances, imperfections, welding distortion, etc. can also be responsible for deviations.

However, the spotwelded variant showed unexpectedly large discrepancies. The effect of the main influencing factors of the connection modeling method was investigated in a DOE. It was found that the changes in the connection stiffness and in the diameter of the connection area

slightly affected the results, while the thickness ratio of the connecting plates had an immense effect on them. Control simulations scattered in the design space validated prediction quality of the response surfaces. The change in the thickness ratio of the plates proved to be the most influential factor and improved the simulation results drastically. It was shown that the connection modeling method used for spotwelded connection can be regarded valid once the geometrical properties, with particular emphasis on the thicknesses, are clarified. Further studies may investigate in the same manner the other connection types that had been studied in Ref. [56], e.g., the bolted type, the more densely spotwelded one or all of those variants in a various connection angle. These would provide valuable results on validity of the finite element modeling of each connection type.

5.7. Thesis 1

I proved that the damping and coupling effects of various junction types can be accurately considered in Virtual SEA through the proper finite element representation of the connection. The most common junction types that can be found on a vehicle chassis structure, have been validated by comparing experimental and virtual power injection method results for set of coupled plates. The effects of the finite element connection modeling parameters have been explored in a Design of Experiment, and I proved that the most influential ones are the geometrical properties, in particular, the thickness ratio of the connecting plates. The changes in the connecting element stiffness and the diameter of the connection point have less influence on the Virtual PIM results [II].

6. CLUSTERING-BASED SUBSYSTEM GERNERATION FOR VIRTUAL SEA

As described before, building an SEA model is far from straightforward in real life applications, because it has to comply with certain requirements. Since the hand-made SEA subsystems do not always entirely meet these, more advanced methods, such as the use of clustering techniques have already been proposed. While a number of studies provide thorough analysis of SEA subsystem validities and coupling strengths on models with different complexity, none of them focuses on the comparison of different clustering methods and validates the results via FE simulation. Therefore, this Chapter aims to assess and compare various subsystem divisions achieved by different methods on a simplified car body model and measure their accuracy. The evaluation of each model is based on the fulfillment of the SEA assumptions described in Chapter 4.3. Since any violation of those may result in incorrect predictions by the method, the results of each clustering model are compared to a reference finite element simulation. The techniques presented here could also help to reduce the time spent on SEA model building and give consistent, reasonable results.

6.1. Numerical model review

The numerical model that was used for comparison of different subsystem divisions is a simplified car structure. This simplified model helped to reduce computational costs but at the same time, it is complex enough to present the capabilities of different subsystem generation approaches. The same finite element model was used for both the validation of the Virtual SEA results and for extracting the modes and matrices for the Virtual PIM. The model consists of around 43 000 first order shell elements with an average size of 25 mm and around 43 000 nodes. Each panel has a thickness of 2.5 mm and steel material properties, which makes the model valid up to around 5 000 Hz according to the finite element mesh size criteria. The material properties are summarized in Table 5.

Table 5. Material properties of the FE car body model.

Young's modulus	210 000 MPa
Poisson ratio	0.3
Density	7 850 kg/m^3
Structural damping coefficient	0.01

For the Virtual SEA models, the global damping was set to 1%, which is equal to the structural damping coefficient in the FE simulations. There were 3 load cases defined, each with a unit force excitation in Z direction at the front right and rear right fenders and at the back of the floor, shown in Figure 36. The evaluation points were chosen on the largest panels of the car structure, which are usually the main contributors to the sound pressure level inside the cabin in real passenger cars. In these locations, the averages of the squared velocity results are compared. Two points were selected on the windshield and 4-4 points on the roof and floor panels, as shown in Figure 37. Both the FE and the Virtual SEA simulations were performed up to 1 120 Hz. The modal base for the Virtual SEA simulations were calculated up to 1120 Hz, yielding approximately 2000 modes. The reference FE simulation used a higher frequency modal basis due to modal truncation, extracted up to 1600 Hz. The number of modes in this case was close to 3200.

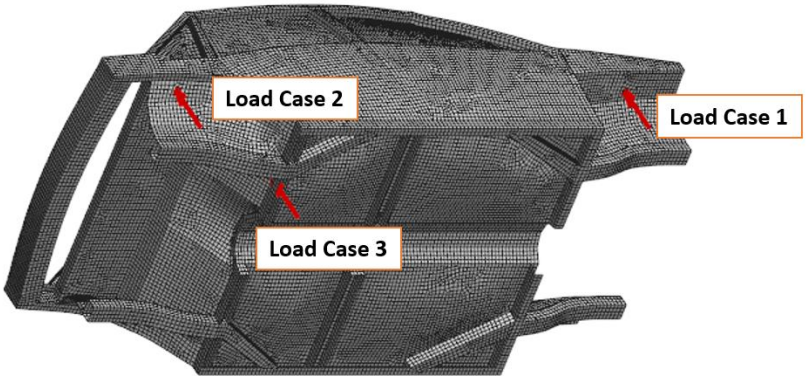

Figure 36. Excitations applied to the numerical model.

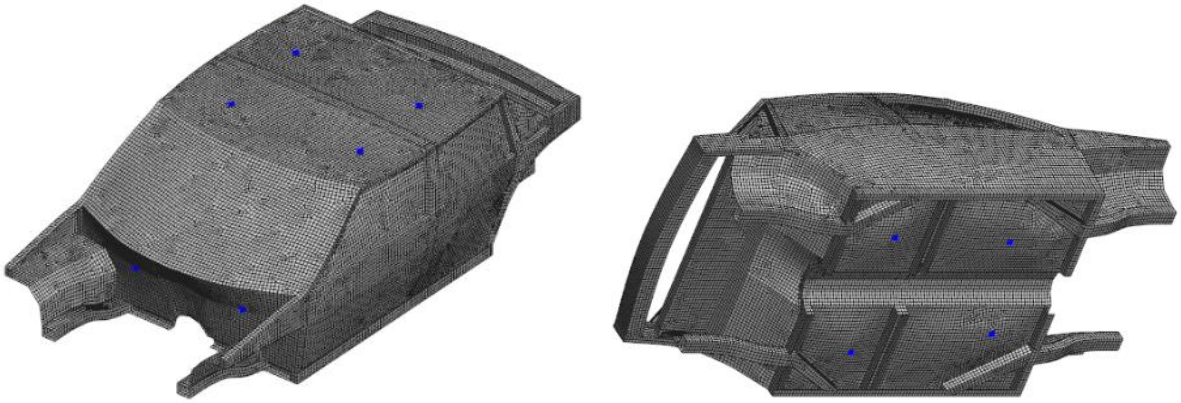

Figure 37. Response points of the numerical model.

6.2. Manual partitioning

As the basis of the comparison of different SEA subsystem divisions, one model was built up manually by defining each subsystem based on intuition, as it would be done in traditional SEA. This division is shown in Figure 38. In this case, every large panel or individual part of the car body structure forms a separate subsystem, which makes sense from SEA point view. After the analysis was performed, the direct CLFs (i.e., the CLFs between adjacent subsystems) were investigated for each frequency band. In the main diagonal of the CLF matrix, the damping loss factors are indicated. According to the weak coupling assumption in SEA theory, the off-diagonal CLF values should be lower than the DLFs in the main diagonal.

Generally, it can be observed in Figure 39 that as the frequency increases, the coupling between the adjacent subsystems becomes weaker. In the lowest frequency bands, the weak coupling condition is not always met, associated with subsystem pairs with relatively high coupling loss factor values (see for example, subsystems 15 and 14, corresponding to the rear left door and the rear left fender). However, the 400 Hz and the 1 000 Hz results show that the model perfectly fulfills the weak coupling criteria. The reciprocity relation of the SEA model is also investigated in an analogous way in Figure 40. The matrix of the reciprocity coupling loss factors for the adjacent subsystems are subtracted from the direct coupling loss factors, so that the reciprocity is fulfilled when all of the elements are close to zero. The difference of the CLFs and the reciprocity CLFs shows similar results as the coupling weakness investigation. At the lowest frequencies, the reciprocity relation cannot hold, but as the frequency increases, the values become closer to zero, indicating the validity of the model. The obtained SEA model was compared to the FE simulation in the previously described load cases in Figure 41. The dashed lines show the FE results, while the solid lines correspond to the Virtual SEA. For load cases 2 and 3, the average of the squared velocities in the response points show very good agreement between FE and Virtual SEA, while for load case 1, the trends are captured. Generally, however, at high frequencies the results appear to be more acceptable based on the coupling conditions and the overall quality of the data. Even in the low frequency range, where the SEA assumptions are not entirely respected, the FE results are represented quite well.

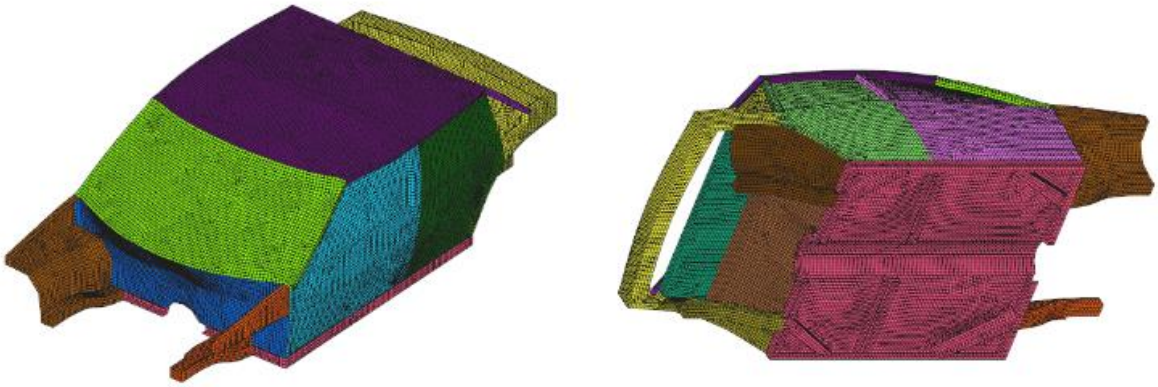

Figure 38. Manual partitioning of the Virtual SEA model.

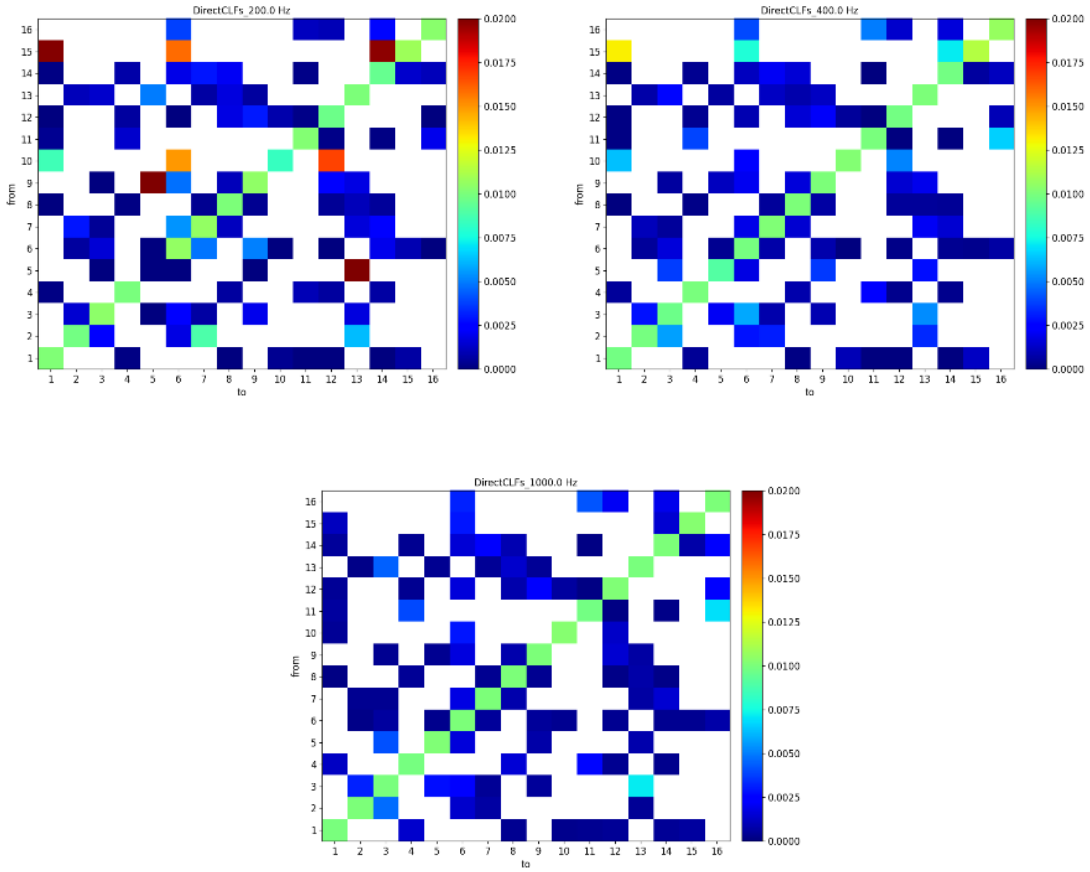

Figure 39. Direct CLF matrices in 200 Hz, 400 Hz and 1 000 Hz frequency bands for manual partitioning.

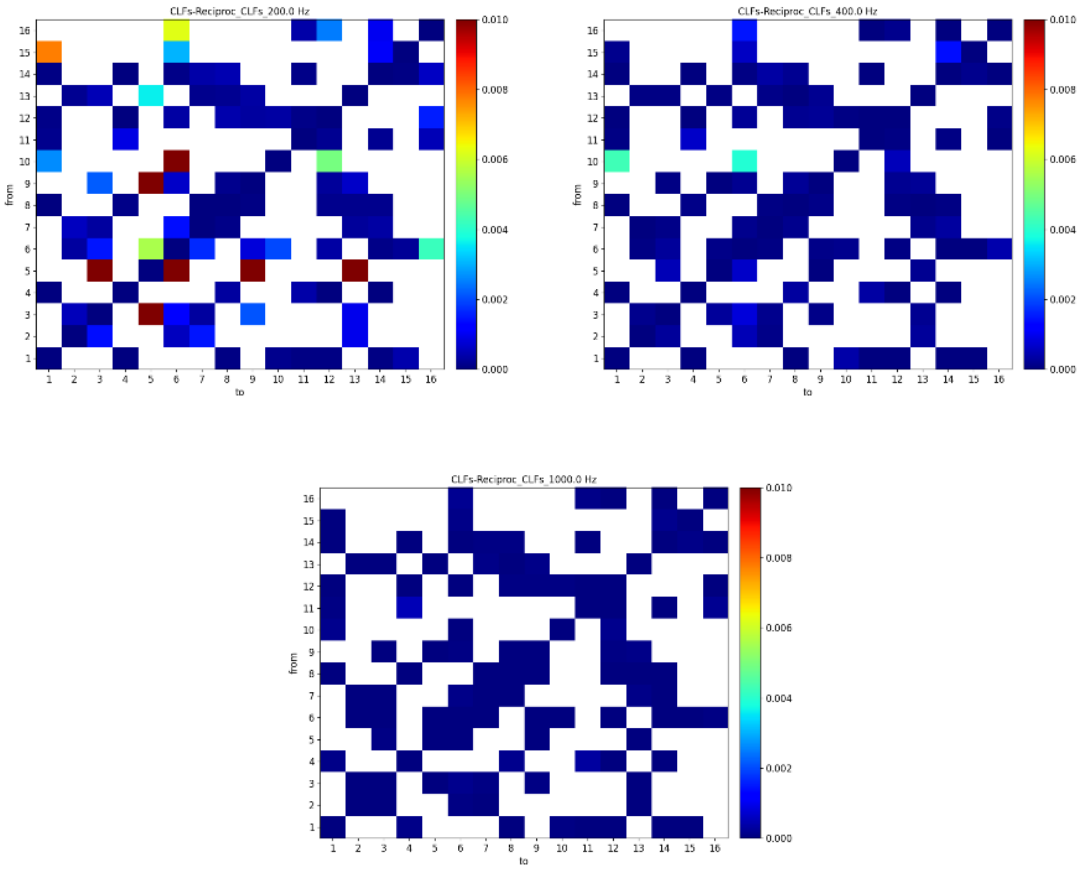

Figure 40. Difference of Direct CLF and reciprocity CLFs in 200 Hz, 400 Hz and 1 000 Hz frequency bands for manual partitioning.

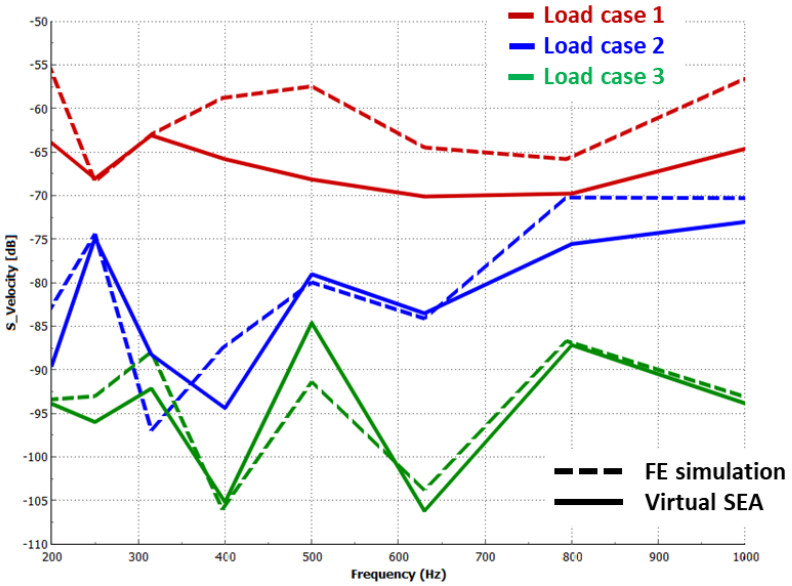

Figure 41. Comparison of FE (dashed lines) and Virtual SEA (solid lines) with manual partitioning. Averaged squared velocity of response nodes in 3 load cases. Red – front right fender excitation, blue – rear right fender excitation, green – floor excitation.

6.3. K-means partitioning

In the case of the second model, the subsystems for the Virtual SEA simulation are generated by K-means clustering algorithm. First, the structure was divided into many small parts that were excited to create a large matrix of transfer functions. These functions were averaged over the frequency bands and projected into two-dimensional space using Principal Component Analysis (PCA). Then, the reduced data was fed into a custom Python script using a built-in clustering module for the K-means cluster analysis. In this type of clustering, the final number of the clusters is required to be specified initially, which is a great drawback of the method. But still, compared to the entirely manually defined subsystems, the results depend to a lesser extent on modelling intuitions. Based on the previous model, 12 subsystems were specified in this case, and the so-obtained result is shown in Figure 42.

There are some key differences that are worth mentioning, when comparing to the manually created division. The front parts of the car body – i.e., the front fenders, the firewall and the front doors – form one large subsystem, while in contrast to this the rear of the car is divided into numerous smaller subsystems. Most significantly, the rear fenders were split, which are relatively small parts. The two largest panels – the floor and the roof – are also split into two different subsystems. The direct CLFs obtained through the Virtual PIM are shown in Figure 43 for each frequency band. As the results in Figure 43 depict, at low frequencies the semi-automated K-means clustering process performs similarly to the manual division, although there appear to be some high coupling values from subsystem 12 to 3 and 9, representing the rear fenders and the rearmost part of the car. For the latter, the damping is also too high compared to the defined value at the low frequency bands. This issue is solved towards to the higher frequencies, but the coupling between subsystem 9 and 12 remains too high. This was already conspicuous at the visual inspection of the subsystems. Regarding the reciprocity relation at low frequencies, it can be observed in Figure 44 that subsystem 9 is the main source of the model deficiencies. However, it is clearly visible on this subsystem that the model becomes better and better as the frequency increases. In the highest frequency bands, the direct and the reciprocity CLSs are almost equal, indicating the validity of the model in this regime. Despite the CLFs results showing no signs of any improvement, the agreement between FE and Virtual SEA with the K-means clustering is very good for load case 2 (blue) and 3 (green), shown in Figure 45. Also, for load case 1 (red), the discrepancies around 500 and 800 Hz were reduced slightly. The low frequency correlation is also notable. Overall, the SEA model with

the K-means clustering is acceptable, but there is room for improvement by fine tuning the clustering parameters and by checking and correcting the results if necessary.

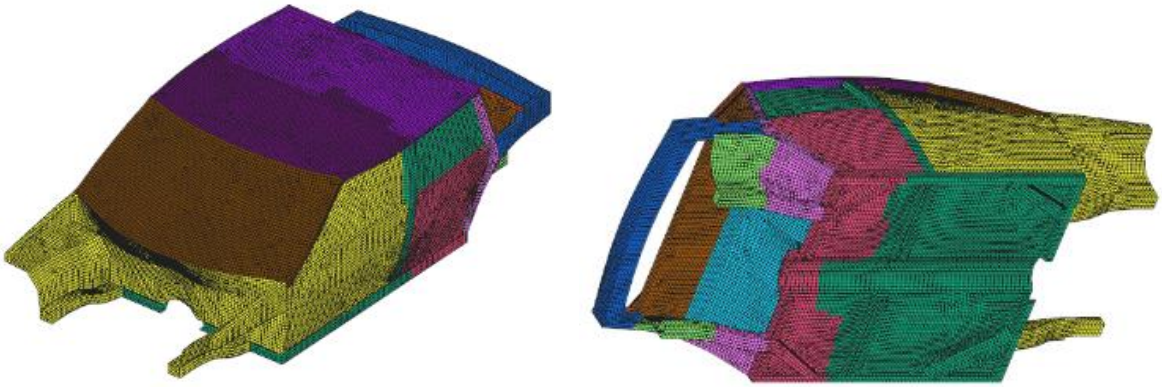

Figure 42. K-means partitioning of the Virtual SEA model.

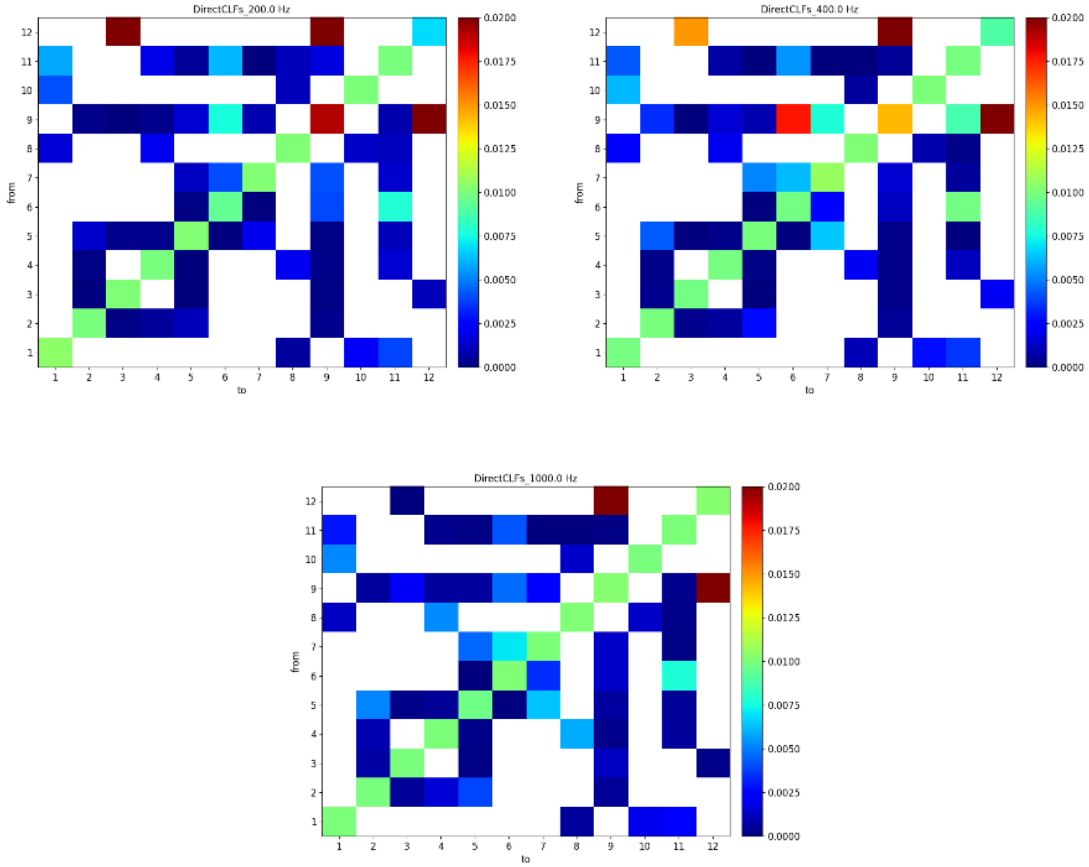

Figure 43. Direct CLF matrices in 200 Hz, 400 Hz and 1 000 Hz frequency bands for K-means partitioning.

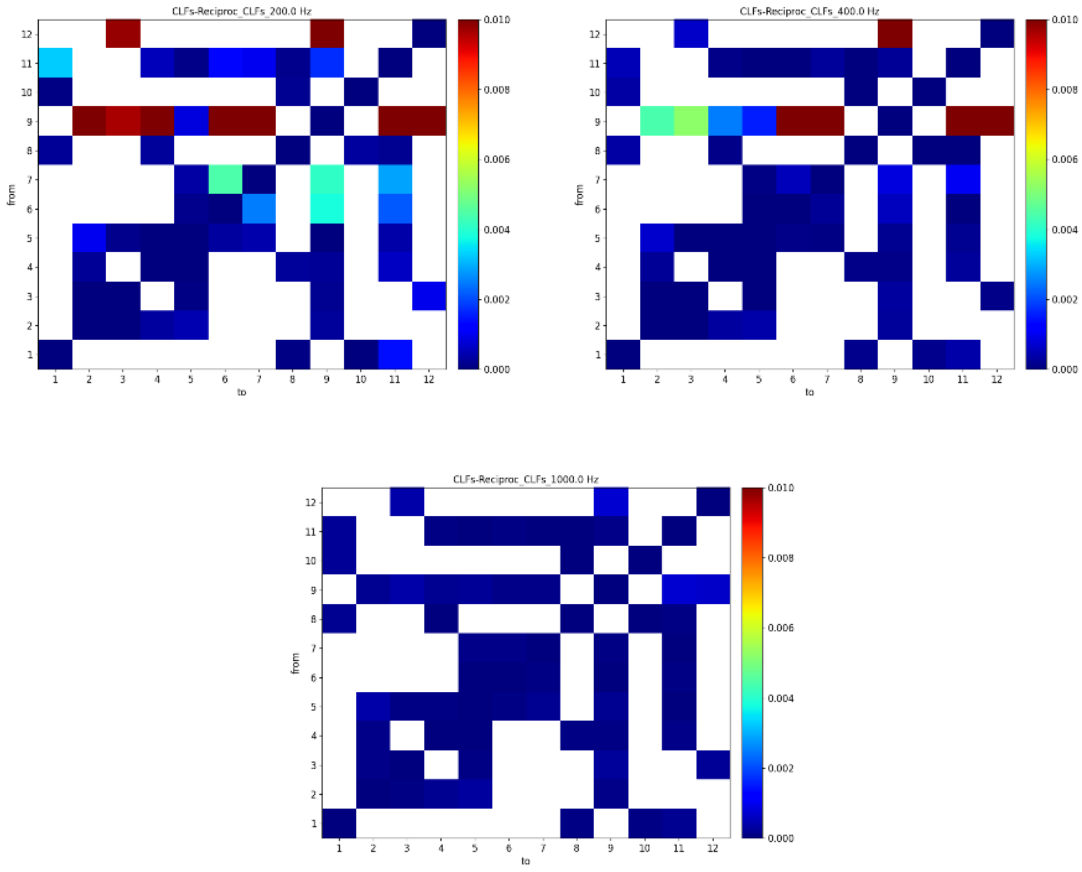

Figure 44. Difference of Direct CLF and reciprocity CLFs in 200 Hz, 400 Hz and 1 000 Hz frequency bands for K-means partitioning.

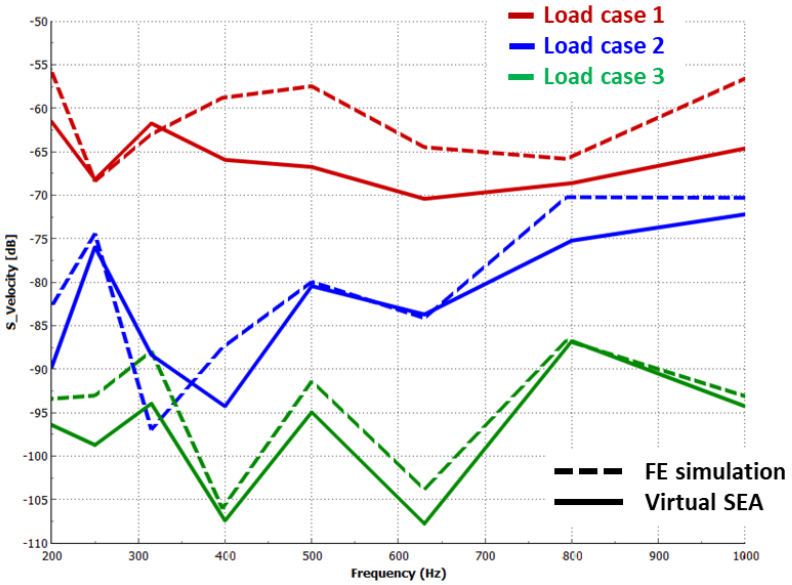

Figure 45. Comparison of FE (dashed lines) and Virtual SEA (solid lines) with K-means partitioning. Averaged squared velocity of response nodes in 3 load cases. Red – front right fender excitation, blue – rear right fender excitation, green – floor excitation.

6.4. X-means partitioning

The model described in this chapter attempts to fix the deficiencies of the K-means clustering model. Recall, that in the K-means model, the number of clusters is provided by the user. On the other hand, the X-means algorithm starts with an initial number and adds centroid in each iteration until it reaches the upper bound and selects the best score for output. The algorithm that was used also comes standard with an open-source Python module. The input dataset for this analysis was produced in the same way as it was for the K-means. In this case, the initial number of clusters is set to 10 and the maximum to 20. Additionally, the results were overlooked and corrected before the Virtual SEA in order eliminate the most obvious modeling mistakes, such as disconnected subsystems. These occurred in the K-means analysis e.g., at the rear fenders, or at too large subsystems, such as the whole front of the car. This resulted in 12 raw subsystems, which differ from the K-means results due to different initialization. After postprocessing, the final results consist of 16 subsystems, shown in Figure 46.

This model also features some characteristic attributes that are kept during the analysis. The firewall, for example, is split into two parts and the roof subsystem is extended down to the B-pillars. The C-pillars, the rear windshield and the back panel of the cabin are in one subsystem. The CLF results, shown in Figure 47, are quite similar to the previous analyses at low and mid frequencies. There are a couple of connected subsystems with high coupling values, for example subsystem 3 and 6, corresponding to the rear left fender and the floor, respectively. These CLFs get lower at the mid frequency range. However, at the high frequency bands, the coupling between subsystem 16 and 5, which are the two parts of the firewall, increases. This suggests that these are not valid SEA subsystems and should be joined together. From the reciprocity relation point of view, the X-means model seems to be improved compared to the previous models. There are less values far from zero at the lower frequencies and starting from 400 Hz, even these values are also reduced. At the 1 000 Hz frequency band, the direct and the reciprocity CLFs are almost equal, as shown in Figure 48. Regarding the comparison to FE results at the response points, Figure 49 shows that the X-means model performed slightly worse than the K-means model for load case 1 (red), and for load case 2 (blue). Load case 3 (green) once again shows good correlation with the FE analysis. It can be concluded from this model that some of the characteristic features should have been avoided, for example the splitting of the firewall. The results then would have been similar to the manually defined subsystems, but with the advantage of being partially automatized.

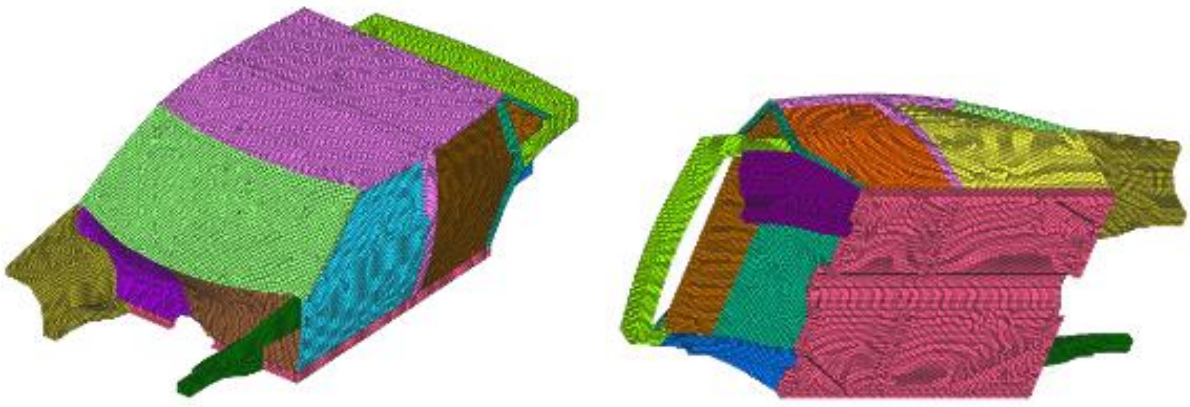

Figure 46. X-means partitioning of the Virtual SEA model.

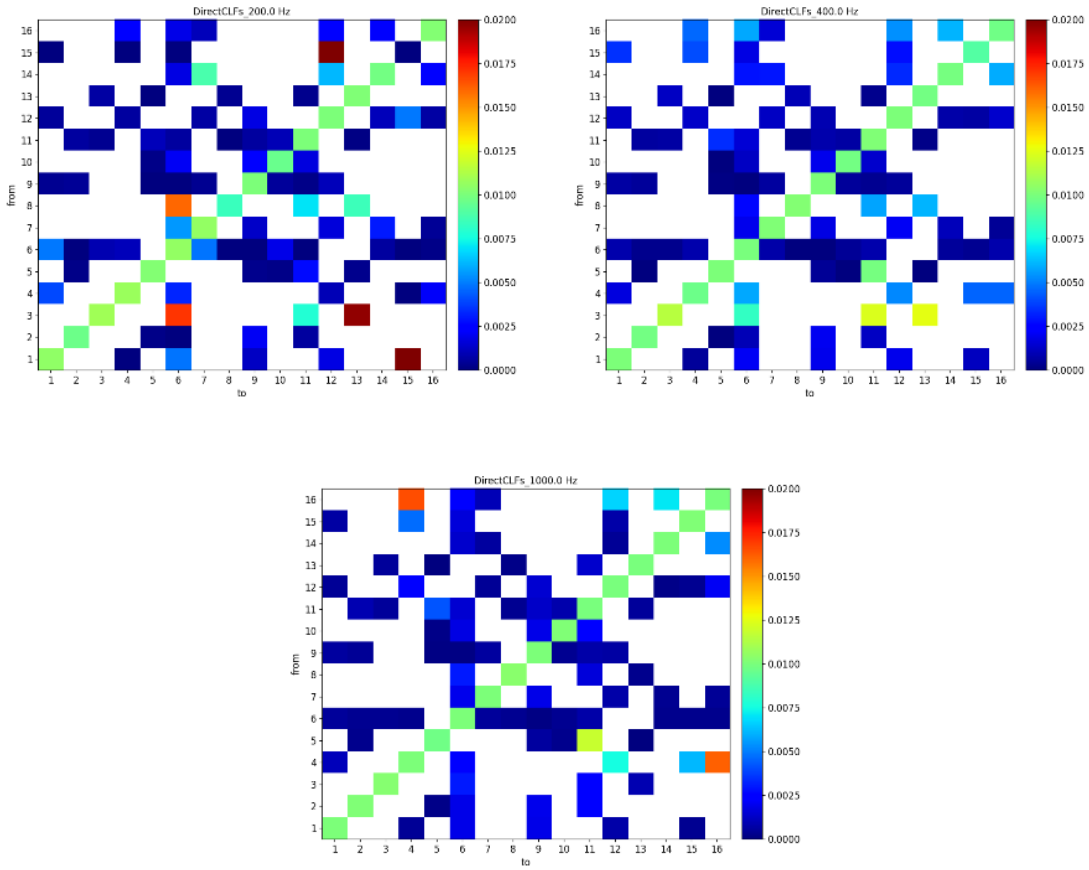

Figure 47. Direct CLF matrices in 200 Hz, 400 Hz and 1 000 Hz frequency bands for X-means partitioning.

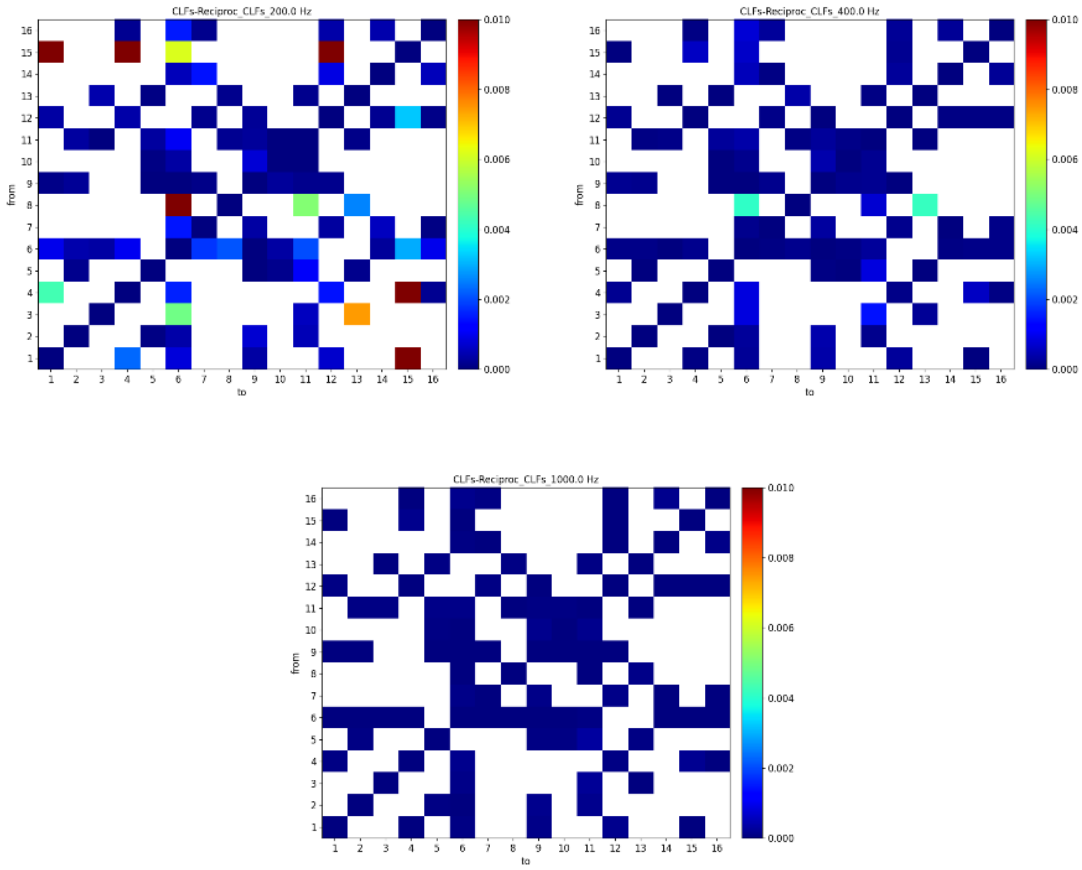

Figure 48. Difference of Direct CLF and reciprocity CLFs in 200 Hz, 400 Hz and 1 000 Hz frequency bands for X-means partitioning.

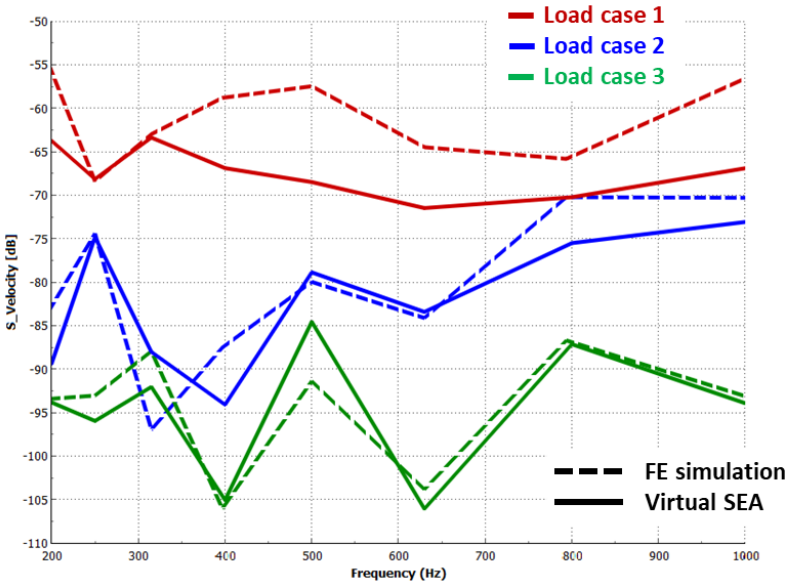

Figure 49. Comparison of FE (dashed lines) and Virtual SEA (solid lines) with X-means partitioning. Averaged squared velocity of response nodes in 3 load cases. Red – front right fender excitation, blue – rear right fender excitation, green – floor excitation.

6.5. Automatic partitioning in Virtual SEA

The last subsystem division was created by the automatic subsystem generation algorithm implemented in MSC Actran's Virtual SEA module. The method uses a particular clustering method that allows to regroup an initial, coarse number of parts into SEA subsystems [81]. Two parameters must be provided for such analysis: the frequency range to consider and the number of initial parts. The handling of the disconnected subsystems can also be specified. Since this is a fully automated process, it is the easiest to use as the first step of a complete Virtual SEA simulation. For this study, a number of 400 initial parts was defined and the frequency range from 300 Hz to 600 Hz was considered. Any disconnected subsystem was managed and merged into their neighboring subsystems, after evaluating the pure results. The whole subsystem generation sequence completed in less than 10 minutes, which is a fraction of the time requirements of the previously described, semi-automated methods. The final division of the car obtained by the automatic process is shown in Figure 50.

There are only 6 subsystems identified by the algorithm, corresponding to the left, right, front, rear side of the car and to the floor and roof panels. These form relatively large subsystems, compared to the previous partitioning methods, apart from the floor and roof panels that were identified previously as well. It can be observed as well that the boundaries of the subsystems do not strictly coincide with the boundaries of individual parts. After performing the Virtual power injection method, the CLF results in Figure 51 show that the results of this automatic subsystem generation meet the SEA weak coupling assumptions best. Even in the lowest frequency band, at 200 Hz, all the coupling values are lower than the damping values in the diagonal. The highest value comparable to the damping occurred between subsystems 3 and 5, corresponding to the floor and the left side of the car. At higher frequencies, there are no outstanding CLFs in the matrices, which proves the high quality of the model from SEA point of view. The model validity is also confirmed by the reciprocity CLFs, as shown in Figure 52. At 200 Hz, the difference between the direct and the reciprocity CLFs are closer to zero than in other cases. From 400 Hz onwards, the values in the matrices are basically zero. Regarding the averaged squared velocity results at the response points, shown in Figure 53, the automatic subsystem generation model gets closest to the FE reference results. For all the load cases, the discrepancies are within the 5 dB range. Most notably, the correlation in load case 1 (red) is satisfactory, although the previous models struggled to achieve such decent quality results. The low frequency behavior of the model is also very well represented in Virtual SEA. Overall, the Virtual SEA with the built-in automatic subsystem generation algorithm is the most efficient

and most accurate way of model building from both SEA model validity and results quality point of view.

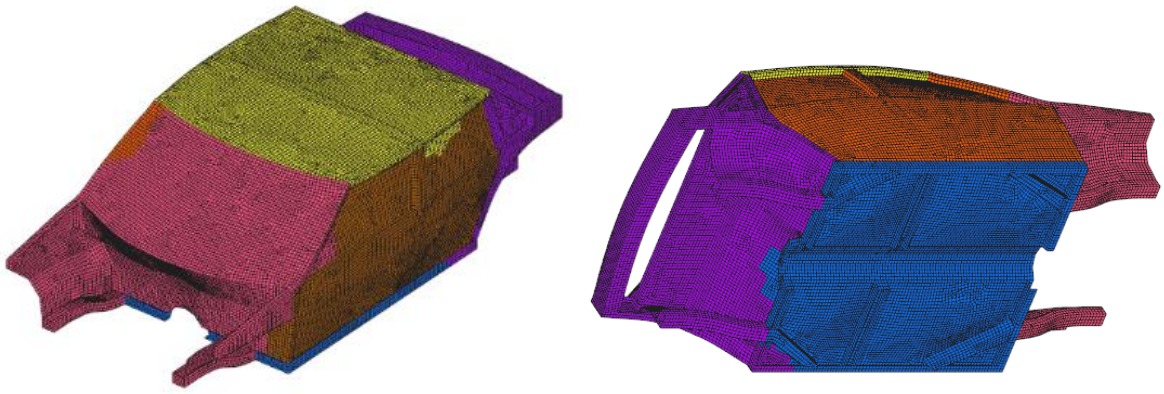

Figure 50. Automatic partitioning of the Virtual SEA model.

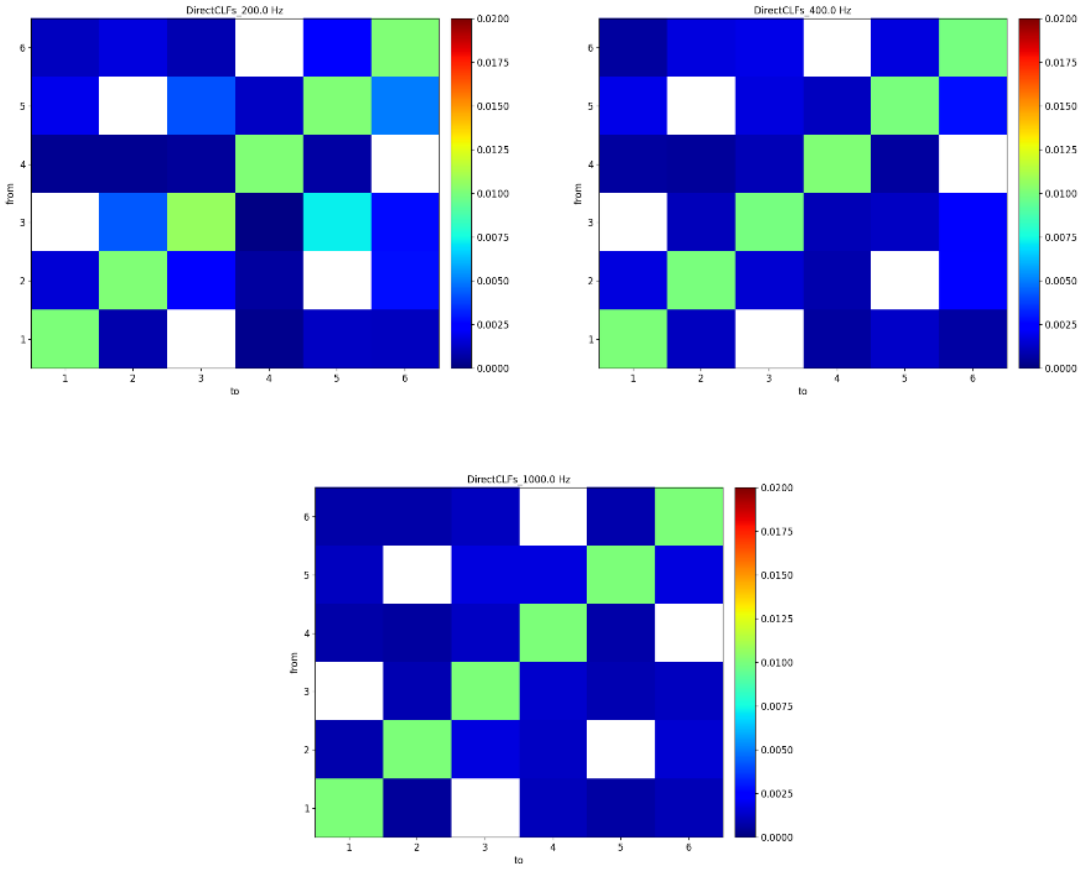

Figure 51. Direct CLF matrices in 200 Hz, 400 Hz and 1 000 Hz frequency bands for automatic partitioning.

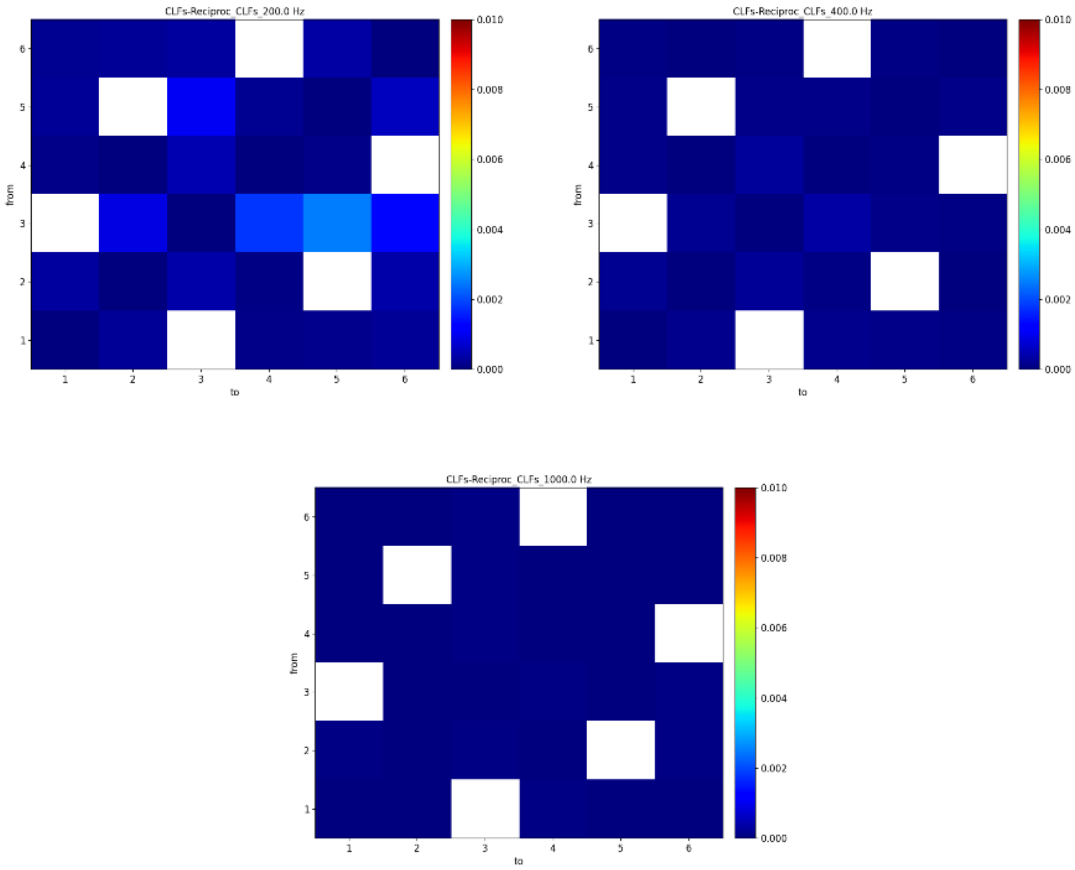

Figure 52. Difference of Direct CLF and reciprocity CLFs in 200 Hz, 400 Hz and 1 000 Hz frequency bands for automatic partitioning.

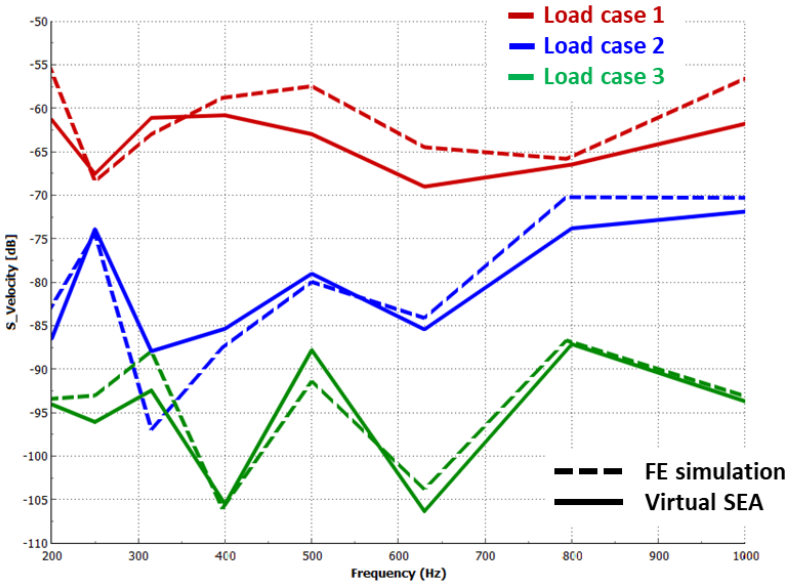

Figure 53. Comparison of FE (dashed lines) and Virtual SEA (solid lines) with automatic partitioning. Averaged squared velocity of response nodes in 3 load cases. Red – front right fender excitation, blue – rear right fender excitation, green – floor excitation.

6.6. Summary and conclusions

Different Virtual SEA subsystem divisions were investigated on a simplified, car-like model. The investigation involved the fulfilment of the weak coupling assumption and the reciprocity relation through the direct CLF and reciprocity CLF matrices. Each model was compared to a reference FE simulation by calculating averaged square velocities of response points located on the largest panels. In the first model, the subsystems were chosen manually. The disadvantage of this method is that the selection of valid SEA subsystems requires great expertise and experience, especially for a more general, complicated structure. With the complexity of the model, the time requirement of the subsystem definition could also increase. In this case, the direct CLF-reciprocity CLF matrices showed that the model can be considered valid from 400 Hz. On the other hand, the comparisons to the FE results were acceptable at lower frequencies as well but the model might show some uncertainties in this range.

The subsystems for the second and the third model were created by K-means and X-means clustering algorithms in Python. These methods eliminated the need for expertise for the model building and could save some time in this area. However, the resultant subsystem divisions are not improved significantly in terms of CLFs and reciprocity CLFs compared to the first model. Some of the setbacks could have been eliminated by a manual revision of the models. The comparison to the FE results showed similar agreement as the first model but the general validity of the model was not improved.

The last model was created using the built-in automatic subsystem generation algorithm in MSC Actran. The total number of systems was only 6, but the direct CLF-reciprocity CLF matrices confirmed that this is the best division that can be achieved, and the SEA assumptions are approximated as closely as possible. Even in the lowest frequency range, the model could be considered valid by the weak coupling and reciprocity criteria. The results of the response points were the closest to the FE results as well throughout the whole frequency range. Overall, the built-in algorithm is proven to be the most effective and accurate clustering method for creating valid SEA subsystems at the lowest frequency bands. In addition, the model building became reasonable and consistent, and the modeling times could also be reduced using this method.

6.7. Thesis 2

I formulated a novel procedure to compare different subsystem divisions for the Virtual SEA approach. Based on this procedure, I proved that clustering algorithms are able to provide subsystem divisions that comply more with the assumptions of the SEA theory than the

subsystems defined intuitively by a user. The automatic subsystem generation feature implemented in MSC Actran has been proven to be superior to other clustering methods. I proved that ultimately, clustering-based subsystems lead to more accurate Virtual SEA models to be created in a more reasonable and consistent way, with less time spent on model building [I].

7. FULL VEHICLE TRIMMED BODY SIMULATION IN VIRTUAL SEA

The effectiveness of the Virtual SEA approach has already been proven in former studies for various complexity models, but none of them presented a full-scale, industrial test case containing fluid-structure coupling with poro-elastic trim parts in between. Therefore, in this Chapter, an extensive correlation study of a full vehicle trimmed body model is presented between measurement, finite element method and Virtual SEA.

7.1. Overview of the validation process

The model used for the validation of the structure-fluid coupling and the trim consideration in the Virtual SEA approach was a 2015 Audi A3 Limousine passenger car in Body-in-Blue (BIB) and Trimmed Body (TB) configurations. Measurement data provided by AUDI was available up to 1 200 Hz for both setups. The finite element simulations were performed up to 1 000 Hz for the BIB and 500 Hz for the trimmed configuration, due to the large computational demands of the reduced impedance calculation, described in Chapter 4.2. On the other hand, Virtual SEA simulations were feasible up to the frequency of the modal support, 1 000 Hz for the BIB and for the TB configurations as well, without drastic increase in the computational costs since the effects of the trim parts are considered via updating the neighboring DLFs and CLFs. Moreover, it is possible in MSC Actran's Virtual SEA to fit logarithmic functions to the space- and frequency averaged quantities computed during the virtual PIM and SmEdA and provide extrapolated results beyond the highest frequency of the modal support, up to 4-times the mesh validity [60]. This is only relevant up until a certain frequency, where other physical phenomena do not take effect, such as the appearance of new propagating waves, or the coincidence frequency phenomena [81]. Because of this, the extrapolation of the results was only used for the BIB configuration, providing results up to 4 kHz. An interpolation point at 2 kHz was added to guide the extrapolation, with the support of modes in the corresponding third octave frequency band.

7.1.1. Simulation model setup

The same finite element structure model was used for both modal frequency response simulations (BIB and TB) and for extracting the modes of the Virtual SEA simulations as well. This structure consists of about 4.9 million degrees of freedom. Due to the presence of the trim parts, two cavity models had to be employed, each containing approximately 200 000 degrees

of freedom. Once again, the finite element cavity models were the same for the modal frequency response and for the Virtual SEA simulations, in the appropriate setups. The average element size in all models provides 8 linear elements per wavelength at the maximal frequency of the structure and fluid modal extractions, thus they can be considered valid. Figure 54 and Figure 55 show the structure and the cavity models in the BIB configuration.

Excitations were defined in 3 load cases at 3 distinct locations, as shown in Figure 56. In each load case, unit point forces were applied in the vertical direction of the car. The point forces are converted to injected powers according to Equation (27). 2% constant damping was defined initially for the entire structural model. Subsystem accelerations were compared between the measurement, modal frequency response and Virtual SEA simulations. Direct correspondence between kinetic energy and acceleration over one period was used, written as:

$$a = \sqrt{\frac{8\pi^2 f^2 E_{kin}}{m}} \tag{60}$$

To calculate subsystem accelerations, the frequency response functions of 137 response points in the BIB, and 37 response points in the vicinity of the trim parts for the TB configuration were evaluated by averaging at least 4 response points results over subsystems. The sound pressure levels were compared in the trimmed configuration only, the main cavity contains 24, the trunk cavity contains 6 microphone points.

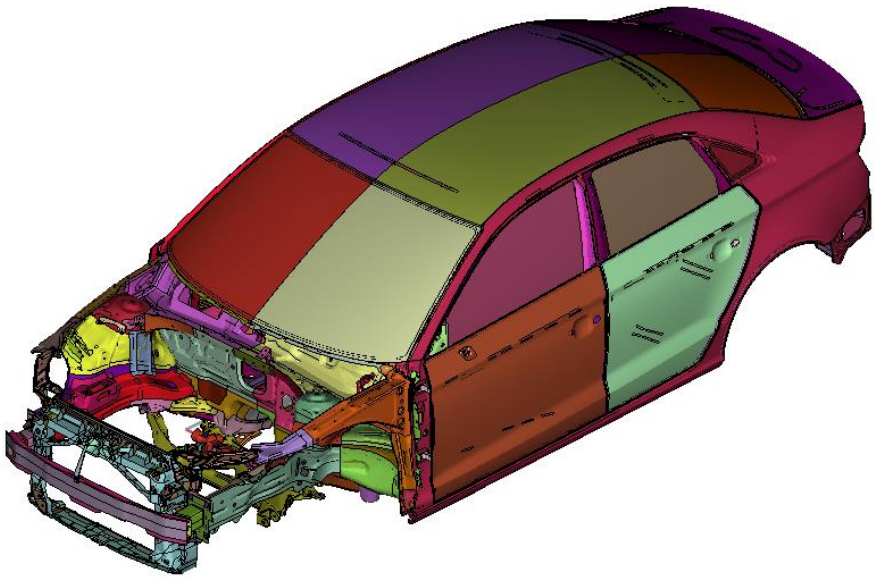

Figure 54. Finite element model of the car structure.

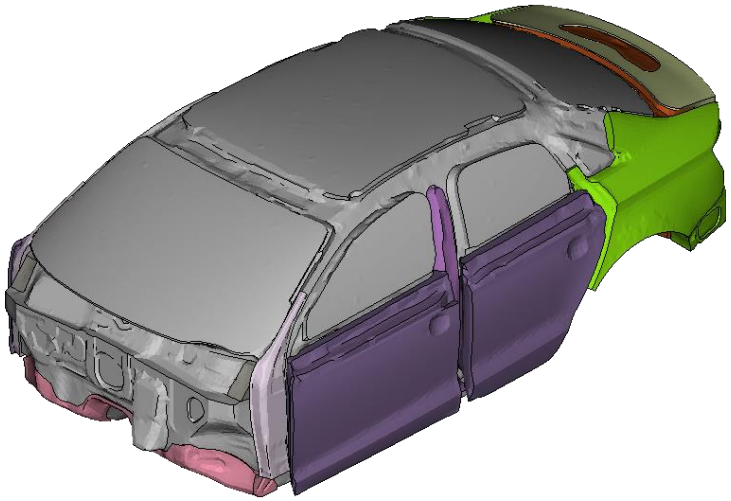

Figure 55. Finite element model of the car cavity in the BIB configuration.

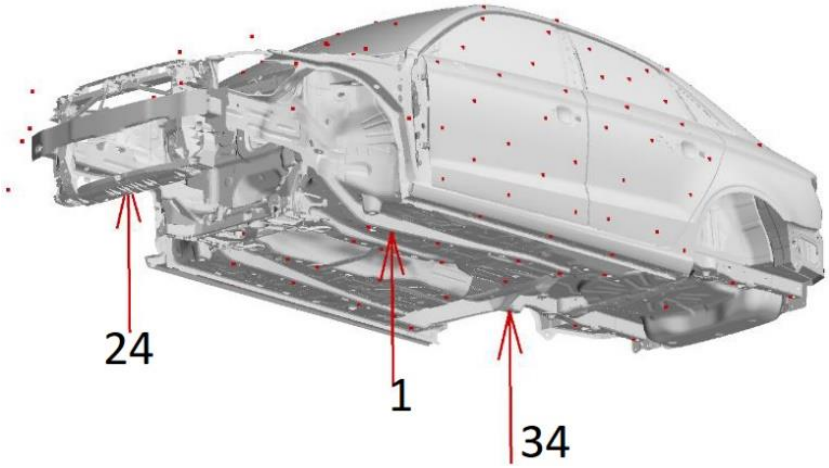

Figure 56. Excitation locations: 1 – front left floor, 24 – front right suspension mount, 34 – rear right suspension mount; 137 response points for the BIB configuration are marked by red points.

7.1.2. Virtual SEA model

As the previous chapter highlighted, the most efficient and accurate way of creating valid SEA subsystems is through the automatic subsystem creation algorithm implemented in MSC Actran. However, it is not possible yet to use this feature when trim parts are present in the model, because it is assumed that the trim parts cover most of the subsystem on which they are applied. Hence, the modification of the DLFs and CLFs affects the whole subsystem in connection with the trim part. So, in this case, the subsystem creation was driven by the desired output results – to make the averaging of FRFs reasonable – and by the presence of the trim parts. Nevertheless, the model validity was evaluated via the reciprocity relation. Figure 57

shows the partitioning of the car body model that consists of 39 structural and 20 fluid subsystems in the BIB, 42 structural subsystems and 2 cavity subsystems (main cavity and trunk) in the trimmed configuration. The changes between the two configurations were made due to the energy transfer through trims and to save computational time, since the trim effect is calculated separately for each subsystem and between each structure-fluid coupling that is affected.

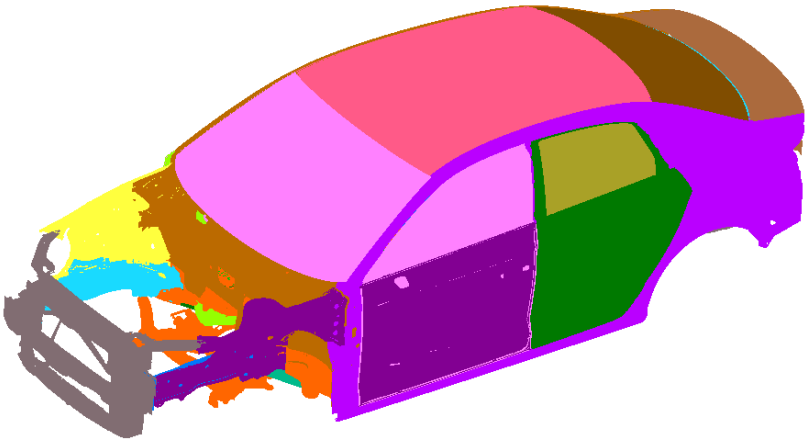

Figure 57. Partitioning of the structure model into SEA subsystems.

7.1.3. Trim models

The trimmed configuration models included the trim parts with the most significand effect in the simulations. These are the firewall insulation, the floor carpet, the headliner, and the rear seats. All of these contain poro-elastic materials in a multilayered structure, characterized by the Biot theory, described in Chapter 4.2. The effect of these parts is considered by the RIM approach in the finite element modal frequency response, and by the analytical equivalent transfer admittance approach in the Virtual SEA simulations. Virtual SEA uses a simplified layer structure that is constant over the trim part, while finite element method gives the opportunity for detailed modeling local variations in the layers. Virtual SEA can only account for the thickness scaling of the layers, according to Equation (38). Generally, the bottom layer (directly on the structure side) was scaled to fill the gap between the structure and the fluid. The approximate layer-structure of the considered trim parts are described according to Table 6.

Table 6. The layer structure of the considered trim part in the trimmed body simulations.

Trim part	Layer type	Material type	Thickness
Firewall insulation	Foam	Porous elastic	5 mm[1]
	Heavy layer	Isotropic elastic	2 mm
Floor carpet	Foam	Porous elastic	10 mm[1]
	Heavy layer	Isotropic elastic	2 mm
	Felt	Porous elastic	3 mm
Headliner	Airgap	Fluid	10 mm[1]
	Heavy layer	Isotropic elastic	6 mm
	Felt	Porous elastic	2 mm
Rear seats	Foam	Porous elastic	75 mm[1]
	Foam	Porous elastic	3 mm
	Felt	Porous elastic	1 mm

7.2. Reciprocity of the SEA matrix

As the previous Chapter showed, evaluating the reciprocity relation of the SEA loss matrix is a good indication of the validity of the Virtual SEA model. Figure 58 and Figure 59 show the CLFs with continuous lines and the reciprocity CLFs with dashed lines from the windshield and from the left frame subsystem to the neighboring subsystems, respectively. In general, the reciprocity relation is respected around 300 Hz onwards, which means that the Virtual SEA model can be considered valid above this frequency. It is also assured that no negative CLFs occur in this frequency range.

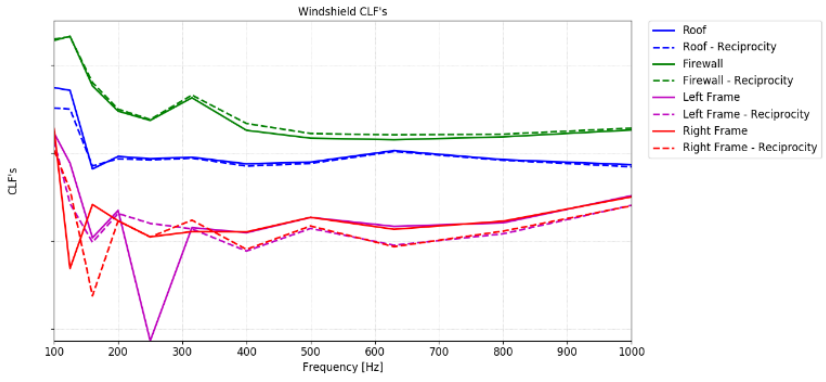

Figure 58. CLFs (continuous) and reciprocity CLFs (dashed) between windshield and roof (blue), firewall (green), left frame (purple), right frame (red).

[1] Scaled to match gap between solid and fluid

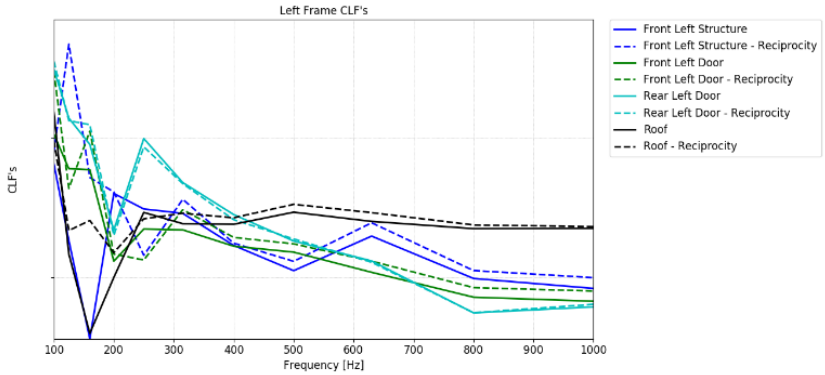

Figure 59. CLFs (continuous) and reciprocity CLFs (dashed) between left frame and front left structure (blue), front left door (green), rear left door (cyan), roof (black).

7.3. Results of the Body-in-Blue configuration

The global mean accelerations of the BIB model in all load cases were compared in Figure 60. Figure 61 shows the mean of all response points broken down to each load case. More detailed, local results averaged over different subsystems – front left door, front right window, frame left and roof – can be found in Appendix A. It can be observed in the global mean results of the 3 load cases that the modal frequency response and the Virtual SEA results overlap in their common frequency range, thus providing a smooth transition from the low frequency FE models to the mid- and high frequency range. The same agreement can be observed in the individual load cases. Both simulation approaches use the same eigenmode databases, thus the correlation was expected. Comparison of the simulation results to measurement data shows that the simulations correlate well up to 500 Hz, which is the typical validity of a fully scaled vehicle finite element model.

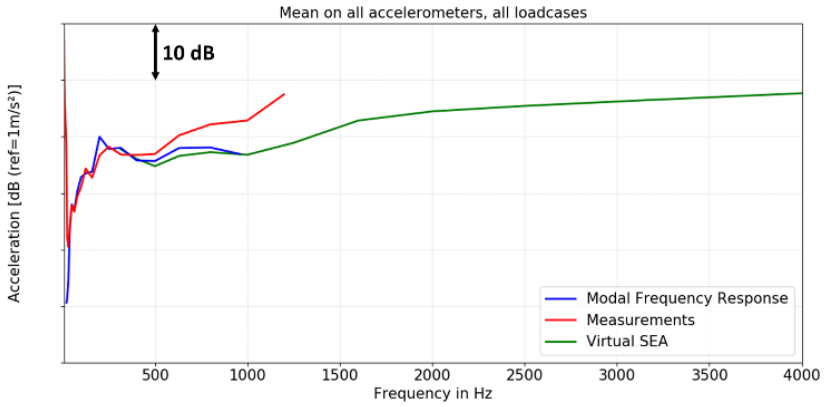

Figure 60. Mean accelerations of all response points in all load cases in BIB configuration, measurement (red), modal frequency response (blue), Virtual SEA (green).

Above 500 Hz the correlation is less good, presumably because of the changes of the global damping in the model. Similar agreement can be observed on the local scale in load cases 1 and 34. Load case 24 shows relatively good correlation with measurement even above 500 Hz, both for global and local results. It can be concluded that the Virtual SEA method provides the same accuracy as modal frequency response and can be used to assess the high frequency behavior of vibro-acoustic systems when the appropriate damping of the model is found.

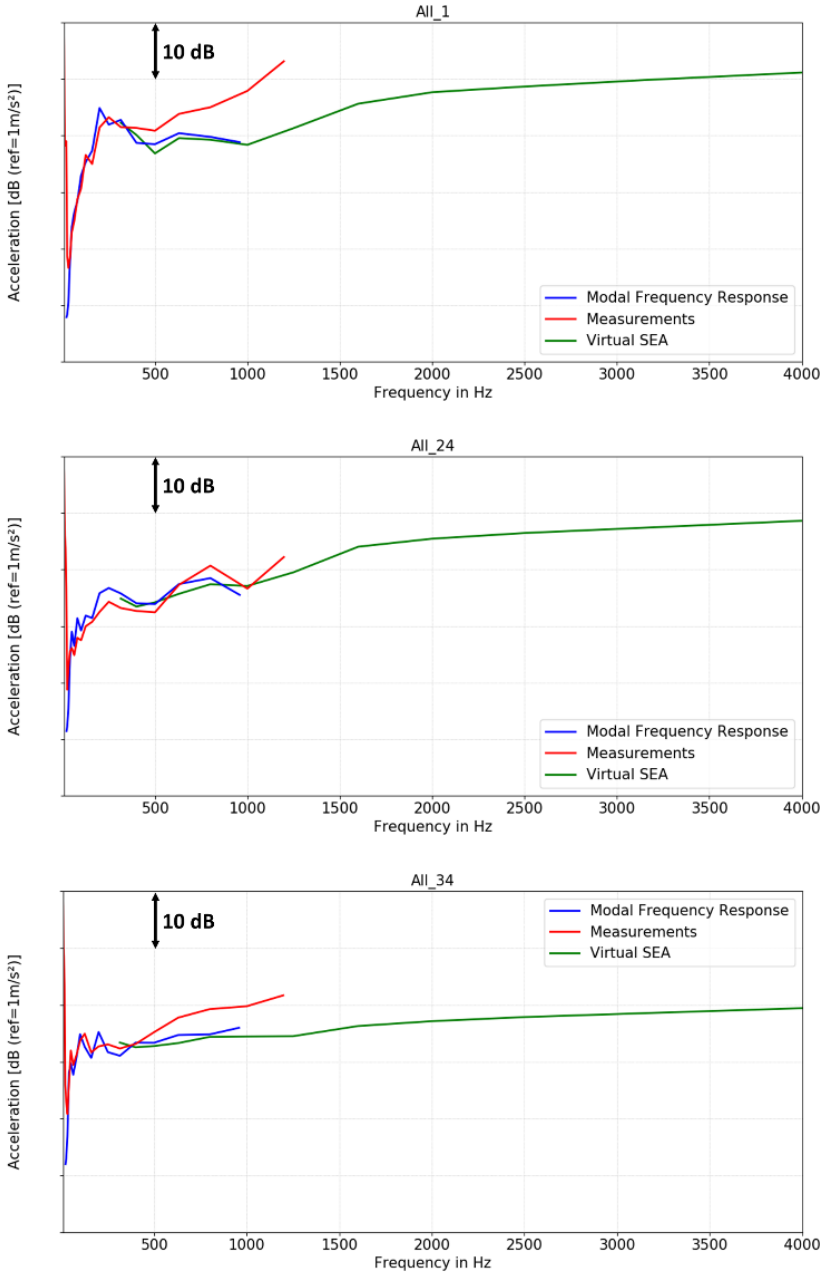

Figure 61. Mean accelerations of all response points in each load case in BIB configuration, measurement (red), modal frequency response (blue), Virtual SEA (green).

7.4. Virtual SEA results with tuned global damping

Due to the discrepancies in the results observed above 500 Hz, the potential in frequency-dependent global damping was investigated. Since the modal frequency response and the Virtual SEA provided the same accuracy, only the Virtual SEA model was rerun with the updated damping value that was first decreased from 2% to 1% globally, leading to better correlating results above 500 Hz. The global mean accelerations averaged all load cases is shown in Figure 62. Similar results can be observed in individual load cases in the global and local results too. The results suggest that frequency dependent damping needs to be used in the simulations to obtain good correlation in the entire frequency range.

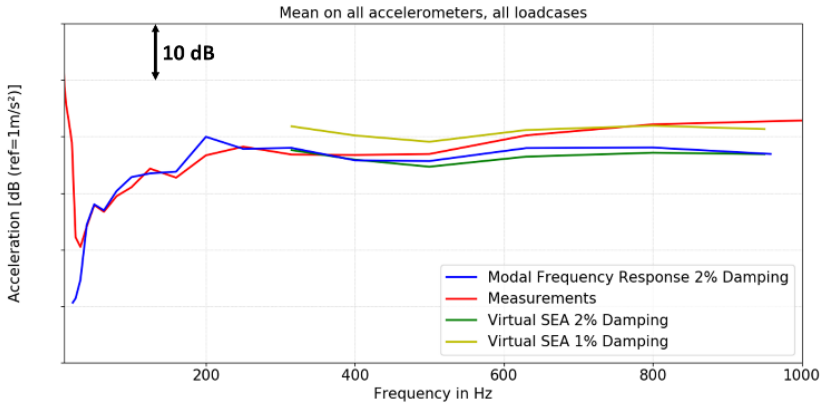

Figure 62. Mean accelerations of all response points in all load cases with adapted global damping in BIB configuration, Modal Frequency Response with original 2% damping (blue), Measurement (red), Virtual SEA with original 2% damping (yellow), Virtual SEA with adapted 1% damping (green).

7.5. Results of the trimmed configuration

In this section, the results of the TB configuration are shown, containing four different trim parts. Based on the finding of the previous section, frequency dependent damping was applied to the structure in the Virtual SEA model, described by a linear function between 2% and 1% over the 100 – 1 000 Hz frequency range. The damping in the cavity remained constant. The structural damping in the modal frequency response simulation was also unchanged, because it was found suitable for the frequency range the simulation is able to cover. The figures below show the mean results of the subsystems that have trim coverage, since the rest of the structure was unchanged, and the trim parts affect mostly the subsystems in their vicinity. Figure 63 shows the mean acceleration results over all load cases, while Figure 64 shows the same averages broken down to the 3 load cases. The global mean sound pressure levels in dB(A) are shown in Figure 65. The measurement results are shown by red curve, modal frequency

response is the blue one and the Virtual SEA results correspond to the green curve on each figure.

The correlation quality of the Virtual SEA results is satisfactory in general, the mean acceleration and sound pressure level results show good agreement with measurement. In load case 24 and 34, it can be observed that Virtual SEA overestimates the results, which is more pronounced in load case 34 where the difference from measurement can reach up to 5 dB. The reason for this discrepancy could be that the simplified trim model of the rear seats does not represent well the real seat structure with the defined layers and thickness scaling. The accelerations in the modal frequency response simulation start to diverge from measurement at 200 Hz in load case 1 and 34, resulting in a gap up to 10 dB between the two simulation methods. In these load cases, the finite element model and the corresponding trim parts need to be investigated, since this phenomenon was not present in the BIB configuration.

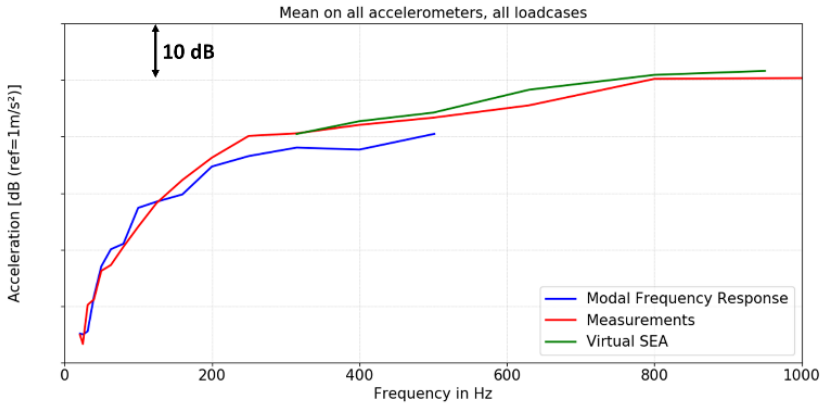

Figure 63. Mean accelerations of all response points in all load cases in trimmed configuration, measurement (red), modal frequency response (blue), Virtual SEA (green).

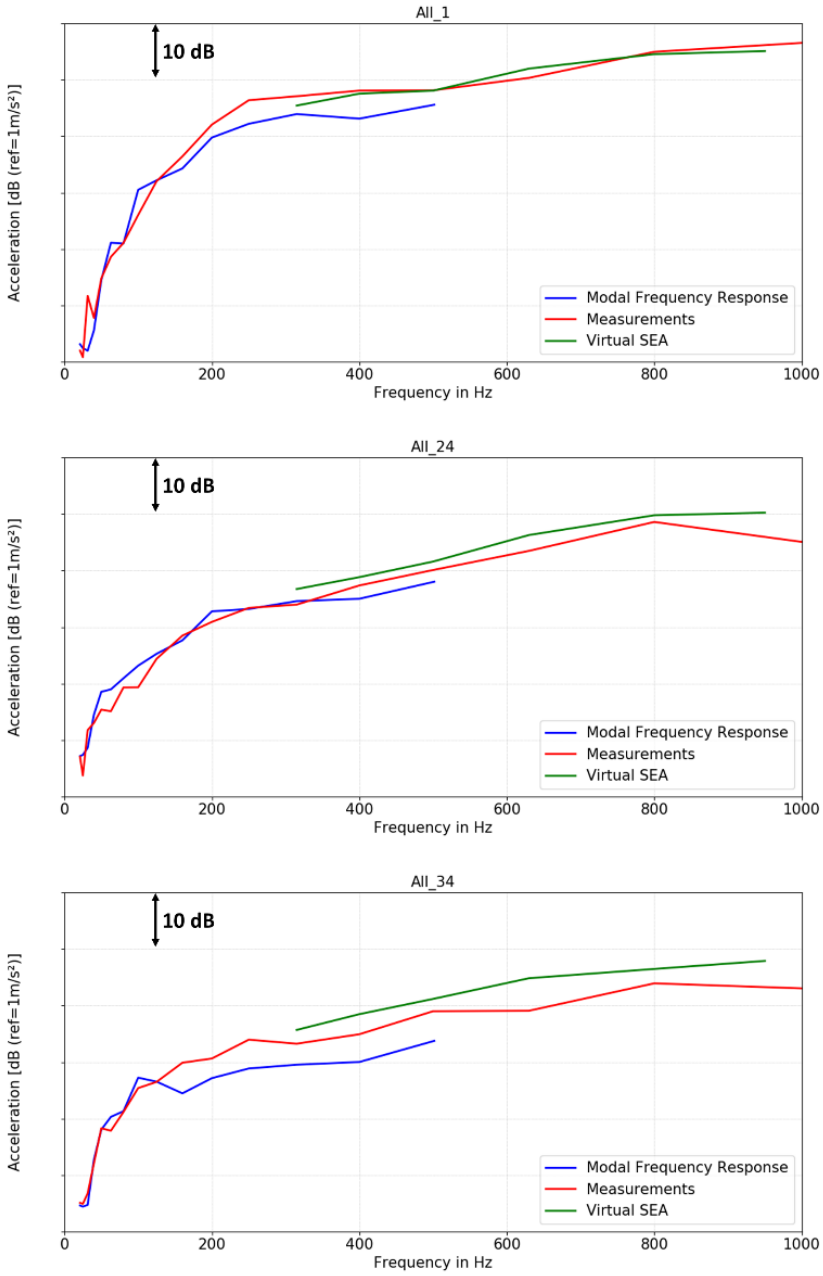

Figure 64. Mean accelerations of all response points of each load case in trimmed configuration, measurement (red), modal frequency response (blue), Virtual SEA (green).

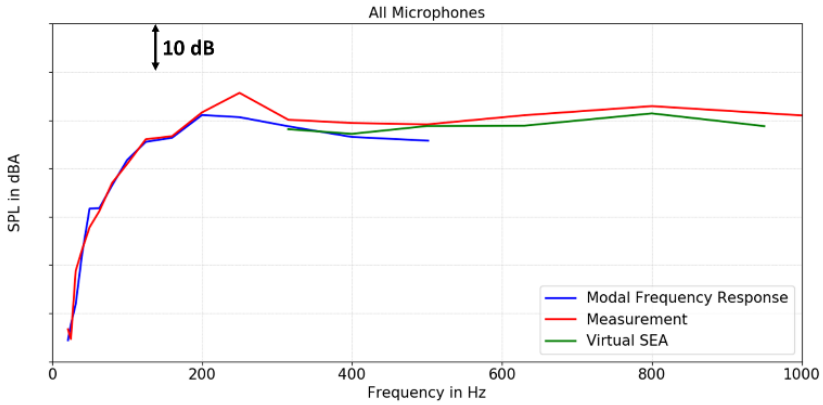

Figure 65. Mean SPL of all microphone points in all load cases in trimmed configuration, measurement (red), modal frequency response (blue), Virtual SEA (green).

7.6. Summary and conclusions

The effectiveness of the Virtual SEA approach was demonstrated in a full-scale, industrial case study. First, a comparison of experiment, modal frequency response and the Virtual SEA approach was presented in case of a full-scale vehicle without trims. The SEA model based on the finite element model was validated starting from 300 Hz, by evaluating the reciprocity relation. One of the advantages of the Virtual SEA method is that the same finite element models can be reused to cover the mid- and high frequency range though the effective use of modal bases and the extrapolation feature. The simulations showed good agreement with measurements up to 500 Hz. Above 500 Hz, where the original 2% constant global damping cannot hold anymore, the results started to diverge. Changing the global damping value from 2% to 1% in the Virtual SEA simulation led to a much better correlation with the measurement results in the high frequency range as well. The extrapolated results above 1 000 Hz still need to be validated by further measurements.

In the second part of this section, multiple trim bodies were considered in the model and a similar comparison was performed. The averaged acceleration results of the trimmed subsystems and the averaged sound pressure levels over the cavity subsystems were compared between measurements, modal frequency response and Virtual SEA simulations in the same load cases. Based on the result of the BIB configuration, frequency dependent damping was applied for the structure in Virtual SEA. In general, the correlation of the results was satisfactory for such a complex simulation model. Moderate overestimations can be observed in load case 24 and 34 in the Virtual SEA results, which might be the result of the simplified layer structure of one particular trim part, the rear seats. Overall, this section showed that the Virtual SEA approach is capable of full vehicle trimmed body simulations with great accuracy, even

compared to finite element method. The validation involved the fluid-structure coupling through the SmEdA approach and the analytical equivalent transfer admittance method for considering the effect of the trim parts.

7.7. Thesis 3

I proved that Virtual SEA is capable of performing industrial-scaled, full vehicle trimmed body acoustic simulations in the mid-frequency range, with prediction accuracy comparable to finite element method, using:

- SmEdA approach, for the structure-fluid coupling,
- analytical equivalent transfer admittance method, for considering the damping, absorption, and insulation effect of multilayered, trim parts containing poro-elastic materials.

As such, I proved that Virtual SEA provides transition of the low frequency finite element models to the mid- and high frequency range [V].

8. REDUCTION OF PANEL VIBRATION VIA THE OPTIMIZATION OF DAMPING PAD DISTRIBUTION

The noise inside the passenger compartment of a vehicle can be reduced depending on its source and frequency range. Damping pads with sufficient mass and high damping coefficient can be efficiently applied to reduce the vibrations of large panels that contribute to the structure-born interior noise. Several works can be found in literature that discuss the topic of finding the optimal distribution of damping pads, but those are wasteful of resources, and complicated to use. In this Chapter, a new and user-friendly methodology is proposed to identify the areas with the highest modal activity on the structure, which enables to find the optimal distribution of damping layers for a given frequency range. Its advantage is that it is not necessary to perform extra calculations, as the results that the method relies on are available during a complete Virtual SEA simulation process. The effectiveness of this methodology is presented on a real vehicle model in Body-in-White (BIW) configuration.

8.1. Simulation methodology

The proposed method is specifically based on the Virtual SEA module in MSC Actran. In the first step of the solution sequence of such analysis, a reduced energy model is built by assembling distribution matrices according to Equation (30) and Equation (31). MSC Actran is able to compute local responses during a Virtual SEA simulation by computing an auxiliary scalar output field $\alpha(x)$, on each subsystem during the build distribution matrices sequence. This distributes the energy of a subsystem across its nodes. This output field $\alpha(x)$ is proportional to the average of the resonant modes at node x (eigenvectors) in each frequency band and is normalized, so the energy of the subsystem can be retrieved by integrating over local results of the subsystem. For any given output node x, squared velocity or squared pressure results can be retrieved by scaling the subsystem energy E by the $\alpha(x)$, evaluated at node x. This is expressed in Equation (61), where $\boldsymbol{X}$ denotes the subsystem containing node x [81].

$$Nodal\ response(x) \propto \alpha(x) * E(\boldsymbol{X}),\ x \in \boldsymbol{X} \tag{61}$$

By plotting this scalar field, the optimal positions of the damping pads for a given frequency range can be easily determined, because it shows exactly where to expect high local responses. No extra calculations are necessary, since the computation sequence is part of the Virtual SEA simulation that requires the calculation of the modes, mass, and stiffness matrices.

8.2. Simulation model setup

The optimization of damping pad distribution was performed on the same 2015 Audi A3 Limousine car model that was used in the previous chapter, but in a less complex, BIW configuration, shown in Figure 66. This model consists of about 560 000 linear elements and 550 000 nodes. The first setup is a bare model without damping pads to identify those areas on the floor panel on which applying damping pads would be effective. The second setup uses the original damping pad layout by the manufacturer and the third one is a weight-optimized model. The original layout of the damping pads is shown in Figure 67. The damping pads are made of bitumen material, whose properties are summarized in Table 7. The total mass of the damping layers in the original setup is 3.98 kg and the covered area is 0.78 m^2.

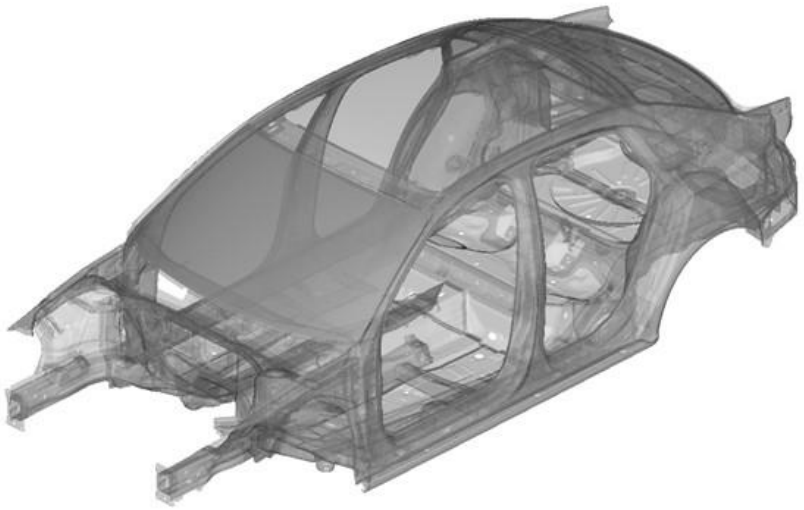

Figure 66. Finite element model of the car structure.

Table 7. Material properties of bitumen damping layers.

Young's modulus	400 MPa
Poisson ratio	0.27
Density	1.967-2.596 kg/m^3

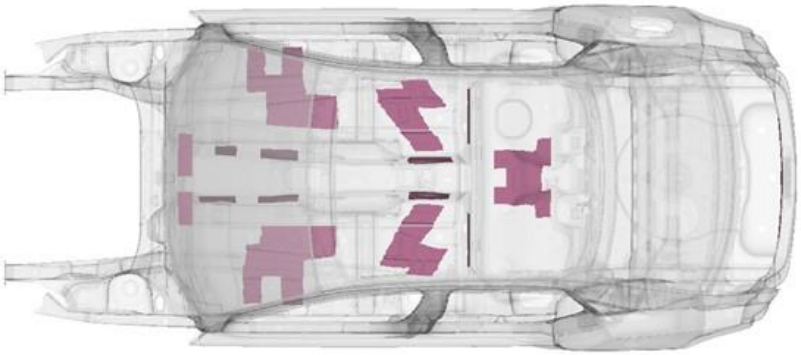

Figure 67. Original damping pad layout by manufacturer.

To compare the effect of the different layouts, a full Virtual SEA simulation is performed, and the mean squared velocity of the floor panel subsystem is compared for each setup due to a unit point force excitation in two load cases. The modal database for the simulation was extracted up to 560 Hz. The Virtual SEA models of each setup were built up with 1% constant damping defined for the entire vehicle structure in each case, 36.6% damping defined for the bitumen layers in the second (original model) and third (optimized model) setup. The partitioning of the Virtual SEA model is shown in Figure 68.

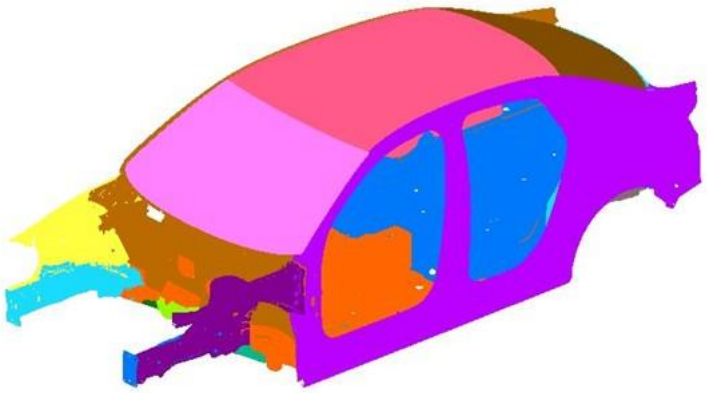

Figure 68. SEA subsystems of the vehicle.

8.3. Simulation results

Figure 69 shows the results of setup number one, without damping pads. The scalar field α that is used to calculate local responses at a later stage of a Virtual SEA simulation is shown on the floor panel. In those areas, where α takes high values, high local responses are expected, and

these are easy to identify. It can be observed in Figure 70, showing the original damping pad layout and the results of the bare configuration, that most of these areas are covered by bitumen layers. However, according to the results, there are also some areas where α takes low values but covered by bitumen layers, which seems to be unnecessary and could be removed. Figure 71 shows the new weight-optimized layout where the damping pads were removed from these areas. Compared to the original setup where the total mass of the damping pads was 3.98 kg, the new setup weighs only 2.68 kg, meaning about 33% mass reduction. In terms of coverage, the total surface covered by the damping pads in the optimized layout has dropped from 0.78 m^2 to 0.548 m^2, corresponding to about 30% decrease.

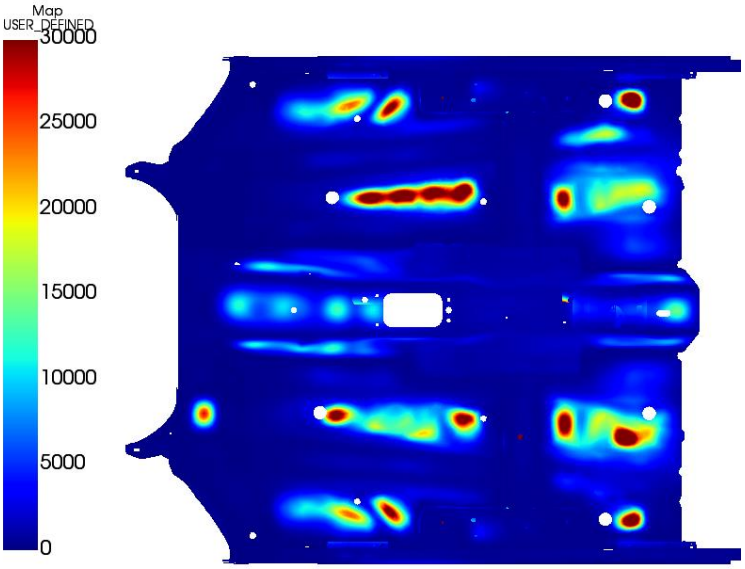

Figure 69. Field alpha of the bare floor model.

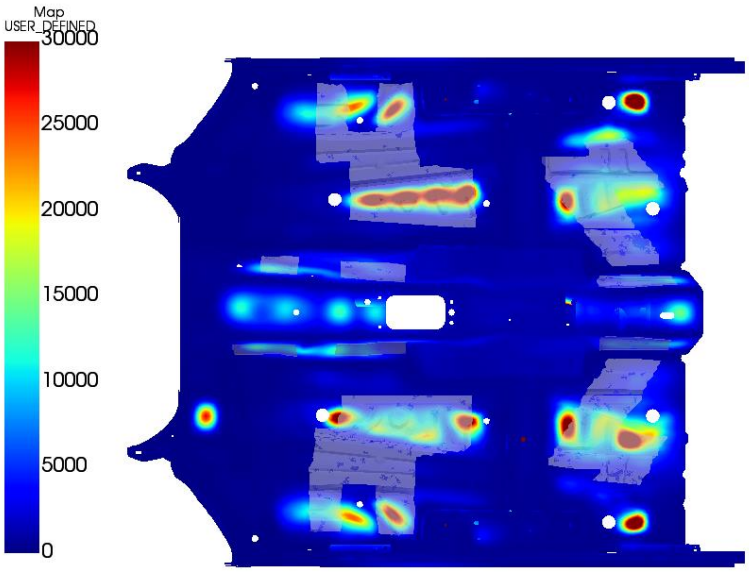

Figure 70. Original damping pad layout on the bare model results.

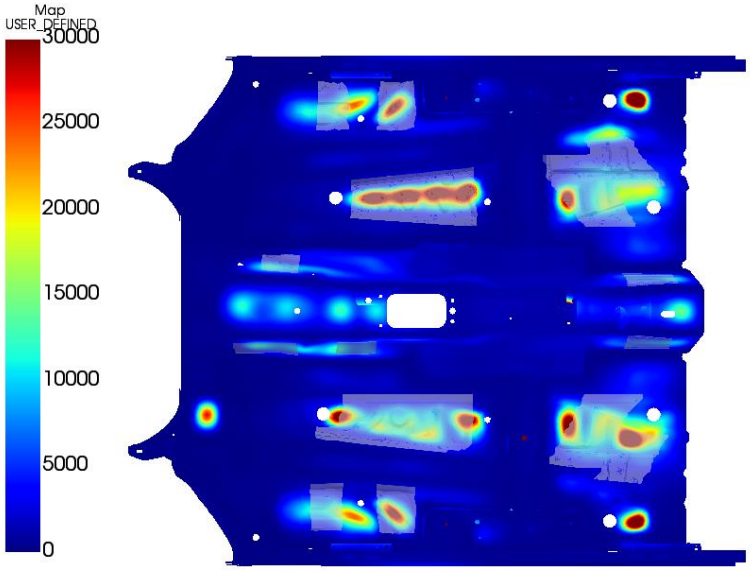

Figure 71. Optimized damping pad layout on the bare model results.

To compare the results of the original and the optimized setups, the mean velocity of the floor panel was investigated in a Virtual SEA simulation. A unit point force excitation was applied in two load cases. The locations of the excitations are shown in Figure 72.

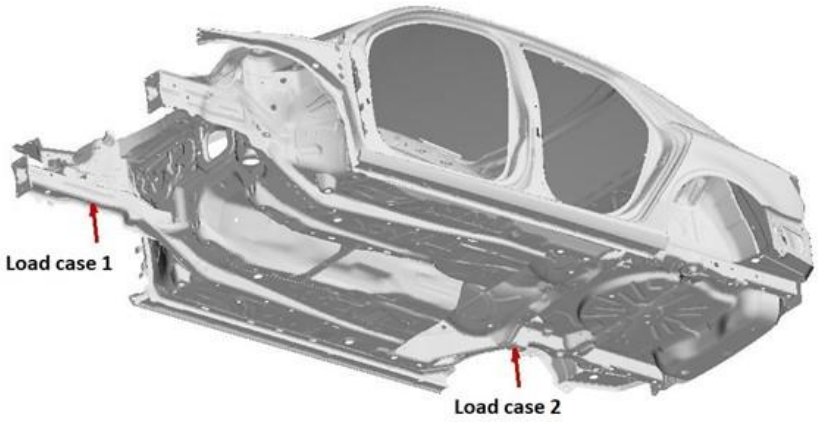

Figure 72. Excitation load cases.

Figure 73 shows the mean velocity of the floor panel of the three setups in load case one, where the excitation was applied on the front right frame rail, and Figure 74 shows the same results for excitation on the rear right suspension mount. It can be observed that starting from 100 Hz, the effect of the damping pads becomes significant. The mean velocity of the floor panel is about 1-1.5 dB lower in the two setups, where damping pads were used compared to the bare model. The difference between the original and the optimized setup is negligible. These curves suggest that similar performance as the original setup can be achieved with the optimized model, with 33% less weight of the damping pads.

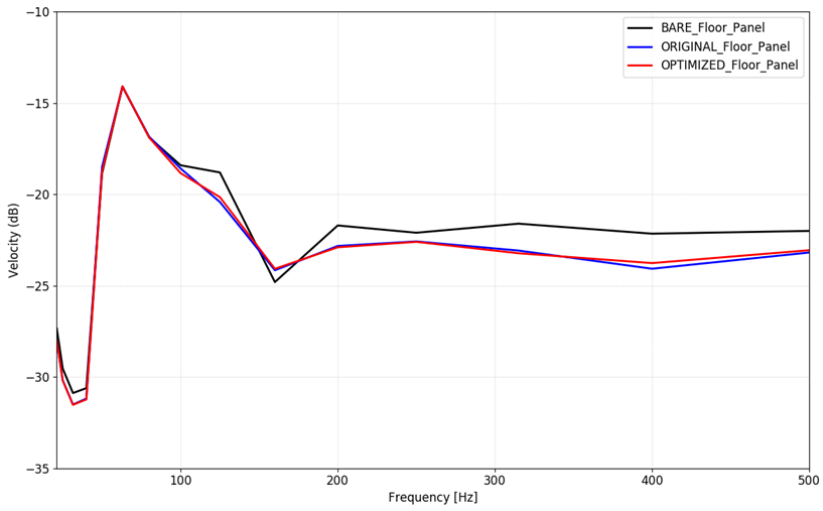

Figure 73. Mean velocity of the floor panel in three setups in load case 1.

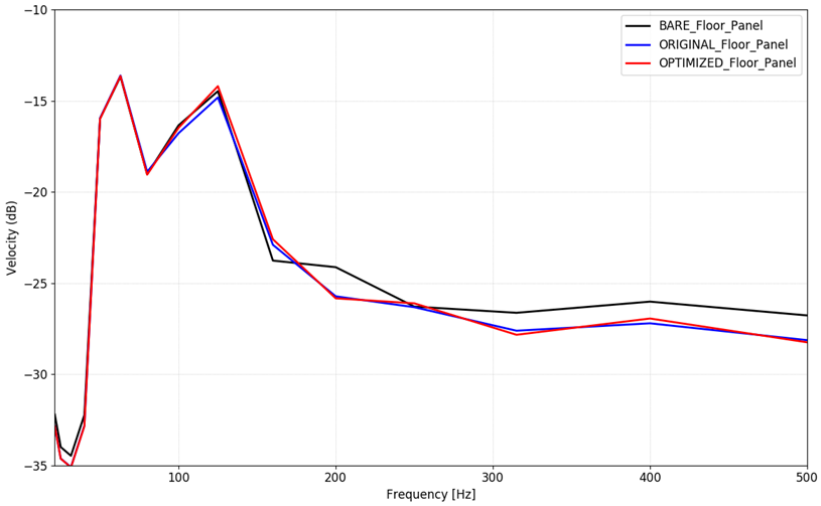

Figure 74. Mean velocity of the floor panel in three setups in load case 2.

8.4. Summary and conclusions

Is this Chapter, a novel methodology was proposed to find the optimal location of damping pads on vehicle chassis, where the modal activity is the highest. The methodology relies on the scaling factor of subsystem energy levels that is used to retrieve local responses in MSC Actran. As part of a complete Virtual SEA solution, this approach allows acoustic developers to determine the optimal damping pad distribution on a structure for a given frequency range with minimal additional effort and computational cost. The effectiveness of the method was presented by comparing the original and the optimized damping pad layout on a Body-in-White car structure. A complete analysis of one model took approximately 2 hours 40 mins including the modal extraction up to 560 Hz, providing the results for the optimization and the velocity results in the two load cases. It was shown that with the optimized layout, similar NVH performance can be achieved on the floor panel of the car structure as with the original setup, but with 33% less weight. This might aid to increase the efficiency of high-volume production of vehicles, as well as to optimize the damping layer mass for higher category models.

8.5. Thesis 4

I formulated a novel methodology to determine the optimal location of damping pads on a vehicle chassis structure for a given frequency range. The methodology relies on the scaling factor of subsystem energy levels that distributes subsystem energies along the finite element nodes to retrieve local responses in MSC Actran's Virtual SEA module. I proved that this method enables to reduce to overall weight and coverage of damping layers on the vehicle chassis while preserving its NVH performance. An additional advantage is that the required

scalar field is calculated during a Virtual SEA simulation, which means that the proposed method adds no extra computational cost to the overall solution [III].

9. ASSESSMENT OF GOALS AND OUTLOOK

The main goal of the present work was to enable the Virtual SEA approach to cover the mid- and high frequency vibro-acoustic simulations. Former studies already showed some of its key features that make it more effective than conventional simulation methods in certain cases. However, the present work provides original contributions in achieving the goals that were defined in Chapter 3. First, it was shown that Virtual SEA is able to consider distinct types of junctions through the finite element representation of the connection, unlike analytical SEA. Various connection types were investigated by experimental and virtual power injection method and the results showed satisfactory agreement. The influence of the finite element modeling parameters was explored in a DOE, and the key factors, such as the thickness ratio of the connecting plates were identified with the help of response surfaces. Next, the validity of different SEA subdivisions was investigated. It was proven that clustering methods lead to the best possible SEA models, thus providing better accuracy results than models built up based on intuition. In relation to this, a novel methodology was proposed that allows the comparison of different subdivisions. From several clustering techniques evaluated, the subsystem generation algorithm built into MSC Actran was proven to be the most effective method that facilitates reasonable and consistent model building and also saves resources. The following step of the enabling process was to create the vibro-acoustic Virtual SEA model of a full-scale, trimmed body vehicle. In this model, the fluid-structure coupling was realized by the SmEdA approach, and the effects of the trim bodies were considered by updating the affected damping and coupling loss factors, according to the analytical equivalent transfer admittance method. The results presented in Chapter 7.5 confirm that Virtual SEA can be used for vehicle trimmed body simulations, with significantly less computational costs than finite element and reduced impedance methods. Consequently, Virtual SEA provides the transition of the low frequency finite element models to the mid- and high frequency range. The last goal of the present work was to investigate how the energetic quantities computed during a Virtual SEA simulation can be used for optimization. It was found that the scalar field that distributes the subsystem energies between the subsystem nodes is proportional to the modal activity, thus it can be used to find the optimal distribution of damping layers on a vehicle chassis. The proposed method helped to save about 33% of the damping material used on the floor panel of a vehicle model while preserving the NVH performance. Furthermore, this was achieved by effectively no additional computation costs since the calculation of the scaling factor is part of a complete Virtual SEA simulation.

Future work could include the validation of other junction types that this work did not cover, such as bolted, riveted connections, in various angles, etc. For each junction type, a similar design of experiment could be used for exploring the effects of individual modeling parameters. Regarding the full vehicle simulations, the use of the automatic subsystem generation could result in even more accurate results. Once the placement of trim parts is considered during the subsystem generation, it can be used for trimmed body simulations as well. One could also explore the possibilities that other data mining methods such as Proper Orthogonal Decomposition (PDO), Machine Learning (ML), Artificial Intelligence (AI), etc. could offer to reduce the computational costs or improve the results of the subsystem generation process. Further studies could investigate how the presence of trim parts alters the extended solution of Virtual SEA, which would also require high-frequency measurements for the validations. The modeling method of the more complex-shaped trim bodies that cannot be described as a multilayered composite material needs to be worked out. One drawback of the Virtual SEA method is that the modal base needs to be recalculated for every single change in the model. Solving this could help the method to spread more quickly in the vehicle industry, where design cycles can be quite frequent. The present work showed that the Virtual SEA method has immense potential to cover the mid- and high frequency range for full vehicle trimmed body acoustic simulations.

10.SUMMARY OF NEW SCIENTIFIC RESULTS

10.1. Thesis 1

I proved that the damping and coupling effects of various junction types can be accurately considered in Virtual SEA through the proper finite element representation of the connection. The most common junction types that can be found on a vehicle chassis structure have been validated by comparing experimental and virtual power injection method results for set of coupled plates. The effects of the finite element connection modeling parameters have been explored in a Design of Experiment, and I proved that the most influential ones are the geometrical properties, in particular, the thickness ratio of the connecting plates. The changes in the connecting element stiffness and the diameter of the connection point have less influence on the Virtual PIM results [II].

10.2. Thesis 2

I formulated a novel procedure to compare different subsystem divisions for the Virtual SEA approach. Based on this procedure, I proved that clustering algorithms are able to provide subsystem divisions that comply more with the assumptions of the SEA theory than the user-defined subsystems. The automatic subsystem generation feature implemented in MSC Actran has been proven to be superior to other clustering methods. I proved that ultimately, clustering-based subsystems lead to more accurate Virtual SEA models to be created in a more reasonable and consistent way, with less time spent on model building [I].

10.3. Thesis 3

I proved that Virtual SEA is capable of performing industrial-scaled, full vehicle trimmed body acoustic simulations in the mid-frequency range, with prediction accuracy comparable to finite element method, using:

- SmEdA approach, for the structure-fluid coupling,
- analytical equivalent transfer admittance method, for considering the damping, absorption, and insulation effect of multilayered, trim parts containing poro-elastic materials.

As such, I proved that Virtual SEA provides transition of the low frequency finite element models to the mid- and high frequency range [V].

10.4. Thesis 4

I formulated a novel methodology to determine the optimal location of damping pads on a vehicle chassis structure for a given frequency range. The methodology relies on the scaling factor of subsystem energy levels that distributes subsystem energies along the finite element nodes to retrieve local responses in MSC Actran's Virtual SEA module. I proved that this method enables to reduce to overall weight and coverage of damping layers on the vehicle chassis while preserving its NVH performance. An additional advantage is that the required scalar field is calculated during a Virtual SEA simulation, which means that the proposed method adds no extra computational cost to the overall solution [III].

PUBLICATIONS BY THE AUTHOR

[I] Sipos, D., Feszty, D., "Comparison of clustering based Virtual SEA subsystem generation models", Journal of Theoretical and Computational Acoustics, accepted for publication in March 2023.

[II] Sipos, D., Treszkai, M. F., and Feszty, D., "Validation of finite element connection modeling by comparison of experimental and virtual power injection methods" Journal of Vibroengineering, Vol. 25, No. 1, Oct. 2022
DOI: https://doi.org/10.21595/jve.2022.22754

[III] Sipos, D., Treszkai, M. F., Feszty, D., "Optimization of damping pad distribution on body-in-white car structure", Journal of Vibroengineering, Vol. 24, Issue 2, 2022, p. 386-393.
DOI: https://doi.org/10.21595/jve.2021.22158

[IV] Sipos, D., Treszkai, M. F., and Feszty, D., "Welding distortion generated uncertainties in the vibrational behavior of a ladder-like structure" INTER-NOISE and NOISE-CON Congress and Conference Proceedings. Vol. 263. No. 2. Institute of Noise Control Engineering, 2021.
DOI: https://doi.org/10.3397/IN-2021-2844

[V] Sipos, D., Brandstetter, M., Guellec, A., Jacqmot, J., and Feszty, D., "Extended Solution of a Trimmed Vehicle Finite Element Model in the Mid-Frequency Range", SAE Technical Paper 2020-01-1549, 2020
DOI: https://doi.org/10.4271/2020-01-1549.

[VI] Treszkai, M. F., Sipos, D., and Feszty, D., "Damping determination by half-power bandwidth method for a slightly damped rectangular steel plate in the mid-frequency range" Acta Technica Jaurinensis 13.3 (2020): 177-196.
DOI: https://doi.org/10.14513/actatechjaur.v13.n3.545

[VII] Sipos, D., Feszty, D., "Development of a procedure for the validation of statistical energy analysis simulations" Acta Technica Jaurinensis 12.4 (2019): 335-346.
DOI: https://doi.org/10.14513/actatechjaur.v12.n4.512

[VIII] Sipos, D., Feszty D., Vehovszky, B., "The effect of the Biot-parameters on the dynamic and acoustic response of a vehicle", in: Advanced Manufacturing and Repair Technologies in Vehicle Industry: Monograph 35th international colloquium, Zielona Góra, Poland: University of Zielona Góra, Faculty of Mechanical Engineering (2018) 394 p. pp. 299-308.

REFERENCES

[1] Audi AG. "The New Audi A8, Multimaterial Audi space frame A172348" Audi Mediacenter, 05 April 2017. Downloaded: 25 February 2023 https://www.audi-mediacenter.com/en/photos/album/leightweight-construction-240

[2] Audi AG. "The New Audi A8, Joining methods A172352" Audi Mediacenter, 05 April 2017. Downloaded: 25 February 2023 https://www.audi-mediacenter.com/en/photos/album/leightweight-construction-240

[3] Nefske, D. J., and Sung, S. H. "Automobile interior noise prediction using a coupled structural-acoustic finite element model." Proceeding of the 11th International Congress on Acoustics. Paris, France. Vol. 5. 1983

[4] Sung, S. H., and Nefske, D. J. "A Coupled Structural-Acoustic Finite Element Model for Vehicle Interior Noise Analysis." ASME. J. Vib., Acoust., Stress, and Reliab. April 1984, 106(2): 314–318. DOI: https://doi.org/10.1115/1.3269187

[5] Sung, S. H., Nefske, D. J., and Bonarens, F. "Development and experimental evaluation of a vehicle structural-acoustic trimmed-body model." No. 1999-01-1798. SAE Technical Paper, 1999 DOI: https://doi.org/10.4271/1999-01-1798

[6] Sol, A., and Van Herpe, F. "Numerical prediction of a whole car vibro-acoustic behavior at low frequencies." No. 2001-01-1521. SAE Technical Paper, 2001 DOI: https://doi.org/10.4271/2001-01-1521

[7] Yuksel, E., Kamci, G., and Basdogan, I. "Vibro-acoustic analysis of a vehicle integrated with design of experiments methodology using three performance criteria." In Proceedings of 20th International Congress on Acoustics, ICA 2010, Sdyney, Australia, 2010

[8] Song, C. K., Hwang, J. K., Lee, J. M., and Hedrick, J. K. "Active vibration control for structural–acoustic coupling system of a 3-D vehicle cabin model." Journal of Sound and Vibration, 267(4), 851-865. 2003 DOI: https://doi.org/10.1016/S0022-460X(02)01553-5

[9] Kim, S. H., Lee, J. M., and Sung, M. H. "Structural-acoustic modal coupling analysis and application to noise reduction in a vehicle passenger compartment." Journal of Sound and Vibration, 225(5), 989–999. 1999 DOI: https://doi.org/10.1006/jsvi.1999.2217

[10] Panneton, R., and Atalla, N. "An efficient finite element scheme for solving the three-dimensional poroelasticity problem in acoustics." The Journal of the Acoustical Society of America, 101(6), 3287-3298. 1997
DOI: https://doi.org/10.1121/1.418345

[11] Atalla, N., Panneton, R., and Debergue, P. "A mixed displacement-pressure formulation for poroelastic materials." The Journal of the Acoustical Society of America, 104(3), 1444-1452. 1998
DOI: https://doi.org/10.1121/1.424355

[12] Allard, J. F., and Attala, N. "Propagation of Sound in Porous Media." Second Edition, John Wiley and Sons Publication, Chichester, United Kingdom, 372, 2009.

[13] Dazel, O. "Numerical methods for the Biot theory in acoustics." Habilitation thesis, Uniersity of Maine–Le Mans, Laboratoire d'Acoustique, 2011.

[14] Deckers, E., Jonckheere, S., Vandepitte, D., and Desmet, W. "Modelling techniques for vibro-acoustic dynamics of poroelastic materials." Archives of Computational Methods in Engineering, 22(2), 183-236. 2015
DOI: https://doi.org/10.1007/s11831-014-9121-0

[15] Blanchet, D., Anciant, M., and Mebarek, L. "Modeling the Vibro-Acoustic Effect of Trim on Full Vehicle and Component Level Analysis." DAGA, Rotterdam, The Netherlands, 2009

[16] Caillet, A., Guellec, A., Blanchet, D., and Roy, T. "Prediction of Structureborne Noise in a Fully Trimmed Vehicle Using Poroelastic Finite Elements Method (PEM)," No. 2014-01-2083. SAE Technical Paper, 2014
DOI: https://doi.org/10.4271/2014-01-2083

[17] Yoo, J. W., Brandstetter, M., Jeong, C., Jacqmot, J., and Chae, K. S. "Extensive Correlation Study of Acoustic Trim Packages in Trimmed Body Modeling of an Automotive Vehicle." No. 2019-01-1511. SAE Technical Paper, 2019
DOI: https://doi.org/10.4271/2019-01-1511

[18] Lyon, R. H., and Maidanik, G. "Power flow between linearly coupled oscillators." The journal of the Acoustical Society of America," 34(5), 623-639. 1962
DOI: https://doi.org/10.1121/1.1918177

[19] Smith Jr, P. W. "Response and radiation of structural modes excited by sound." The Journal of the Acoustical Society of America, 34(5), 640-647. 1962
DOI: https://doi.org/10.1121/1.1918178

[20] Steel, J. A. "The prediction of structural vibration transmission through a motor vehicle using statistical energy analysis." Journal of sound and vibration, 193(3), 691-703. 1996
DOI: https://doi.org/10.1006/jsvi.1996.0308

[21] Galasso, A., Di Somma, G., D'Esposito, F., De Rosa, S., and Franco, F. "SEA car structural and acoustic modelling." The Shock and Vibration Digest, 38(5), 435-436. 2006

[22] Musser, C. T., Manning, J. E., and Peng, G. C. "Predicting vehicle interior sound with statistical energy analysis." Sound & Vibration, 46(12), 8-14. 2012

[23] Chen, X., Wang, D., and Ma, Z. "Simulation on a car interior aerodynamic noise control based on statistical energy analysis." Chinese Journal of Mechanical Engineering, 25(5), 1016-1021. 2012
DOI: https://doi.org/10.3901/CJME.2012.05.1016

[24] Bötke, A., Erensoy, E., and Sevginer, C. "Modeling and Validation Processes of an Electric Vehicle with Statistical Energy Analysis." In Euronoise, pp. 1417-1422. 2015, ISSN 2226-5147

[25] Jang, J. S., Kuk, J. Y., Park, J. C., Hadjit, R., Dande, H., and Frank, E. "SEA Modeling and Validation of a Truck Cab for Sound Package Optimization." In Proceedings of InterNOISE, 2015

[26] Shorter, P. J., and Langley, R. S. "Vibro-acoustic analysis of complex systems." Journal of Sound and Vibration, 288(3), 669-699. 2005
DOI https://doi.org/10.1016/j.jsv.2005.07.010

[27] Langley, R. S., and Cotoni, V. "Response variance prediction for uncertain vibro-acoustic systems using a hybrid deterministic-statistical method." The Journal of the Acoustical Society of America, 122(6), 3445-3463. 2007
DOI: https://doi.org/10.1121/1.2799499

[28] Hills, E., Mace, B. R., and Ferguson, N. S. "Acoustic response variability in automotive vehicles." Journal of Sound and Vibration, 321(1-2), 286-304. 2009
DOI: https://doi.org/10.1016/j.jsv.2008.09.029

[29] Kompella, M. S., and Bernhard, R. J. "Measurement of the statistical variation of structural-acoustic characteristics of automotive vehicles." No. 931272. SAE Technical Paper, 1993
DOI: https://doi.org/10.4271/931272

[30] Charpentier, A., Sreedhar, P., and Fukui, K. "Using the hybrid FE-SEA method to predict structure-borne noise transmission in a trimmed automotive vehicle." No. 2007-01-218. SAE Technical Paper, 2007
DOI: https://doi.org/10.4271/2007-01-2181

[31] Charpentier, A., Sreedhar, P., Cordioli, J., and Fukui, K. "Modeling process and validation of Hybrid FE-SEA method to structure-borne noise paths in a trimmed automotive vehicle." No. 2008-36-0574. SAE Technical Paper, 2008
DOI: https://doi.org/10.4271/2008-36-0574

[32] Prasanth, S., Charpentier, A., and Fukui, K. "Using the Hybrid FE-SEA model of a trimmed full vehicle to reduce structure borne noise from 200Hz to 1kHz." No. 2011-26-0020. SAE Technical Paper, 2011
DOI: https://doi.org/10.4271/2011-26-0020

[33] Prasanth, S., and Shreedhar, P. "Modeling process and validation of Hybrid FE-SEA method to structure-borne noise paths in a trimmed automotive vehicle." International Journal of Research in Aeronautical and Mechanical Engineering, 1(3), 17-28. 2013

[34] Chen, S. M., Wang, D. F., and Zan, J. M. "Interior noise prediction of the automobile based on hybrid FE-SEA method." in Mathematical Problems in Engineering, Hindawi Publishing Corporation, 2011
DOI: https://doi.org/10.1155/2011/327170

[35] Musser, C. T., and Rodrigues, A. B. "Mid-frequency prediction accuracy improvement for fully trimmed vehicle using hybrid SEA-FEA technique." No. 2008-36-0564. SAE Technical Paper, 2008
DOI: https://doi.org/10.4271/2008-36-0564

[36] Langley, R. S., and Heron, K. 1. "Elastic wave transmission through plate/beam junctions." Journal of sound and vibration, 143(2), 241-253. 1990
DOI: https://doi.org/10.1016/0022-460X(90)90953-W

[37] Langley, R. S. "A derivation of the coupling loss factors used in statistical energy analysis." Journal of Sound and Vibration, 141(2), 207-219. 1990
DOI: https://doi.org/10.1016/0022-460X(90)90835-N

[38] Fahy, F. J., and James, P. P. "A study of the kinetic energy impulse response as an indicator of the strength of coupling between SEA subsystems." Journal of Sound and Vibration, 190(3), 363-386. 1996
DOI: https://doi.org/10.1006/jsvi.1996.0069

[39] Le Bot, A., and Cotoni, V. "Validity diagrams of statistical energy analysis." Journal of sound and vibration, 329(2), 221-235. 2010
DOI: https://doi.org/10.1016/j.jsv.2009.09.008

[40] Bosmans, I., Mees, P., and Vermeir, G. "Structure-borne sound transmission between thin orthotropic plates: analytical solutions." Journal of sound and vibration, 191(1), 75-90. 1996
DOI: https://doi.org/10.1006/jsvi.1996.0107

[41] Wester, E. C. N., and Mace, B. R. "Statistical energy analysis of two edge-coupled rectangular plates: ensemble averages." Journal of Sound and Vibration, 193(4), 793-822. 1996
DOI: https://doi.org/10.1006/jsvi.1996.0316

[42] Wöhle, W., Beckmann, T., and Schreckenbach, H. "Coupling loss factors for statistical energy analysis of sound transmission at rectangular structural slab joints, part I." Journal of Sound and Vibration, 77(3), 323-334. 1981
DOI: https://doi.org/10.1016/S0022-460X(81)80169-1

[43] Wöhle, W., Beckmann, T., and Schreckenbach, H. "Coupling loss factors for statistical energy analysis of sound transmission at rectangular structural slab joints, part II." Journal of Sound and Vibration, 77(3), 335-344. 1981
DOI: https://doi.org/10.1016/S0022-460X(81)80170-8

[44] Díaz-Cereceda, C., Poblet-Puig, J., and Rodríguez-Ferran, A. "Numerical estimation of coupling loss factors in building acoustics." Journal of Sound and Vibration, 332(21), 5433-5450. 2013
DOI: https://doi.org/10.1016/j.jsv.2013.05.012

[45] Patil, V. H., and Manik, D. N. "Sensitivity analysis of a two-plate coupled system in the statistical energy analysis (SEA) framework." Structural and Multidisciplinary Optimization, 59(1), 201-228. 2019
DOI: https://doi.org/10.1007/s00158-018-2061-9

[46] Simmons, C. "Structure-borne sound transmission through plate junctions and estimates of SEA coupling loss factors using the finite element method." Journal of sound and vibration, 144(2), 215-227. 1991
DOI: https://doi.org/10.1016/0022-460X(91)90745-6

[47] De Langhe, K., "High frequency vibrations: contributions to experimental and computational SEA parameter identification techniques." PhD thesis, Katholieke Universiteit Leuven, Department of Mechanical Engineering, Leuven, Belgium, 1996.

[48] Bies, D., and Hamid, S. "In situ determination of loss and coupling loss factors by the power injection method." Journal of Sound and Vibration, 70(2), 187-204. 1980
DOI: https://doi.org/10.1016/0022-460X(80)90595-7

[49] James, P. P., and Fahy, F. J. "A technique for the assessment of strength of coupling between SEA subsystems: experiments with two coupled plates and two coupled rooms." Journal of sound and vibration, 203(2), 265-282. 1997
DOI: https://doi.org/10.1006/jsvi.1996.0871

[50] Bouhaj, M., Von Estorff, O., and Peiffer, A. "An approach for the assessment of the statistical aspects of the SEA coupling loss factors and the vibrational energy transmission in complex aircraft structures: Experimental investigation and methods benchmark." Journal of Sound and Vibration, 403, 152-172. 2017
DOI: https://doi.org/10.1016/j.jsv.2017.05.028

[51] Gu, J., and Sheng, M. "Improved energy ratio method to estimate coupling loss factors for series coupled structure." Journal of Mechanical Engineering, 45(1), 37-40. 2015
DOI: https://doi.org/10.3329/jme.v45i1.24382

[52] Hela Ladin, H. B., Tsujiuchi, N., and Koizumi, T. "Loss factors estimation of statistical energy analysis using power injection method." The Science and Engineering Review of Doshisha University, 55(3), 291-300. 2014
DOI: https://doi.org/10.14988/pa.2017.0000013821

[53] Bhagwan, M. M., and Popuri, B. "Estimation of coupling loss factors for rectangular plates with different materials and junctions." Noise & Vibration Worldwide, 50(9-11), 306-312. 2019
DOI: https://doi.org/10.1177/0957456519883264

[54] Panuszka, R., Wiciak, J., and Iwaniec, M. "Experimental assessment of coupling loss factors of thin rectangular plates." Archives of Acoustics, 30(4), 533-551. 2005

[55] Kurosawa, Y. "Predicting automotive interior noise including wind noise by statistical energy analysis." International Journal of Mechanical and Mechatronics Engineering, 10(3), 635-641. 2017
DOI: https://doi.org/10.5281/zenodo.1132056

[56] Treszkai, M. F., Peiffer, A., and Feszty, D. "Power Injection Method-based evaluation of the effect of binding technique on the Coupling Loss Factors and Damping Loss Factors in Statistical Energy Anal-ysis simulations." Manufacturing Technology, 21(4), 544-558. 2021
DOI: https://doi.org/10.21062/mft.2021.065

[57] Gagliardini, L., Houillon, L., Petrinelli, L., and Borello, G. "Virtual SEA: mid-frequency structure-borne noise modeling based on Finite Element Analysis." No. 2003-01-1555. SAE Technical Paper, 2003
DOI: https://doi.org/10.4271/2003-01-1555

[58] Gagliardini, L., Houillon, L., Borello, G., and Petrinelli, L. "Virtual SEA-FEA-based modeling of mid-frequency structure-borne noise." Sound and vibration, 39(1), 22. 2005

[59] Borello, G., and Gagliardini, L. "Virtual SEA: towards an industrial process." No. 2007-01-2302. SEA Technical Paper, 2007
DOI: https://doi.org/10.4271/2007-01-2302

[60] Brandstetter, M., Dutrion, C., Antoniadis, P. D., Mordillat, P., and Van den Nieuwenhof, B. "SEA Modelling and Transfer Path Analysis of an Extensive RENAULT B segment SUV Finite Element Model." In Aachen Acoustic Colloquium, 2018

[61] Duval, A., Dejaeger, L., Morgenstern, C., and Rondeau, J. F. Novel technique for the introduction of curved trims in SEA/Virtual SEA models using poroelastic finite elements in the middle (and high) frequency range." Congrès SIA Confort automobile et ferroviaire, Le Mans, France, 2010

[62] Magrans, F. X., Poblet-Puig, J., and Rodríguez-Ferran, A. "A subsystem identification method based on the path concept with coupling strength estimation." Mechanical Systems and Signal Processing, 100, 588-604. 2018
DOI: https://doi.org/10.1016/j.ymssp.2017.07.043

[63] Totaro, N., and Guyader, J. L. "SEA substructuring using cluster analysis: The MIR index." Journal of Sound and Vibration, 290(1-2), 264-289. 2006
DOI: https://doi.org/10.1016/j.jsv.2005.03.030

[64] Kovalevsky, L., and Langley, R. S. "Automatic recognition of the components of a hybrid FE-SEA model." In INTER-NOISE and NOISE-CON Congress and Conference Proceedings, 244(1), 336-346. Institute of Noise Control Engineering, 2012.

[65] Díaz-Cereceda, C., Poblet-Puig, J., and Rodríguez-Ferran, A. "Automatic subsystem identification in statistical energy analysis." Mechanical Systems and Signal Processing, 54, 182-194. 2015
DOI: https://doi.org/10.1016/j.ymssp.2014.09.003

[66] Kassem, M., Soize, C., and Gagliardini, L. "Structural partitioning of complex structures in the medium-frequency range. An application to an automotive vehicle." Journal of Sound and vibration, 330(5), 937-946. 2011
DOI: https://doi.org/10.1016/j.jsv.2010.09.008

[67] Kassem, M., Soize, C., and Gagliardini, L. "Energy-density field approach for low-and medium-frequency vibroacoustic analysis of complex structures using a statistical computational model." Journal of sound and vibration, 323(3-5), 849-863. 2009
DOI: https://doi.org/10.1016/j.jsv.2009.01.014

[68] Wodtke, H. W., and Lamancusa, J. S. "Sound power minimization of circular plates through damping layer placement." Journal of Sound and vibration, 215(5), 1145-1163. 1998
DOI: https://doi.org/10.1006/jsvi.1998.1660

[69] Arenas, J. P., and Hornig, K. H. "Sound power radiated from rectangular plates with unconstrained damping layers." In Proceedings of the 9th International Conference on Computational Structures Technology, Stirlingshire, Scotland. 2008
DOI: http://dx.doi.org/10.4203/ccp.88.83

[70] Subramanian, S., Surampudi, R., Thomson, K. R., and Vallurupalli, S. "Optimization of damping treatments for structure borne noise reductions." Sound and vibration, 38(9), 14-19. 2004
DOI: http://dx.doi.org/10.4271/2003-01-1592

[71] Balmes, E., and Germes, S. "Design strategies for viscoelastic damping treatment applied to automotive components." IMAC, Dearborn. 2004

[72] Furukava, M., Gerges, S., Neves, M. M., and Coelho, B. J. "Analysis of structural damping performance in passenger vehicles chasis." The Journal of the Acoustical Society of America 126(4), 22-80. 2009
DOI: http://dx.doi.org/10.1121/1.3249345

[73] Comesana, D. F., and Tatlow, J. "Designing the damping treatment of a vehicle body based on scanning particle velocity measurements." In American Control Conference. 2018

[74] Hara, D., and Özgen, G. O. "Investigation of weight reduction of automotive body structures with the use of sandwich materials." Transportation research procedia, 14, 1013-1020. 2016
DOI: https://doi.org/10.1016/j.trpro.2016.05.081

[75] Guellec, A., Cabrol, M., Jacqmot, J., and Van den Nieuwenhof, B. "Optimization of trim component and reduction of the road noise transmission based on finite element methods." No. 2018-01-1547. SAE Technical Paper, 2018
DOI: https://doi.org/10.4271/2018-01-1547

[76] MSC Nastran 2021.4 Dynamic Analysis User's Guide, Hexagon AB, 2021

[77] Ihlenburg, F., Mollenhoff, R., and Wandel, M. "Computational assessment of reduction methods in FE-based frequency-response analysis." In 11th World Congress on Computational Mechanics (WCCM XI), 5th European Conference on Computational Mechanics (ECCM V), 6th European Conference on Computational Fluid Dynamics (ECFD VI). 2014

[78] Biot, M. A. "General theory of three-dimensional consolidation." Journal of applied physics, 12(2), 155-164. 1941
DOI: https://doi.org/10.1063/1.1712886

[79] Biot, M. A. "Theory of propagation of elastic waves in a fluid saturated porous solid. I. Low-Frequency Range." The Journal of the Acoustical Society of america, 28(2), 168-178. 1956
DOI: https://doi.org/10.1121/1.1908239

[80] Biot, M. A. "Theory of propagation of elastic waves in a fluid saturated porous solid. II. Higher Frequency range." The Journal of the Acoustical Society of america, 28(2), 179-191. 1956
DOI: https://doi.org/10.1121/1.1908241

[81] MSC Actran 2022 User's Guide Vol. 1, Installation, Operations, Theory and Utilities, Free Field Technologies, Hexagon AB, 2022

[82] Maxit, L., and Guyader, J. L. "Estimation of SEA coupling loss factors using a dual formulation and FEM modal information, part I: theory." Journal of sound and vibration, 239(5), 907-930. 2001
DOI: https://doi.org/10.1006/jsvi.2000.3192

[83] Maxit, L., and Guyader, J. L. "Extension of SEA model to subsystems with non-uniform modal energy distribution." Journal of sound and vibration, 265(2), 337-358. 2003
DOI: https://doi.org/10.1016/S0022-460X(02)01459-1

[84] Nielsen, F. "Hierarchical Clustering." In: Introduction to HPC with MPI for Data Science. Undergraduate Topics in Computer Science. Springer, Cham. 2016
DOI: https://doi.org/10.1007/978-3-319-21903-5_8

[85] Hamerly, G., and Elkan, C. "Alternatives to the k-means algorithm that find better clusterings." In Proceedings of the eleventh international conference on Information and knowledge management. Association for Computing Machinery, New York, NY, USA, 600–607. 2002
DOI: https://doi.org/10.1145/584792.584890

[86] Pelleg, D., and Moore, A. W. "X-means: Extending k-means with efficient estimation of the number of clusters." In Proceedings of the Seventeenth International Conference on Machine Learning. Morgan Kaufmann Publishers Inc., San Francisco, CA, USA, 727–734. 2000

[87] Fisher, R. A., "Statistical Methods for Research Workers." Oliver and Boyd, Edinburgh, Scotland. 1958

[88] Optimus: Theoretical Background, Noesis Solutions, Leuven, Belgium, 147, 2013.

APPENDIX A

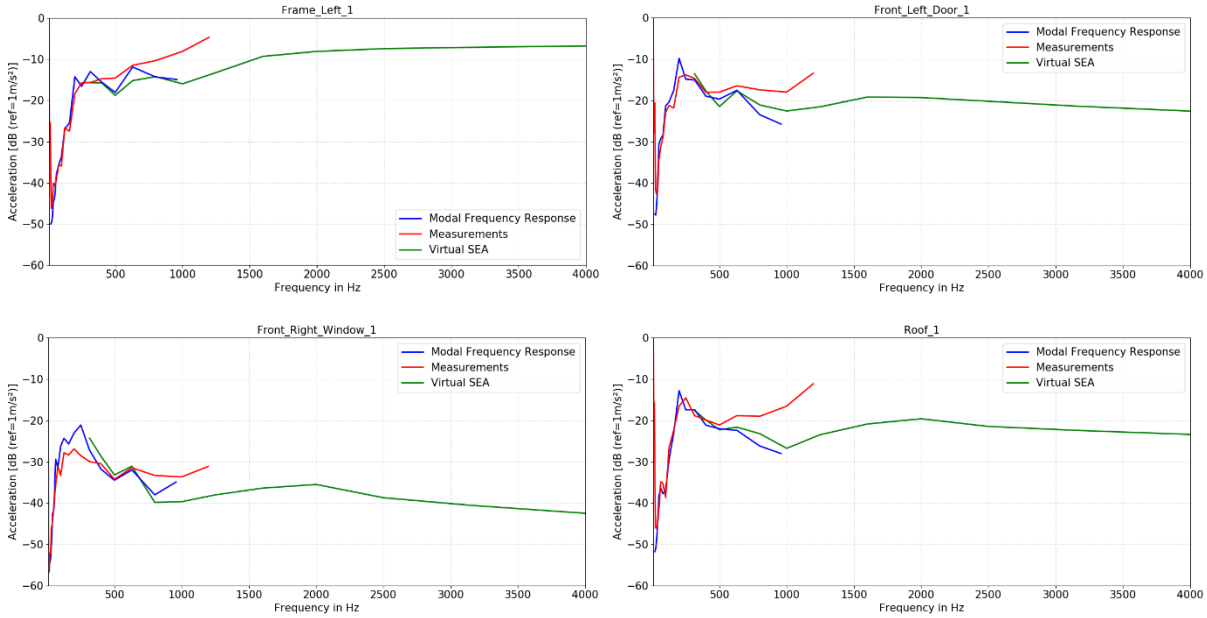

Figure 75. Mean accelerations on the frame left (upper left), front left door (upper right), front right window (bottom left), roof (bottom right) in BIB configuration, load case 1. Measurement (red), modal frequency response (blue), Virtual SEA (green).

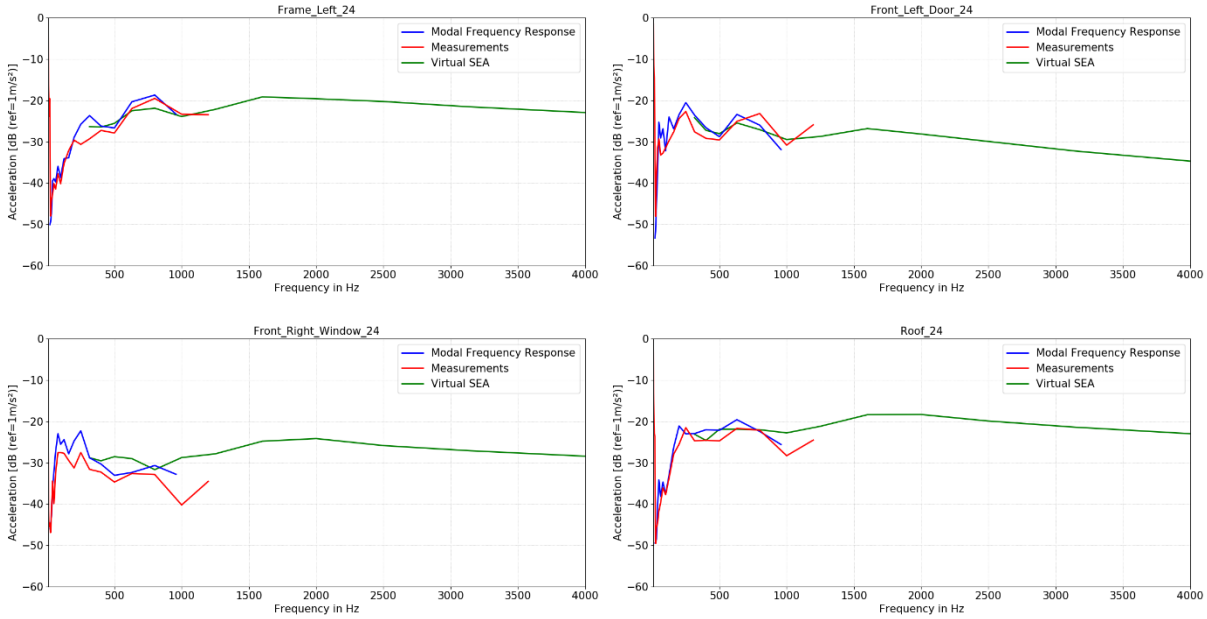

Figure 76. Mean accelerations on the frame left (upper left), front left door (upper right), front right window (bottom left), roof (bottom right) in BIB configuration, load case 24. Measurement (red), modal frequency response (blue), Virtual SEA (green).

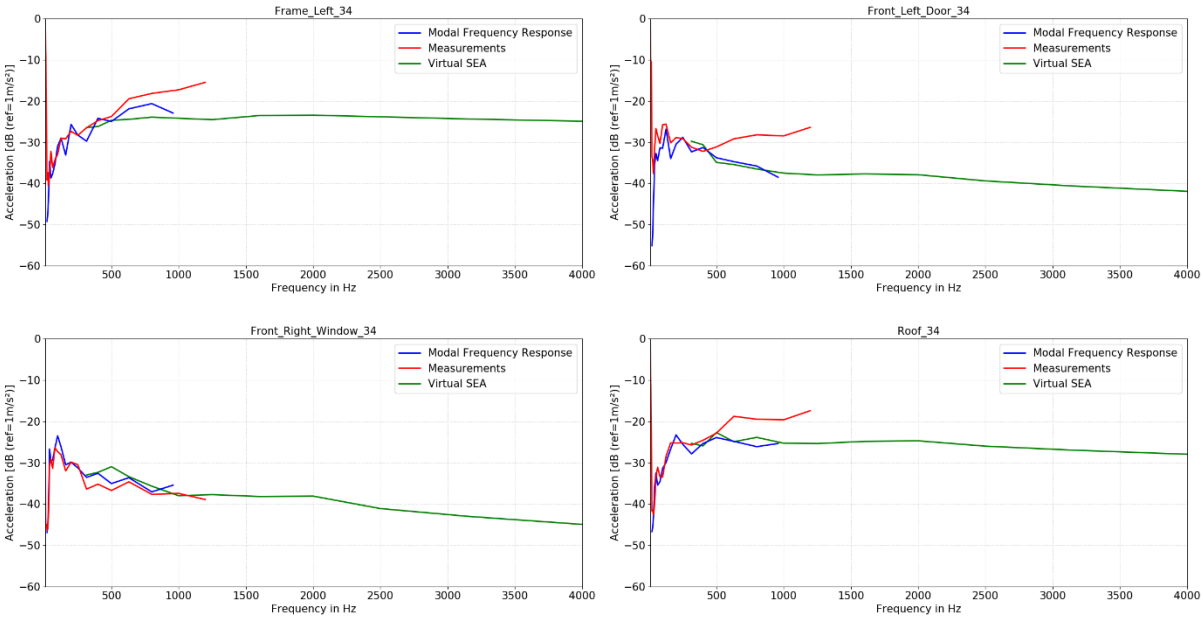

Figure 77. Mean accelerations on the frame left (upper left), front left door (upper right), front right window (bottom left), roof (bottom right) in BIB configuration, load case 34. Measurement (red), modal frequency response (blue), Virtual SEA (green).

Figure 78.